
LOOKING FOR AXION-LIKE-PARTICLE DI-PHOTON DECAY IN THE FASER EXPERIMENT USING SiGe BiCMOS PIXEL DETECTORS.

2020 - 2021



WRITTEN BY
THÉO MORETTI

Université de Genève, Suisse
Section de Physique - Département de Physique Nucléaire et Corpusculaire
THEO.MORETTI@ETU.UNIGE.CH

SUPERVISED BY PROFESSOR GIUSEPPE IACOBUCCI AND PROFESSOR FRANCESCO RIVA

Contents

1	Introduction	2
2	The QCD Axion and more general Axion-Like-Particles	4
2.1	Motivation of the QCD Axion	4
2.2	The Strong CP problem	6
2.2.1	Pseudoscalar masses problem in low energy QCD	6
2.2.2	Solution to the $U(1)_A$ problem	8
2.2.3	QCD vacuum	9
2.2.4	CP-violating terms in QCD	10
2.3	The axion solution to the Strong CP problem	12
2.4	Axion-Like-Particles and coupling to SM gauge bosons	14
3	Axion-Like-Particles in FASER	16
3.1	The ForwArD Search ExpeRiment (FASER)	16
3.1.1	Current design	17
3.1.2	Non-charged decays	19
3.2	ALPs phenomenology	19
3.2.1	Production from heavy meson decays	20
3.2.2	Decay into di-photons	22
3.3	The Pre-Shower module	25
3.3.1	Design of the PS module	25
4	Monte-Carlo simulations for ALPs in FASER	27
4.1	Meson spectrums from ATLAS IP	27
4.2	Mesons decays into ALPs	28
4.3	ALPs decays within FASER	30
4.4	Topology of di-photon signals	35
4.4.1	Sensitivity reach of FASER's PS detector	40
5	Time resolution of SiGe BiCMOS pixel detectors	42
5.1	Fundamentals of silicon pixel detectors	42
5.1.1	Doped semiconductors and junctions	42
5.1.2	Silicium pixel detectors	43
5.1.3	Electronic noise	44
5.2	Measuring the time resolution	45
5.2.1	The ATTRACT prototype	46
5.2.2	Reference sensor: LGAD	47
5.2.3	Layout of experiment	49
5.2.4	Data taking scheme	51

6	Results for time resolution of the ATTRACT sensor and Time walk correction	54
6.1	Calibration	54
6.2	Time walk correction	57
6.2.1	Event selection	57
6.2.2	Time walk correction procedure	58
6.2.3	TOF fitting method	63
6.2.4	Time resolution results	64
7	Outlook and conclusion	67
	Bibliography	71

Acknowledgements

In the first place, I would like to express my gratitude to Professor Giuseppe Iacobucci and Professor Francesco Riva with giving me the special opportunity to perform a Master Thesis with both of them, working on both theoretical and experimental Physics. I would particularly thank them for believing in my potential and giving me the opportunity to fulfill this thesis. I also would like to thank Professor Lorenzo Paolozzi who dedicated a lot of his time to give me all of the background I needed to start my work, as well as always being patient with the continuous flow of questions I submerged him with. I'm grateful of the many discussion I had with all three of you, which enlarged my knowledge and from which I always extracted positive feedback.

In a more general way, I would like to thank all of the members of the group of Professor Iacobucci for welcoming me and always helping me when needed. I'm very glad to have joined such an excellent group of hard working people as well as good friends.

I would like to express my particular gratitude to my parents Damien and Thamila Moretti for their emotional support throughout the past five years, as well as my grands parents Nordine and Marie Aït-Laoussine with whom I leaved each week, always caring for me and making sure I could pursue my studies in the best possible way. There were some particular difficult moment I had to face and I strongly believed I would not be where I am today without you.

I would also like to thank the amazing group of friends who accompanied me for the Bachelor and the Master degrees. The adventure would not have been the same without you and the many things we all went through together. I found in all of you good support and motivation which again allowed me to be where I am today. I would especially thank my girlfriend Sibilla Giovanetti for here never ending support and for believing in me when I could not. The last but not least, I want to thank my partner for half of my master thesis, Carmelo Mileto, from whom I learned a lot, not only on the professional point of view but also the personal point of view. It could have the taste, for a brief amount of time, of the feeling of having an incredible teammate with whom we performed amazing work.

Finally, I would have wished that my other grands parents, Joseph and Christiane Moretti could be there to see their grandkid follow his dreams in becoming a Physicist, you always have been proud of me and I'm sure from where you are, you continue to be.

Théo Moretti

Chapter 1

Introduction

In the contemplation of Nature, one might have noticed that what makes it beautiful but also strange at the same time is the many symmetries it exhibits. In Physics, symmetries are part of the fundamental basis on which physicist have been building the laws allowing them to describe Nature through their constant will of describing the environment they live in. Out of the many astonishing outcomes of this description lies one of the most remarkable theorem which was stated as Emmy Noether's first theorem in 1915 she proved to be:

"To every differentiable symmetry generated by local actions, there corresponds a conserved current."

The later statement is more precisely referring to the principle of covariance which is one of the requirements of any law of Physics and then allows to write the conservation of a certain quantity through a continuity equation. At the time of which this theorem was established, it was referring specifically to the concepts of conservation of energy, momentum and angular momentum which are nothing else than direct consequences of space and time symmetries in classical mechanics.

Nowadays, the description of Nature and hence of the fundamental constituents of matter is done by the Standard Model of Particle Physics (SM) based on Quantum Field Theory (QFT), which is nothing else than quantum mechanics merged with relativity, it can be seen as quantum mechanics but with an un-conserved number of particles in a system. In Quantum Field Theory, one iQFTs interested in the symmetries of space and time but not only and this has led to many interesting discoveries during the past century. Some of the other symmetries investigated are here discrete symmetries, namely the Charge Conjugation (C), the Parity (P) and the Time Reversal (T). Although these symmetries were thought to be exact symmetries of any derived law in QFT, it has been shown by Nobel prize winners Lee and Yang in 1956 [1] that no experiment could prove the parity in weak interactions not to be broken and hence weak interactions violates parity but also charge conjugation, we say that weak interactions are not CP preserving.

This non conservation also arose in the study of Strong interactions when looking at the properties of the Lagrangian describing the low energy regime of strong interactions and the study of this apparent non conservation will be the first subject discussed in what follows. Indeed, this thesis will, in the first part, discuss the CP problem in Quantum Chromodynamics (QCD) and present the theoretical solution to this problem, the QCD Axion. It will then cover its properties and move towards a more general description of any weakly coupled light pseudoscalar particle, also called Axion-Like-Particles (ALPs) that could hint to Physics beyond the Standard Model of Particle Physics.

This thesis will also present why the FASER experiment at CERN could be a good opportunity to hunt for such light particles if a dedicated piece is added to the original design of the detector, it will mainly go through simulations made to understand the topology of events coming from the decay of ALPs and through the choice of the characteristics such a detector should have to be sensitive to ALP decays.

In the second part of this thesis will be discussed the proposed technology for detecting the decays of the ALP, a di-photon decay which will be covered in more details later. The interest in pixel detector has been continuously growing especially because this technology has been offering never seen before time resolution at low power consumption but can also provide good spatial resolution which will be the key aspect here. The technology used is a Bipolar Junction Transistor (BJT) and Complementary Metal-Oxide Semiconductor (CMOS) with Silicon Germanium (SiGe) used as the base of the transistor of the BJT to provide it with higher working frequencies but also with better noise performances.

There will here be presented the characterization in terms of timing resolution of a specific chip designed for a different project but still based on the same technology which will enable a good overview of how such sensors work. This work will mainly go through the experimental set-up needed to perform such characterization, but also how to correct for effects like time walk in order to obtain the best possible time resolution.

Chapter 2

The QCD Axion and more general Axion-Like-Particles

2.1 Motivation of the QCD Axion

Before going to the quantum level and see why CP seems not to be a symmetry of the strong interactions as predicted by QCD, let's first go through a very simple but meaningful calculation of the electric dipole moment (eDM) of the neutron at the classical level.

In such a picture, we can simply illustrate the neutron as a sphere of a certain radius r_n . It would be composed of three smaller spheres, one up quark of charge $q_{up} = 2/3e$ and two down quarks of charge $q_{down} = -1/3e$. If we were to ask anyone to draw such a particle, it would probably look like the figure 2.1 with the three quarks placed on the summit of a triangle.

If we recall that the classical expression for the eDM \vec{d} of a set of charges is given by the following equation:

$$\vec{d} = \sum_i q_i \vec{r}_i \quad (2.1)$$

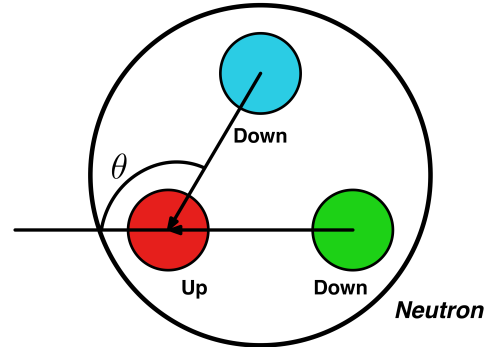


Figure 2.1: Classical view of neutron

We then use the fact that the distance between each individual quark is approximately two times the radius of the neutron which is of the order of $r_n = 0.8fm$ [2] . Doing the calculation would give an estimation of the eDM of the neutron like follows:

$$\vec{d}_n = \begin{bmatrix} -\frac{2}{3} \cdot r_n \\ 0 \end{bmatrix} - \begin{bmatrix} -\frac{2}{3}r_n \cos(\pi - \theta) \\ -\frac{2}{3}r_n \sin(\pi - \theta) \end{bmatrix} \Rightarrow \|\vec{d}_n\| \simeq 10^{-13} \cdot \sqrt{1 - \cos(\theta)} e \text{ cm} \quad (2.2)$$

We thus have that the classical expectation for the magnitude of the neutron eDM is of the order of $10^{-13}e\text{cm}$. Now regarding its direction, since there is only one vector which breaks Lorentz symmetry that is the spin of the neutron [3], the eDM has to also point in the same direction. Since the first measurement of the neutron eDM back in 1957 by Smith, Purcell and Ramsey [4] , many other experiments have been trying to refine this measurement thanks to increasing precision in the measurement. The simplest conceptual way in which such a measurement is done is via precession of the neutron.

If we consider a certain number of neutrons prepared such that they all have their spin pointing in the same direction, lets say the up direction, sent through a set of parallel magnetic and electric fields, the neutron would undergo Larmor precession at a frequency of:

$$\nu_{Larmor,\pm} = 2\|\vec{\mu} \cdot \vec{B} \pm \vec{d} \cdot \vec{E}\| \quad (2.3)$$

After waiting a certain time, by counting how many of the neutrons have seen their spin direction change, it is possible to determine the precession frequency $\nu_{Larmor,+}$. By making the direction of the magnetic and electric field anti-parallel, it is then possible to measure the second precession frequency, namely $\nu_{Larmor,-}$. If the neutrons were to have a non zero eDM, this effect of the electric field would change the torque on the neutron exerted by the fields and hence change the precession frequency. The neutron eDM can then be bounded by taking the difference of the two precession frequencies in the parallel and antiparallel field configurations. The latest measurement performed to measure the neutron eDM gave the upper bound of [5] :

$$\|\vec{d}_n\| \leq 2.9 \cdot 10^{-26} e \text{ cm} \quad (2.4)$$

We just have made explicit what is called the Strong CP problem or for instance, why is the angle θ so small, meaning that instead of being placed at the edges of a triangle, the quarks would need to almost be aligned on a straight line. Let's now go through the solutions at a classical level such a problem could have and understand why it is so-called the strong CP problem.

- i) The first solution would be that Parity is not a good symmetry of Nature, after all this does not sound completely absurd since it has already been proven that in the SM, weak interaction violates Parity. Under Parity symmetry, space coordinates transforms as follows:

$$P : \vec{x} \rightarrow -\vec{x} \quad (2.5)$$

If we now consider a neutron having its spin \vec{s} and its eDM \vec{d}_n pointing in the same direction and recalling that spin is a pseudo-vectorial quantity, both the spin and the eDM changes under Parity as:

$$P : \vec{d}_n \rightarrow -\vec{d}_n \quad P : \vec{s} \rightarrow \vec{s} \quad (2.6)$$

Under Parity, the neutron goes from $\hat{s} = \hat{d}_n$ to $\hat{s} = -\hat{d}_n$ and being an experimentally proven fact that the neutron has spin 1/2, the only solution for the neutron to go to himself under Parity transformation is to have a null eDM. This is the Parity solution to the strong CP problem but as said before, Parity is violated in weak interactions and is not a good symmetry of Nature, hence the solution to the Strong CP problem has to be different.

- ii) The second solution is Time symmetry which is also called Charge-Parity (CP) symmetry since it has been proven that Charge-Parity-Time (CPT) is a good symmetry of Nature. Under Time parity the time coordinates transforms as follows:

$$T : t \rightarrow -t \quad (2.7)$$

If we consider as before a neutron with its spin \vec{s} and its eDM \vec{d}_n pointing in the same direction, then under Time-reversal these quantities would change as:

$$T : \vec{d}_n \rightarrow \vec{d}_n \quad T : \vec{s} \rightarrow -\vec{s} \quad (2.8)$$

Under Time-Reversal, the neutron would once again go from $\hat{s} = \hat{d}_n$ to $\hat{s} = -\hat{d}_n$ and this would also mean that the neutron eDM has to be null. Once again CP has been proven not to be a good symmetry of Nature since in the Cabbibo-Kobayashi-Maskawa (CKM) matrix, it has been shown that the CP-violating phase is non negligible [6] .

- iii) The third and last solution we will discuss here is the Axion solution, in fact having the angle θ being small would mean that both the down quarks would surround the up quark and such arrangement of charges seems very natural. The key concept here is to make the angle θ dynamical such that if initially the system is in a state with $\theta \neq 0$ it can quickly reach the state in which $\theta = 0$ and hence it solves the Strong CP problem. The Axion solution makes θ dynamical and it can be proven that the minimum will always be at $\theta = 0$ [3].

We have seen in the above discussion what was the origin of the Strong CP problem and the proposed solution on the classical level: the Axion solution. Let's now move to the QFT level by giving a more complex and detailed description of the Strong CP problem and to understand why also at this level the Axion solution has strong motivations.

2.2 The Strong CP problem

In the SM, the theory describing the interactions between elementary particles known as quarks and gluons but also describing non elementary states in which a quark and an anti-quark (Mesons) or three quarks or anti-quarks (Baryons) are bounded together (more generally called Hadrons) is called QCD. In the early years of this theory, a major effort has first been done to try and classify hadrons thanks to the discovery of Isospin in 1937 by E. Wigner [7] and Strangeness in 1955 by K. Nishijima [8], but a couple years later problems started to arise with respect to the spectrum of the pseudoscalar mesons and the predicted masses.

2.2.1 Pseudoscalar masses problem in low energy QCD

In order to understand better what is the problem with the pseudoscalar mesons masses, it is interesting to consider in the first place the QCD Lagrangian in the low-energy limit which means with quark masses below the QCD scale Λ_{QCD} . If one does so, it would end with a theory in which only up and down quark contribute and with the following Lagrangian:

$$\mathcal{L}_{QCD} = -\frac{1}{4}G_{\mu\nu}^a G_{\mu\nu}^a + \sum_n i\bar{q}_n \gamma^\mu D_\mu q_n + \sum_n m_{q_n} \bar{q}_n q_n \quad (2.9)$$

We have used the notation D_μ to define the gauge covariant derivative associated to the interactions with gluons i.e. the SU(3) gauge symmetry, defined here as $D_\mu = \partial_\mu - ig_3 A_\mu^a t^a$. We also have defined the field strength tensor for gluons as $G_{\mu\nu}^a t^a = \frac{i}{g_3} [D_\mu, D_\nu]$ where g_3 is the coupling associated to strong interactions and have finally introduced a set of quarks field q_n with n being the number of quarks flavors under consideration, here $n = 2$.

If we now consider that the quark masses are sufficiently small that we can ignore the last term in the expression for the QCD Lagrangian, there is no mixing between left-handed and right-handed quarks which makes it actually symmetric under the following separate unitary transformations:

$$\begin{pmatrix} u \\ d \end{pmatrix}_L = U_L \begin{pmatrix} u \\ d \end{pmatrix}_L \quad ; \quad \begin{pmatrix} u \\ d \end{pmatrix}_R = U_R \begin{pmatrix} u \\ d \end{pmatrix}_R \quad (2.10)$$

Such transformations on the chiral quark states can be decomposed as $U(2) \simeq SU(2) \times U(1)$ which makes the massless QCD Lagrangian with 2 flavors being symmetric under the group $SU(2) \times SU(2) \times U(1) \times U(1)$. If we denote the chiral quark doublets as follows [9] :

$$q_L = \left(\frac{1 - \gamma^5}{2} \right) \begin{pmatrix} u \\ d \end{pmatrix} \quad ; \quad q_R = \left(\frac{1 + \gamma^5}{2} \right) \begin{pmatrix} u \\ d \end{pmatrix} \quad (2.11)$$

It is possible to write the Noether currents associated to each symmetry as [9] :

$$j_L^\mu = \bar{q}_L \gamma^\mu q_L \quad ; \quad j_R^\mu = \bar{q}_R \gamma^\mu q_R \quad (2.12)$$

$$j_L^{\mu a} = \bar{q}_L \gamma^\mu \tau^a q_L \quad ; \quad j_R^{\mu a} = \bar{q}_R \gamma^\mu \tau^a q_R \quad (2.13)$$

We have here labeled $\tau^a = \sigma^a/2$ the generators of the $SU(2)$ group and the σ_a are the Pauli matrices. Now if we take on one hand the sum of the left-handed and right-handed current for both set of equations 2.12 and 2.13 , we will get the baryon number and isospin vector current as follows:

$$j^\mu = \bar{q} \gamma^\mu q \quad ; \quad j^{\mu a} = \bar{q} \gamma^\mu \tau^a q \quad (2.14)$$

The corresponding symmetries are nothing else than the transformations we wrote above for the chiral quark states but with the condition that $U_L = U_R$. If we take on the other hand the difference of the left-handed and the right-handed currents for the two set of equations 2.12 and 2.13, we will get the axial currents:

$$j^{\mu 5} = \bar{q} \gamma^\mu \gamma^5 q \quad ; \quad j^{\mu 5a} = \bar{q} \gamma^\mu \gamma^5 \tau^a q \quad (2.15)$$

As we have said, the vector transformations, which we will now label as $SU(2)_V \times U(1)_V$, are manifest symmetries of the strong interactions leading to the conservation of baryon number and isospin quantum numbers. One could then wonder if the axial currents also led to conservations laws or if these are not symmetries of the strong interactions.

In fact in 1960, Nambu and Jona-Lasinio hypothesized the fact that these are spontaneously broken accurate symmetries of the strong interactions which led to a correct description of the properties of strong interactions at low-energy.

Still considering the massless limit for the QCD Lagrangian with only 2 quark flavors, quarks and anti-quarks have strong attractive interactions and being massless, the cost to create an extra quark-antiquark pair is rather small[9]. For this reason we expect the QCD vacuum to contain a condensate of quark-antiquark pair and since these pairs should have zero total momentum and angular momentum, thus having a net chiral charge since pairing left-handed quarks with the antiparticle of a right-handed quark as show in figure 2.2.



Figure 2.2: Quark condensate

It has been proven experimentally that the vacuum expectation value for the quark condensate is non zero:

$$\langle 0 | \bar{q} q | 0 \rangle = \langle 0 | \bar{q}_L q_R + \bar{q}_R q_L | 0 \rangle \neq 0 \quad (2.16)$$

Such states transforms under the symmetry group with $U_L \neq U_R$ and the fact that the expectation value is different from zero signals that the symmetry group is spontaneously broken into the subgroup of vector symmetries with $U_L = U_R$. According to the Goldstone theorem, since the axial symmetry group $SU(2)_A \times U(1)_A$ is spontaneously broken, there have to be for each of the 3+1 broken generators a massless particle with the quantum numbers of a local symmetry rotation. Phrased another way this means that in a theory of strong interactions with massless

up and down quarks, there should exist four spin-zero particles with the appropriate quantum numbers to be created by the four axial currents.

The picture we described before is interesting to understand the properties of the low-energy QCD with massless quarks but strong interactions do not contain any massless quarks but they do contain an isospin triplet of relatively light mesons: the pions. These mesons are known to have odd Parity properties since being composed of a quark anti-quark pair and can then be created by the axial isospin currents.

To understand this a bit further we can try to parametrize the matrix elements of the current $j^{\mu 5a}$ between the vacuum and an on-shell pion, still in the massless limit by writing [9]:

$$\langle 0 | j^{\mu 5a}(x) | \pi^b(p) \rangle = -i p^\mu f_\pi \delta^{ab} e^{-ip \cdot x} \quad (2.17)$$

We have here labeled as a and b the isospin indices and f_π is the pion decay constant which can be estimated experimentally as $f_\pi = 93$ MeV. If we contract the equation 2.17 with p_μ and use the conservation of the axial currents, we find that an on-shell pion has to satisfy $p^2 = 0$ which means it have to be massless as required by Goldstone's theorem.

The next logical step is to take the QCD Lagrangian with non zero quark masses to see if the expression we developed above would change and thus one can write the non conservation of the axial current as [9]:

$$\partial_\mu j^{\mu 5a} = i \bar{q} \{M, \tau^a\} \gamma^5 q \quad \text{with: } M = \begin{pmatrix} m_u & 0 \\ 0 & m_d \end{pmatrix} \quad \text{the quark mass matrix} \quad (2.18)$$

The axial symmetry is then no longer an exact symmetry of the QCD Lagrangian but is only approximately realized if the quark masses are sufficiently small. In this case one should no longer observe massless Goldstone boson but Pseudo-Nambu-Goldstone bosons which do have a mass different from zero. The pion triplet fits exactly in the predicted masses from the spontaneous breaking of the $SU(2)_A$ symmetry group but there do not exist any light singlet available to identify with the spontaneous breaking of the $U(1)_A$ symmetry group. This means that if $U(1)_A$ is broken at a certain scale f_b , then there should exist a meson with mass bounded by [10] :

$$m_{\eta'} = \frac{\sqrt{3} m_{\pi^0} f_\pi}{\sqrt{f_\pi^2 + 8f_b^2}} \leq \sqrt{3} m_{\pi^0} \approx 233.8 \text{ MeV} \quad (2.19)$$

Since no such state exists it implies that the axial rotation is not actually an approximate symmetry of the strong interactions, this is referred to as the $U(1)_A$ problem.

2.2.2 Solution to the $U(1)_A$ problem

Since we just found out the axial rotation does not seem to be even an approximate symmetry of the QCD Lagrangian, if one was to perform an axial rotation such as $q \rightarrow e^{i\theta\gamma^5/2} q$ by some angle θ , this would induce the following term in the Lagrangian [10] :

$$\mathcal{S}_\theta = \frac{\theta g_3^2}{32\pi^2} \int d^4x \tilde{G}_a^{\mu\nu} G_{\mu\nu}^a \quad (2.20)$$

We have above used the dual field-strength tensor defined as $\tilde{G}_a^{\mu\nu} = \frac{1}{2} \epsilon^{\mu\nu\alpha\beta} G_{\alpha\beta}^a$ and by having this additional, CP-violating term in the Lagrangian, the $U(1)_A$ problem seems to be solved. Nevertheless, a closer look at this term shows that we can rewrite the product of the field-strength tensor and its dual $\tilde{G}_a^{\mu\nu} G_{\mu\nu}^a$ as a total divergence $\partial_\mu K^\mu$ of the following current [11] [10] :

$$K^\mu = \epsilon^{\mu\nu\alpha\beta} \left(A_\nu^a G_{\alpha\beta}^a - \frac{g_3}{3} f^{abc} A_\nu^a A_\alpha^b A_\beta^c \right) \quad (2.21)$$

We have labeled here as f^{abc} the structure constants of the $SU(3)$ algebra and we have labeled the gluon fields as A_μ . Therefore the additional term in the QCD Lagrangian can be seen as the integral over four dimensional space of a total derivative which can be also written as a surface integral over the boundary at spatial and temporal infinity.

It is common in field theory to ignore such terms since they are assumed to vanish at the boundary and hence to have no contribution in perturbation theory. The assumption one would simply make is that the for an arbitrary field strength tensor $F_{\mu\nu}^a$ this previous goes to zero at the boundary which implies we must also have $A_\mu^a t_a$ going to zero at the boundary. However, the correct assumption to make is that any gauge transformation of zero also satisfies the boundary conditions:

$$A_\mu^a t_a = 0 \rightarrow \frac{i}{g_3} U \partial_\mu U^{-1} \quad (2.22)$$

We have in the equation 2.22 defined as U a differentiable map from the angular coordinates to the elements of the $SU(3)$ gauge group. If we consider an Abelian gauge theory the difference between having $A_\mu = 0$ or having the pure gauge is trivial because all possible gauge configurations can be obtained continuously from the trivial one [3]. The previous statement means that one can make a continuous gauge transformation V such that we obtain $V = U^{-1}$:

$$\frac{i}{g_3} U \partial_\mu U^{-1} \rightarrow \frac{i}{g_3} V \left(U \partial_\mu U^{-1} \right) V^{-1} + \frac{i}{g_3} V \partial_\mu V^{-1} = \frac{i}{g_3} (VU) \partial_\mu (VU)^{-1} \quad (2.23)$$

As mentioned above this works perfectly fine for Abelian gauge theory but as long as QCD is a non-Abelian gauge theory per se, there cannot exist gauge transformations in which the continuous deformation is not possible. Such configurations are locally equivalent to zero but cannot be gauged away globally since they are different on a topological level.

Now armed with the fact that the additional term we found to be added by axial rotation on the quark fields can apparently contribute, $U(1)_A$ is hence not a symmetry of the strong interactions and this solves the so called $U(1)_A$ problem.

2.2.3 QCD vacuum

The most immediate outcome is that QCD must have an infinite number of topologically distinct vacua $|n\rangle$ associated with the infinite number of gauge configurations. An intuitive way to see this is through the homotopy class of the configurations since the gauge transformations are nothing else than maps between the boundary of the 3-sphere S^3 to the $SU(3)$ group elements. These previous are then classified by the third homotopic group $\pi_3 = [SU(3)] = \mathbb{Z}$ meaning there exists an infinite number of vacua which can be identified by the homotopic invariant n , the winding number [10] .

It can be shown that the winding number can be written as an integral over the associated gauge fields:

$$n = \frac{g_3^2}{32\pi^2} \int d^4x \tilde{G}_a^{\mu\nu} G_{\mu\nu}^a \in \mathbb{Z} \quad (2.24)$$

From a qualitative point of view, this is very similar to a double-well potential in non-relativistic quantum mechanics. The potential would then have two degenerate minima and a non zero amplitude to tunnel back and forth between them. In perturbation theory this implies that the ground state of the system has to be a superposition of the two wells.

In QCD the situation is analogous and one finds a pseudo-classical solution, corresponding to tunneling between different vacua with different winding number. Such solutions are called

instantons. Therefore the different vacua have a non zero overlap, are unstable and the physical QCD vacuum should hence be a superposition of all the vacua:

$$|\theta\rangle = \sum_n e^{-in\theta} |n\rangle \quad (2.25)$$

The effect of a gauge transformation T_m on the vacua states $|n\rangle$ is then to change the winding number as $T_m |n\rangle = |n+m\rangle$ and the QCD vacuum $|\theta\rangle$ is then an eigenstate of such operator [10] :

$$T_m |\theta\rangle = \sum_n e^{in\theta} |n+m\rangle = \sum_l e^{i\theta(l-m)} |l\rangle = e^{-im\theta} |\theta\rangle \quad (2.26)$$

We can now write down what is the contribution to the effective action coming from instanton effect by computing the vacuum-to-vacuum transition amplitude with the outgoing side going at $t = +\infty$ and the incoming side at $t = -\infty$ [10]:

$$\begin{aligned} {}_{out}\langle\theta|\theta\rangle_{in} &= \sum_{m,n} e^{-i(n-m)\theta} {}_{out}\langle m|n\rangle_{in} = \sum_{\nu} e^{i\nu\theta} \sum_n {}_{out}\langle \nu+n|n\rangle_{in} \\ &\propto \sum_{\nu} \int [\mathcal{D}A]_{\nu} \cdot \exp \left(i \{ \mathcal{S}_{QCD}[A] + \frac{\theta g_3^2}{32\pi^2} G_a^{\mu\nu} \tilde{G}_{\mu\nu}^a \} \right) \end{aligned} \quad (2.27)$$

We have here used the path integral formalism and the piece $[\mathcal{D}A]_{\nu}$ means that the integration has to be performed over gauge transformations with winding number $\nu = m - n$. Since a gauge transformation changes the winding number of the vacua $|m\rangle$ and $|n\rangle$ by the same amount, the amplitude should not change and so the overlap $\langle m|n\rangle$ has to depend only on ν .

The consequences of having non perturbative instantons effect is to have an additional term in the effective action for all the possible vacuum transitions ν . Another interesting fact is that the induced term in the effective action has the exact same form as the one induced by chiral transformations on the QCD Lagrangian. It means that even if one does not take into account in the Lagrangian this term, instanton effects will generate it.

The parameter θ hence becomes a time-independent property of the vacuum and the vacuum's energy depends on the value of this parameter. It can be shown that an approximate form of the vacuum's energy, considering only the first elements $\nu = 0, \pm 1$ in the sum over the possible vacuum transitions, can be written as [10] :

$$E(\theta) \approx \Lambda_{QCD}^4 [1 - \cos(\theta)] \quad (2.28)$$

Here the parameter Λ_{QCD} was inserted in order to give an estimation of the scale of the vacuum energy. One can also see this result from a different picture in which the chiral phase is incorporated inside the quark mass matrix and using the chiral Lagrangian for the vacuum's energy calculation would give the following expression [11] :

$$E(\theta) \approx f_{\pi}^2 m_{\pi}^2 \cos(\theta) \quad (2.29)$$

2.2.4 CP-violating terms in QCD

We have finally reached the conclusion that a CP-violating term in QCD seems nothing else than natural and takes the following form:

$$\mathcal{S}_{\theta QCD} = \frac{\theta_{QCD} g_3^2}{32\pi^2} \int d^4x \tilde{G}_a^{\mu\nu} G_{\mu\nu}^a \quad (2.30)$$

We now understand that if such term is only generated by the instanton effects, one could simply rotate it away with a specific choice of chiral phase but since the quark mass matrix M is in general complex one would have to perform a chiral rotation to make it real such that it would induce an identical term with chiral phase $\theta_F = \arg \det M$. These two identical terms would then leave a basis-independent and physically measurable phase:

$$\bar{\theta} = \theta_{QCD} - \theta_F \quad (2.31)$$

The chiral phase might be shifted back and forth between the quark mass matrix and the CP-violating term but it cannot be eliminated and since there is no a priori reason why the two contributions should cancel each other, the theoretical expectation for $\bar{\theta}$ is $\mathcal{O}(1)$.

Switching back to initial problem of the neutron eDM, one of the consequences of adding such a term is in fact to give to the neutron a non zero eDM proportional to $\bar{\theta}$. The calculation of such eDM is not trivial so we will here simply give an overview of it. We can start by writing the term in the Lagrangian responsible for the interaction between neutron and pions since diagrams involving pions loops generate a neutron eDM [11] :

$$\mathcal{L}_{\pi nn} = \pi^a \bar{\Psi} \left(i\gamma^5 g_{\pi nn} + \bar{g}_{\pi nn} \right) \tau^a \Psi \quad (2.32)$$

Here we have labeled as Ψ the proton and neutron isospin doublet, the first term is simply the coupling to pseudo-scalar pions for the neutrons which gives the Yukawa potential describing the strong nuclear forces between nucleons. The second term is the CP-violating term, corresponding to the coupling between neutrons and pions $\bar{g}_{\pi nn}$, which must be proportional to $\bar{\theta}$. The Feynman diagram for the process in which a neutron acquires an eDM is at leading order given by the following figure:

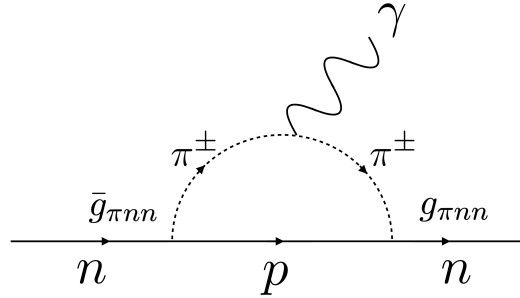


Figure 2.3: Pion loop and neutron eDM

The CP-violating term appears at the vertex involving the term $\bar{g}_{\pi nn}$ and so the eDM for the neutron is generated at this vertex. After many long and tedious calculations, the prediction for the neutron eDM is given by [11] :

$$d_n = \frac{m_n}{4\pi^2} g_{\pi nn} \bar{g}_{\pi nn} \ln\left(\frac{m_n}{m_\pi}\right) = \left(5.2 \cdot 10^{-16} \text{ e}\cdot\text{cm}\right) \bar{\theta} \quad (2.33)$$

As we have mentioned in the early beginning of this discussion about the neutron eDM, the actual bound on its value is $d_n \leq 2.9 \cdot 10^{-26} e \text{ cm}$ [5] which then allows us to put a bound on the $\bar{\theta}$ parameter as follows:

$$\bar{\theta} \leq 5.6 \cdot 10^{-11} \quad (2.34)$$

We arrive to the same conclusion as the one we made only with the classical considerations which is: why is the $\bar{\theta}$ parameter so small. This issue of naturalness would mean that two a

priori unrelated parameters in the SM conspire to cancel each other up to one part in 10^{10} or more. We can now see what would be the proposed solutions to this problem as we did with our classical considerations [12] :

- i) One of the first solution to be proposed was the vanishing up quark mass solution. In fact if one of the quark masses would be zero, this would make the contribution in the QCD Lagrangian of the chiral phase go to zero $\theta_F = \arg \det M = 0$. This is even tough not a good solution since there are many evidences of why the up quark can't be massless [13] .
- ii) Another solution would be the fact that CP symmetry is actually spontaneously broken at a certain scale. This would make the parameter θ_{QCD} forbidden in the Lagrangian. However, it has been shown that if this suppresses the term at leading order, it would be re-induced by loop corrections [14].
- iii) The last solution we discuss here is an additional chiral symmetry which simply adds a chiral symmetry, effectively rotating the $\bar{\theta}$ term away and solving the problem. This solution is also known as the Axion solution, it provides a Dark Matter candidate as we will see later and is by far the strongest solution proposed so far.

2.3 The axion solution to the Strong CP problem

The axion solution to the strong CP problem was initially proposed by Peccei and Quinn in 1977 [15] and this solution was different from the others since it proposed a dynamical solution. Their initial idea was that the full SM Lagrangian would be invariant under an additional global chiral $U(1)$ symmetry also called Peccei-Quinn symmetry labeled $U(1)_{PQ}$. If the symmetry existed and was exact, this would automatically solve the strong CP problem since the parameter $\bar{\theta}$ would be set to zero through a chiral transformation.

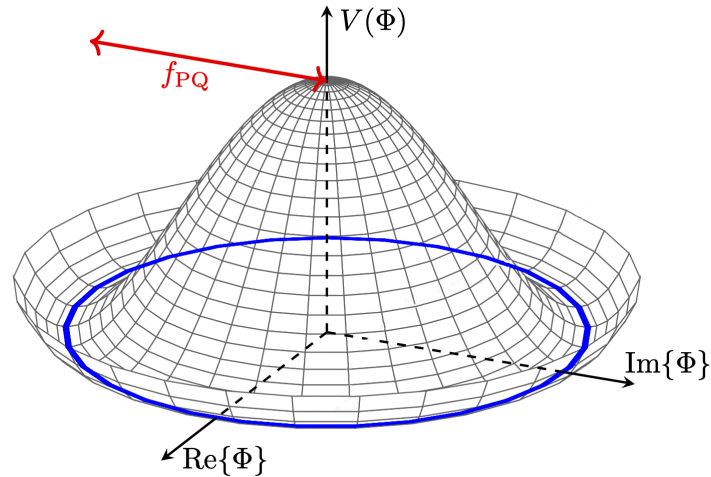


Figure 2.4: Spontaneous symmetry breaking potential

However, if such a symmetry is exact the result can be nothing but unphysical, in fact it has been shown by Peccei and Quinn that even if the $U(1)_{PQ}$ is spontaneously broken by some potential like the one in the figure 2.4, the $\bar{\theta}$ parameter would still be dynamically driven to zero. The difference is that this time a pseudo-Nambu Goldstone boson would join the dance.

Essentially the effect of adding this symmetry in the theory is to replace the static CP violating parameter $\bar{\theta}$ by the dynamical interactions of the axion field $a(x)$ which conserves CP

symmetry. An interesting aspect of this solution is that, being a pseudo Nambu Goldstone boson, the effect of a $U(1)_{PQ}$ transformation of the axion field is a translation. If we denote by α the phase parameter of this transformation and if we call f_{PQ} the scale at which the symmetry breaking occurs, we can write that:

$$U(1)_{PQ} : a(x) \rightarrow a(x) + \alpha f_{PQ} \quad (2.35)$$

This means that if the effective Lagrangian describing the full theory is invariant under such a symmetry, the axion field terms can only appear derivatively coupled, but this is without taking into account the fact that this symmetry is anomalous. In fact, the chiral anomaly causes the effective Lagrangian to have terms in which the axion field couples directly with the gluon density $\tilde{G}G$ such that the associated current j_{PQ}^μ has the correct chiral anomaly [12]. Taking into considerations the above conditions on how the axion field should appear in the effective SM Lagrangian, by promoting the $U(1)_{PQ}$ global symmetry, one would have the following terms appearing [12] :

$$\mathcal{L}_{SM}^{eff} = \mathcal{L}_{SM} + \bar{\theta} \frac{g_3^2}{32\pi^2} \tilde{G}_a^{\mu\nu} G_{\mu\nu}^a - \frac{1}{2} \partial_\mu a \partial^\mu a + L_{int} \left[\frac{\partial^\mu}{f_{PQ}} a; \psi \right] + \frac{a}{f_{PQ}} \xi \frac{g_3^2}{32\pi^2} \tilde{G}_a^{\mu\nu} G_{\mu\nu}^a \quad (2.36)$$

We have here labeled as ψ any field included in the theory and ξ is simply a model dependent parameter associated with the chiral anomaly of the $U(1)_{PQ}$ symmetry current which we can write in the following way [12]:

$$\partial_\mu j_{PQ}^\mu = \xi \frac{g_3^2}{32\pi^2} \tilde{G}_a^{\mu\nu} G_{\mu\nu}^a \quad (2.37)$$

The most interesting term in the effective Lagrangian given by 2.36 is the last one. It in fact gives to the axion field an effective potential making its vacuum expectation value (vev) non longer arbitrary. Finding the minimum of this potential will hence give the vev of the axion field $\langle a \rangle$ as follows [12]:

$$\left\langle \frac{\partial V_{eff}}{\partial a} \right\rangle = - \frac{\xi}{f_{PQ}} \frac{g_3^2}{32\pi^2} \left\langle \tilde{G}_a^{\mu\nu} G_{\mu\nu}^a \right\rangle \Big|_{\langle a \rangle} \quad (2.38)$$

It has been shown by Peccei and Quinn that the periodicity of the expectation value of the gluon density $\langle \tilde{G}_a^{\mu\nu} G_{\mu\nu}^a \rangle$ with respect to the $\bar{\theta}$ parameter, can be easily seen by writing an approximate form of the effective potential as follows[12]:

$$V_{eff}(a) \approx \frac{g_3^2 \Lambda_{QCD}^4}{32\pi^2} \left[1 - \cos \left(\frac{\xi \langle a \rangle}{f_{PQ}} + \bar{\theta} \right) \right] \rightarrow \langle a \rangle = - \frac{f_{PQ}}{\xi} \bar{\theta} \mod 2\pi \quad (2.39)$$

We see that the periodicity conditions in fact forces the vev of the axion field to take the above value. From this result it is straightforward to see that if we write the effective Lagrangian in terms of the physical axion field, ie $a_{phys} = a - \langle a \rangle$, the CP violating term would instantly vanish. Moreover, if one expands the effective potential of the axion field around its minimum, it witnesses that the axion itself can get a mass [12]:

$$m_a^2 = \left\langle \frac{\partial^2 V_{eff}}{\partial a^2} \right\rangle = - \frac{\xi g_3^2}{32\pi^2 f_{PQ}} \frac{\partial}{\partial a} \left\langle \tilde{G}_a^{\mu\nu} G_{\mu\nu}^a \right\rangle \approx \frac{g_3^2 \Lambda_{QCD}^4}{32\pi^2} \frac{\xi^2}{f_{PQ}^2} \quad (2.40)$$

In order to obtain the last expression we have taken the value of the expectation values at the minimum of the potential. It is important to notice that the expression here is only an approximation and if one would want to have a more rigorous expression, it would need to involve

the full chiral Lagrangian machinery. It is even more important to specify that the expression here strongly depends on the type of axion model under consideration since the ξ terms appears quadratically.

Our overview of the strong CP problem and its solution, the QCD axion is now over. In fact we have studied one of the problems of the SM, the small neutron eDM and have presented on both at the classical and the quantum level one of the most promising solution, the QCD axion. We also have seen that CP violating terms seems to be natural in QCD at first since both instanton effect and chiral rotation of the quark field would generate such a term but the QCD axion also solves this issue.

It is important to understand that taking a step back, one can realise that the model we developed is in fact very general and model-dependent. We previously only went through the anomalies linked to the gauge groups associated with gluons, $SU(3)$ but one could also investigate couplings to other vector bosons in the SM.

2.4 Axion-Like-Particles and coupling to SM gauge bosons

Until now, we have given a description of the QCD axion through the coupling only to gluons and by imposing conditions on the model such that it could solve the strong CP problem. Although more recent studies have been focusing, no longer on a model being able to solve the strong CP problem but on models involving pseudoscalar particles being light (with respect to the electroweak breakdown scale), weakly coupled and emerging from the spontaneous symmetry breaking of a global symmetry, also called Axion-Like-Particles (ALPs) [16]. Such particles are known to be Dark Matter (DM) candidates through the dimension of the operator responsible for the coupling of ALPs to the SM gauge bosons.

If we consider the simplest models of a low-energy effective field in which an ALP labeled a couples to vector bosons through the dimension-5 interactions as suggested by the associated Peccei-Quinn symmetry, one could write the interaction part of the Lagrangian with such fields as [17]:

$$\mathcal{L} = -\frac{1}{4}g_{aBB}aB_{\mu\nu}\tilde{B}^{\mu\nu} - \frac{1}{4}g_{aWW}aW_{\mu\nu}^a\tilde{W}^{a,\mu\nu} \quad (2.41)$$

We have labeled in the equation 2.41 for the $U(1)_Y$ and the $SU(2)_L$ gauge group, the field strength tensors respectively as $B_{\mu\nu}$ and $W_{\mu\nu}^a$ but also respectively the coupling to the ALP field as g_{aBB} and g_{aWW} with dimensions of GeV^{-1} . If such interactions are generated with some coupling α which was integrated in the theory at a certain (heavy) scale f , one expects that [17]

:

$$g_{aBB}, g_{aWW} \approx \frac{\alpha}{2\pi f} \quad (2.42)$$

This reminds us of course of the discussion we had while studying the coupling between the QCD axion and the gluon strength field tensor. Nonetheless such a coupling can be generalized for any pseudo Nambu-Goldstone boson with non-vanishing axial anomalies.

After electroweak symmetry breaking, the couplings g_{aBB} and g_{aWW} enables the coupling of the ALP to the photon (γ), and the three vector bosons responsible for charged and neutral current (respectively W^\pm and Z^0) as follows:

$$a \rightarrow \gamma\gamma \quad a \rightarrow \gamma Z^0 \quad a \rightarrow Z^0 Z^0 \quad a \rightarrow W^+ W^- \quad (2.43)$$

We reached the point in which it becomes almost impossible to go further into details without having to chose a specific model making the following discussion model-dependent and no longer

relevant. In fact ALPs could also couple to gluons and fermions through dimension-5 operators and even to the Higgs boson through dimension-6 operators and the discussion of all these couplings would need its own discussion.

For the sake of this thesis, only the models involving ALP coupling to di-photons and to the W^+ and W^- vector bosons will be investigated. Indeed, in the next chapter we will focus on ALPs produced through coupling to the W^+ and W^- vector bosons then decaying into di-photons.

Chapter 3

Axion-Like-Particles in FASER

3.1 The ForwArd Search ExpeRiment (FASER)

In the past few decades, the searches aiming at finding physics beyond the SM in particle collider experiments was mainly oriented towards particles in the TeV-scale mass range and coupling to the SM of the order of $\mathcal{O}(1)$. Taking as a reference the experiments at the Large Hadron Collider (LHC) at CERN, the searches for such models aim at high transverse momentum (p_T) particles. After many years of unsuccessful searches in this direction, one could ask itself if new physics could not be instead light and weakly coupled to the SM particles [18].

The main interest has recently moved towards these completely different models which are especially interesting since they may be good candidates for Dark Matter (DM). Regarding the p_T for these particle in the mass range of MeV-scale to GeV-scale, which can be of the order of p_T 100 MeV - GeV, it should be rather small with respect to the p_T for models in which masses belong to the TeV-scale. This would imply that the actual searches would be completely misguided since these particles would be created in what is called the very forward region.

The downside of such models could be at first sight the extremely weak coupling to the SM but if the rates of events can be used as a counter part, one could actually probe these models at particle colliders. Taking the LHC at 13 TeV as a benchmark, the total inelastic proton-proton (pp) scattering cross section is approximately $\sigma_{inel}(13TeV) \approx 75$ mb [19] and most of it is in the forward direction. For the LHC at 14 TeV, the cross section is very similar and hence the expected number of pp inelastic scatterings for an integrated luminosity of 150 fb^{-1} is [18] :

$$N_{inel} \approx 1.1 \cdot 10^{16} \quad (3.1)$$

This high number of inelastic collisions means that even extremely weakly coupled models might give sufficient number of events in the very forward region. Another consequence of the weak coupling to the SM is also the fact such particles might be long-lived and would hence travel long-distances before decaying into SM particles. For example, particles originating from B mesons or pions are typically produced within angles of the order of [18] :

$$\theta = \frac{\Lambda_{QCD}}{E} \quad \text{or} \quad \frac{m_B}{E} \approx 100 \text{ } \mu\text{rad} \quad (3.2)$$

We have labelled in the previous equation E the energy of the incoming particle. This means that even after half a kilometer downstream, such particles would only spread 0.1 m to 1 m in the transverse plane.

Taking all of the previous considerations together, if one was to design a detector capable of being sensitive to SM decay products of such particles, it would need to build a small detector, in covered solid angle from interaction point (IP), due to the highly collimation of the Long-Lived-Particles (LLPs), located far from the IP such that the LLPs would decay inside the experiment and co-centric with the beam axis.

FASER is an experiment specifically designed for this purpose, it is in fact being built in the TI12 tunnel located 480 m downstream IP of the ATLAS experiment and with a bit of engineering work, is completely aligned with the collision beam axis. This inexpensive, small and revolutionary experiment now aims at detecting particles such as Dark photons, ALPs, Dark Higgs and many other models [18] .

3.1.1 Current design

The FASER detector needs to be capable of providing extremely sensitive and accurate results on whether or not it has been detecting a non-SM signal due to the possible low rate of events. It was initially designed to detect an electron-positron pair as the decay product of the Dark Photon and this motivates the current design:

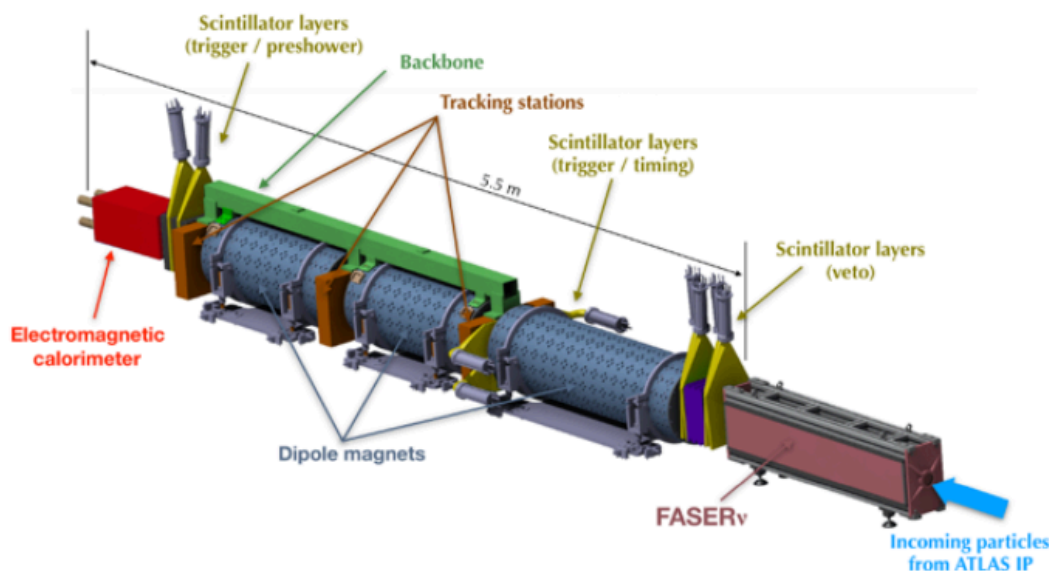


Figure 3.1: The FASER detector

The detector can be separated in different modules, each of them having their own purpose but also giving informations to the others in order to reconstruct signals. We will now describe each of them and understand how the detector works:

- **Scintillators:** There are 4 different scintillators stations, 2 in front of the detector composed themselves by 2 scintillators oriented one with respect to the other with a 90° angle, one after the first magnet and tracker station and one after the third magnet and third tracker.

The first two stations are mainly used for veto in order to know if any charged particle entered FASER and the last two are used for triggering and timing. These are plastic scintillators enabling for fast response but also have a large attenuation length meaning a minimal energy loss due to their small thickness. Each scintillator is linked to a Photo Multiplier Tube (PMT) used for collecting the light and producing gain to the signal.

- **Magnets:** The magnets are present in the number of 3 in the FASER detector. The aim of having magnets is to be able to separate the tracks of charged decay products, mainly the electron-positron pair (or more rare muon anti-muon pair) coming from a Dark Photon decay. The magnets should be strong enough inside the detector to separate the high energy collimated pair of charged particles but low enough outside to not affect the readout of other stations.
- **Tracker:** There are 3 tracking stations in total, one after the first magnet, one after the second magnet and one after the third magnet. These stations are mainly used in order to find the trajectories of the charged particles being bent by the magnetic field inside the detector. The modules used are SemiConductor strip Trackers (SCTs) also used in the ATLAS experiment. Such modules have a $17 \mu m$ resolution in one direction and a $580 \mu m$ resolution in the other direction which allows precision measurement of the tracks in the bending plane for charged pairs.
- **Calorimeters:** There are, at the end of the FASER detector, a set of 4 electromagnetic calorimeters, also used in the LHCb experiment for energy measurement. These modules need to be able to absorb particles with energies going from a 100 GeV to a few TeV and for this reason a sampled calorimeter with lead and scintillator cumulating 25 radiation length has been chosen. One PMT is connected to each calorimeter in order to collect the signal and measure the total energy deposited in the 4 calorimeters.

All of the different modules are not only designed to track and measure the energy of possible Dark Photon decays but are also used to make sure that the signal observed is a non-SM signal. In fact many sources of background can alter the measurement such as:

- i) Off-orbit protons hitting the beam pipe aperture in the dispersion suppressor or beam-gas interactions which can lead to particles entering FASER without crossing any material and mimic the desired signatures [18].
- ii) Highly energetic muons coming from the ATLAS IP either interacting with the material in between the 2 detectors and creating through bremsstrahlung photons or via pair production and photo-nuclear interactions resulting in electromagnetic and hadronic showers (but always accompanied by the parent muon) or simply entering FASER without interacting [18] .
- iii) Highly energetic neutrinos coming from charged pion decays, generating a few events through charged currents interaction with nuclei. Such events will leave a single high energy track[18] .

One can then understand why the trackers with good spatial resolution but also the scintillators stations are essential, not only to measure the desired signals, but also to veto the undesired ones. Anytime the veto station in the front of the experiment will fire, this implies an electrically charged particle entering the detector resulting in an unwanted signal from the different sources listed above. Also, any signal composed of a single track will be discarded. Some background studies have also been performed and FASER's location is in fact one of the quietest in term of background coming from off-orbit protons and beam gas interactions. Thanks to the bending magnets of the LHC, muons flux is not concentrated at the entrance of the detector inside the TI12 tunnel, resulting in less events coming from this source too [20].

3.1.2 Non-charged decays

The FASER detector in its current status is perfectly designed in order to identify two charged tracks like an electron-positron pair or muon anti-muon pair but it is quite obvious to realise that it would be almost blind to a pair of neutral particle like a pair of photons. If one was to look for such events, it would only see energy deposition in the calorimeters at the end of the detector but would not be able to distinguish whether there were only one photon or two or even more.

As one would have certainly understand, the model on which this thesis will be focused is an ALP model and the aim will now be to understand how such models can be probed with FASER. We will see in the next section that the main channel for ALP decays is a di-photon decay meaning one cannot take full advantage of the present detector design to observe such signals. One could still argue that having a large energy deposition in the calorimeters would be sufficient but not being able to distinguish a one photon event from a di-photon event raises the problem of the quality of the signature. This is due to the background to single photon events being significant as we explained before and hence making this detection technique less clean than a di-photon events for which the background is essentially negligible [16]. It has become obvious from now that the FASER detector has no sensitivity at all to di-photon events which makes inevitable an improvement of the current detector design if one wants to also probe ALP models. Before going any further, let's come back a moment to the theory of ALPs to have a better understanding of what exactly we are looking for.

3.2 ALPs phenomenology

As we mentioned before, there exist many different models predicting ALPs, each of them providing their own features and specificities. It has already been proven by [21] that for models in which an ALP couples to photons only, the main production mechanism leading to signals inside FASER is the Primakoff process. It is characterized by a photon, coming mainly from pion decays, themselves coming from IP of ATLAS, interacting with the material in between the two experiments and producing through interaction with nuclei an ALP. This later can then reach FASER and possibly decay within the detector through the main decay channel, a di-photon decay.

This production mechanism has been tested through Monte Carlo (MC) simulations and have given for different possible masses of the ALP and couplings to photons, the reach of FASER for different separations between the two photons [21]. The contour lines on this plot have been made assuming no background and at least 3 detected events. We can already see from this figure that the bigger the distance required between the 2 photons, the smaller the portion of parameter space one can probe. Although this specific production mode of the ALPs makes FASER probe a large portion of the parameter space in the (mass-coupling) plane not yet probed, this might not be the exact process giving the best sensitivity.

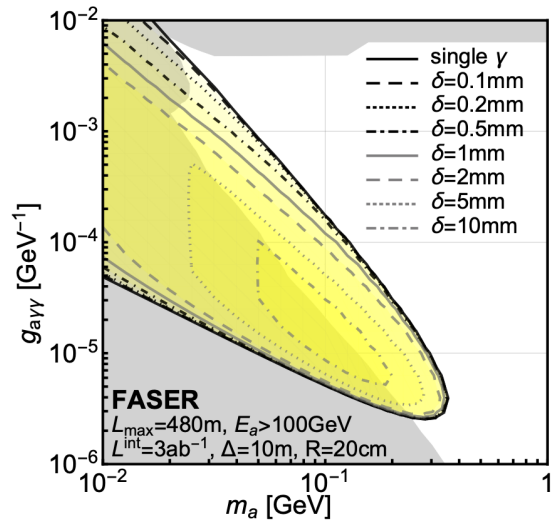


Figure 3.2: Photon induced ALPs in FASER

We will now move towards a different production process for an ALP which can also be coupled to the W^\pm and Z^0 bosons of weak interactions in which it is created from heavy meson decays.

3.2.1 Production from heavy meson decays

We recall from the previous chapter how ALPs couples to the SM gauge boson fields via the anomaly of the corresponding Peccei-Quinn symmetry, inducing terms in the Lagrangian like [16] :

$$\mathcal{L} \supset -\frac{g_{aVV}}{4} a V_{\mu\nu} \tilde{V}^{\mu\nu} \quad (3.3)$$

We have labelled as a the ALP field and $V_{\mu\nu}$ is the gauge boson field strength tensor for any of the SM vector bosons. There is no a priori reason why the ALP could not couple to any of the three SM gauge fields with the associated couplings determined by the gauge charges of the fermions fields responsible for the PQ symmetry anomaly.

Most of the time, only the coupling to photons and gluons is considered since these largely determine the rates of ALP interactions for energies below the electroweak scale. The coupling to the electroweak gauge bosons are in fact suppressed for energies such that $E < M_W$ resulting in very few ALPs produced via this channel [16]. Let's forget a moment about this and try to understand how ALPs could be produced through a coupling with the electroweak bosons.

The mechanism on which we will now focus is an ALP being emitted through Flavor Changing Neutral Current (FCNC) in which a down type quark becomes an up type quark and emits a charged boson which will itself radiate an ALP and then interacts with the up type quark which changes flavor again to become a down type quark. This process is called a flavour changing down type quark decay.

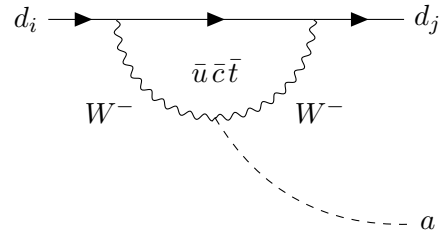


Figure 3.3: Feynman diagram for FCNC

We present in the figure 3.3 an example of this type of decay. Since the SM rates for such FCNC are highly suppressed by the GIM mechanism [22], this production channel for the ALP provides a striking signature with interesting prospects for discovery.

In this specific ALP Effective Field Theory (EFT), we consider for simplicity a model in which the ALP couples only to the field strength tensors of the $SU(2)_W$ group gauge boson which results in an effective Lagrangian as follows [16]:

$$\mathcal{L}_{EFT} = (\partial_\mu a)^2 - \frac{1}{2} M_a^2 a^2 - \frac{g_{aWW}}{4} a W_{\mu\nu}^a \tilde{W}^{a\mu\nu} \quad (3.4)$$

We have once again labelled as a the ALP field, M_a its mass, $W_{\mu\nu}^a$ the field strength tensor of the $SU(2)_W$ gauge bosons and g_{aWW} the coupling of the ALP field to the respective bosons.

After the ElectroWeak Symmetry Breaking (EWSB), this coupling generates interaction between the ALP and W^+W^- as well as ZZ , $Z\gamma$ and $\gamma\gamma$ in ratios given by the weak mixing angle. It can be shown that the contribution to the amplitude of ALP production through FCNC with down type quark decay is given by the following effective interaction term in the Lagrangian [16]:

$$\mathcal{L}_{d_i \rightarrow d_j} \supset -g_{ad_i d_j} (\partial_\mu a) \bar{d}_j \gamma^\mu \mathcal{P}_L d_i + h.c. \quad (3.5)$$

It can be shown that the decay width of such process is given by the following expression [16]:

$$\Gamma(K^\pm \rightarrow \pi^\pm a) = \frac{M_{K^\pm}^3}{64\pi} |g_{asd}|^2 \left(1 - \frac{M_{\pi^\pm}^2}{M_{K^\pm}^2}\right)^2 \lambda^{1/2}(m_{K^\pm}, m_{\pi^\pm}, m_a) \quad (3.10)$$

The last meson decay we will investigate here is the neutral Kaon decay such as $K_L \rightarrow \pi^0 a$. The figure 3.6 shows the Feynman diagrams in which a K^+ meson sees its anti-strange quark decay through FCNC into an anti-down quark resulting in the production of an ALP and positively neutral Pion π^0 .

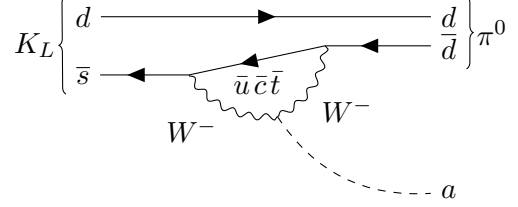


Figure 3.6: B-meson decay

It can be shown that the decay width of such process is given by the following expression [16] :

$$\Gamma(K_L \rightarrow \pi^0 a) = \frac{M_{K_L}^3}{64\pi} \text{Im}(g_{asd})^2 \left(1 - \frac{M_{\pi^0}^2}{M_{K_L}^2}\right)^2 \lambda^{1/2}(m_{K_L}, m_{\pi^0}, m_a) \quad (3.11)$$

We also have defined in the four above decay rates, the phase space factors $\lambda(m_{B^\pm}, m_{K^\pm}, m_a)$, $\lambda(m_{B^\pm}, m_{K^{*\pm}}, m_a)$, $\lambda(m_{K^\pm}, m_{\pi^\pm}, m_a)$ and $\lambda(m_{K_L}, m_{\pi^0}, m_a)$ that we can define in a general way as:

$$\lambda(m_1, m_2, m_3) = \left[1 - \frac{(m_2 + m_3)^2}{m_1^2}\right] \cdot \left[1 - \frac{(m_2 - m_3)^2}{m_1^2}\right] \quad (3.12)$$

One can also write the branching fractions for all of the above mentioned decays, which we will use in the following section, as [23]:

$$\begin{aligned} \mathcal{B}(B^\pm \rightarrow K^\pm a) &\simeq 2 \cdot 10^4 \times g_{aWW}^2 f_0^2(M_a^2) \lambda^{1/2}(m_{B^\pm}, m_{K^\pm}, m_a) \\ \mathcal{B}(B^\pm \rightarrow K^{*\pm} a) &\simeq 2 \cdot 10^4 \times g_{aWW}^2 A_0^2(M_a^2) \lambda^{1/2}(m_{B^\pm}, m_{K^{*\pm}}, m_a) \\ \mathcal{B}(K^\pm \rightarrow \pi^\pm a) &= 10.5 \times g_{aWW}^2 \lambda^{1/2}(m_{K^\pm}, m_{\pi^\pm}, m_a) \\ \mathcal{B}(K_L \rightarrow \pi^0 a) &= 4.5 \times g_{aWW}^2 \lambda^{1/2}(m_{K_L}, m_{\pi^0}, m_a) \end{aligned} \quad (3.13)$$

We have now described how ALPs with couplings to the $SU(2)$ gauge bosons can be produced from heavy-flavor mesons and we also have derived the corresponding decay rates but also branching fractions for B^\pm , K^\pm and K_L mesons. The next logical step is to now understand how ALPs decay into SM particles and hence what we will be looking for with FASER.

3.2.2 Decay into di-photons

Let's recall that after EWSB for the Lagrangian of our Axion model discussed above, coupling to $\gamma\gamma$ arise and the coupling of the ALP to photons is linked to the one of the ALP to WW as follows:

$$g_{a\gamma\gamma} = \sin^2(\theta_W) \cdot g_{aWW} \quad (3.14)$$

We have used in the equation 3.14 the definition of Weinberg's angle responsible for the quark mixing such that $\sin^2(\theta_W) \simeq 0.22$ [6]. In such a model, ALPs will dominantly decay into di-photons with decays into SM fermions are highly suppressed [16]. One of the sub-leading decays channel is the one in which the ALP decays into one real and one virtual photon, further decaying

into an electron-positron pair with a branching fraction of the order of $\mathcal{B} = (a \rightarrow \gamma e^+ e^-) \simeq 1\%$. For the primary ALP decay channel, the decay width is given by:

$$\Gamma_a(a \rightarrow \gamma\gamma) = \frac{g_{a\gamma\gamma} m_a^3}{64\pi} \quad (3.15)$$

The cubic dependence on the mass of the axion is a consequence of the dimension-5 operator which mediates the di-photon decay for the axion. This means that as the ALP mass will increase the its lifetime will rapidly decrease. We can hence write the decay length of the ALP as follows:

$$\bar{d}_a = \frac{c}{\Gamma_a} \gamma_a \beta_a \quad (3.16)$$

It has been shown by [17] that for masses of the ALP in the range of MeV to GeV, the branching fraction of any decay of an ALP into SM particles is entirely given by the $\gamma\gamma$ decay channel.

We present on the figure below, on the left side the decay length of the ALP with respect to its mass and in the right side, the branching fraction of the ALP to $\gamma\gamma$ but also to $\gamma e^+ e^-$. This once again confirms that for masses in the MeV- GeV range, the di-photon decay is the principal channel.

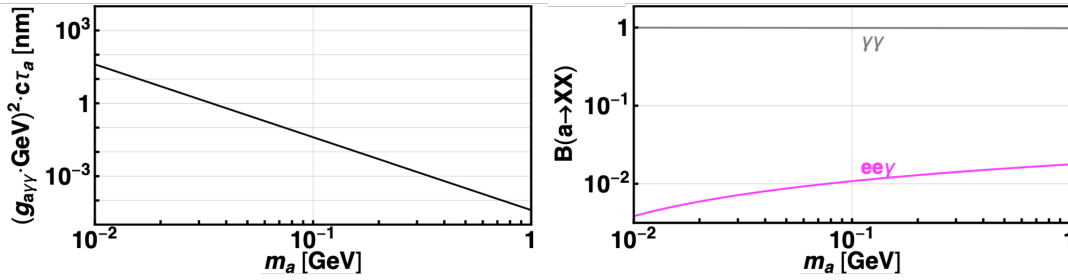


Figure 3.7: Decay length and branching fraction as a function of the mass

With respect to the decay length, one has to pay attention to the fact that the result is dependent on the coupling, if one increases the coupling, the decay length will decrease and vice-versa.

It is now interesting to understand the kinematics of the decay of the ALP to di-photons. In the rest-frame of the ALP, the two photons will decay back-to-back with completely random angles but since ALP is highly energetic, the boost one need to apply to have the kinematics of the decay in the lab-frame is significant. For now we will reserve this discussion of the angles for the a future discussion. Although we can still derive the relation between the angle in the rest-frame of the ALP and the lab frame using relativistic kinematics.

Another consequence of the momentum conservation is, as we said before, that the two photons have to be emitted back-to-back which give us the following conditions:

$$\vec{p}_{\gamma,1} = -\vec{p}_{\gamma,2} \Rightarrow |\vec{p}_{\gamma,1}| = |\vec{p}_{\gamma,2}| \quad (3.18)$$

These two previous relations allows us to give the relation between the angles in the rest frame for the decay of the two photons and the angles of each photon in the lab frame. In order to do that one has to apply a Lorentz boost in the direction of the momentum of the ALP. If we consider that the boost one needs to apply is in the \hat{x} direction, the momentum of the photons will become:

$$\vec{p}_{\gamma,1} = \begin{bmatrix} \gamma(p_{x,1} - \beta|\vec{p}_{\gamma,1}|) \\ p_{y,1} \\ p_{z,1} \end{bmatrix} \quad ; \quad \vec{p}_{\gamma,2} = \begin{bmatrix} \gamma(p_{x,2} - \beta|\vec{p}_{\gamma,2}|) \\ p_{y,2} \\ p_{z,2} \end{bmatrix} \quad (3.19)$$

As a first step, we can write the four-vectors respectively of the ALP, the first photon and the second photon as follows:

$$p_{ALP}^\mu = \begin{bmatrix} m_a \\ 0 \\ 0 \\ 0 \end{bmatrix} \quad p_{\gamma 1}^\mu = \begin{bmatrix} 0 \\ p_{x,1} \\ p_{y,1} \\ p_{z,1} \end{bmatrix} \quad p_{\gamma 2}^\mu = \begin{bmatrix} 0 \\ p_{x,2} \\ p_{y,2} \\ p_{z,2} \end{bmatrix} \quad (3.17)$$

Here we consider a decay in three dimensions ruled out by the two angles θ and φ the angles for the momentum of the photons as shown in the figure 3.8 .

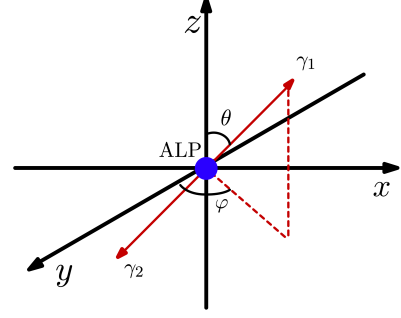


Figure 3.8: ALP decay

We can then start here by writing the angle φ in the lab frame for one of the two photons as:

$$\tan(\varphi'_{\gamma,1}) = \frac{p'_{y,1}}{p'_{x,1}} = \frac{|\vec{p}_{\gamma,1}| \sin(\theta) \sin(\varphi)}{\gamma (|\vec{p}_{\gamma,1}| \sin(\theta) \cos(\varphi) - \beta |\vec{p}_{\gamma,1}|)} = \frac{\sin(\varphi)}{\gamma \left(\cos(\varphi) - \frac{\beta}{\sin(\theta)} \right)} \quad (3.20)$$

In order to find the angle $\varphi'_{\gamma,2}$ one has to use the equation 3.20 and the conservation of momentum as well as substituting $\varphi \rightarrow \varphi + \pi$. We can also do the same procedure for the angle θ which will give:

$$\tan(\theta'_{\gamma,1}) = \frac{\sqrt{p'^2_{x,1} + p'^2_{y,1}}}{p'_{z,1}} = \frac{\gamma \sqrt{\sin^2(\theta) - 2 \sin(\theta) \cos(\varphi) \beta + \beta^2}}{\cos(\theta)} \quad (3.21)$$

Once again, to find the other angle for the other photon $\theta'_{\gamma,2}$ one simply has to use the equation 3.21 and the conservation of momentum as well as substituting $\theta \rightarrow \theta + \pi$.

Now that the angles in the lab frame after the Lorentz boost are known, it is straight forward to determine the components for the momentum of each of the two photons in this reference frame. It will then give the type of kinematics, a detector aiming at detecting ALPs decays into di-photon, should be sensible to.

3.3 The Pre-Shower module

Before going any further into the event rates accessible with FASER for di-photon ALPs signal from their decay, we can investigate the design of the possible upgrade of the current detector to enhance the detection of this specific decay. We will present in what follows, the work made by the University of Geneva to propose a Pre-Shower (PS) module, which would hypothetically inserted after the end of the decay volume, in between the last tracking station and the calorimeters, to enhance the ALPs decay detection.

3.3.1 Design of the PS module

The proposed PS will be composed of essentially two types of objects:

- Planes of monolithic silicon pixel detectors in Silicium Germanium (SiGe) BiCMOS technology with a $100\ \mu\text{m}$ pixel pitch,
- Radiator layers of one radiation length (X_0) of tungsten.

The aim of the radiator layers are to make the photons convert and initiate an electromagnetic (EM) shower through pair production mainly due to the high energy photons. The aim of the planes of pixel detectors will then be to detect all of the charged particles produced in the EM shower and to reconstruct it to identify the number of showers and hence the number of photons. To understand how many layers of radiators but also how many planes of pixel detectors were needed, some GEANT4 simulations were performed using different configurations going from $4X_0$ to $6X_0$ and 4 to 6 pixel planes. The simulations were made for photon pairs generated for all the combinations of energy and spatial separation between the photons belonging to the following lists:

$$E_\gamma = [0.25, 0.35, 0.45, 0.75, 1, 1.5, 2, 3.5] \text{ TeV} \quad ; \quad \delta_{\gamma\gamma} = [0.2, 0.3, 0.5, 1, 2] \text{ mm} \quad (3.22)$$

The aim of the simulation was to shoot several pairs of photons for all of the different possible combinations of the lists 3.22, using the "particle gun" and to obtain the efficiency of the different configurations of the PS module to determine the performance of each of them. Nonetheless, the layout of the detector is not the only factor contributing to the performance, the reconstruction of the EM showers through measurement of the charge deposited in each pixel is another key aspect. A simple photon-reconstruction algorithm was developed to reconstruct the positions throughout the layers of the photons and to identify in which layer they converted.

The study showed that the best configuration for the detector was to have six layers of $1\ X_0$ of tungsten, each followed by a layer of pixel detectors with a $100\ \mu\text{m}$ pitch providing the needed performance over the photon energy range studied. We present on the figure 3.9 the charge deposition in fC in each of the $100 \times 100\ \mu\text{m}^2$ area pixels in the sixth layer of the PS. The photons had energy of 750 GeV and 1.5 TeV, initially generated at a distance of $200\ \mu\text{m}$ from each other. The result shows the algorithm is capable of identifying the two photons tracks for these conditions.

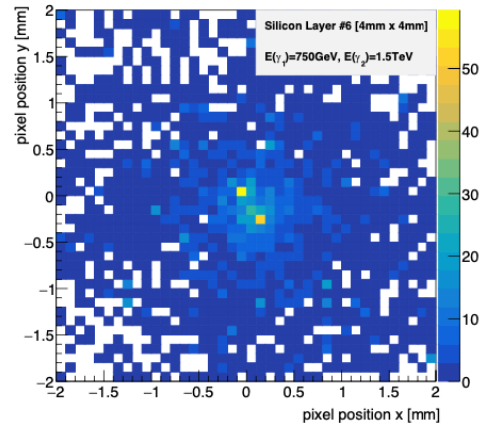


Figure 3.9: Photon reconstruction

Another interesting thing to do, still using the same algorithm is to shoot single photons instead of two photons and understand what is the rate at which a single photon is reconstructed as two. The study have given a fake rate of 2% for energies below 1 TeV and a fake rate of 4% for energies above 1 TeV.

We now have all of the tools we need to start and investigate possible ALPs signals reaching FASER but also possibly decaying within FASER's volume and providing observable SM decays. The aim will be to go through the study of how many ALPs can be generated from the meson decay different channels, themselves coming from the ATLAS IP, but also to understand how many of these generated ALPs can reach FASER and decay within its volume. After knowing the rates of events, another interesting step to take is to study the topology of the events, the spectrum of energy of the photons but also their separation when reaching the described above new module in the FASER detector design, the PS. The best approach for such studies is a MC simulation which will be the heart of the upcoming discussion.

Chapter 4

Monte-Carlo simulations for ALPs in FASER

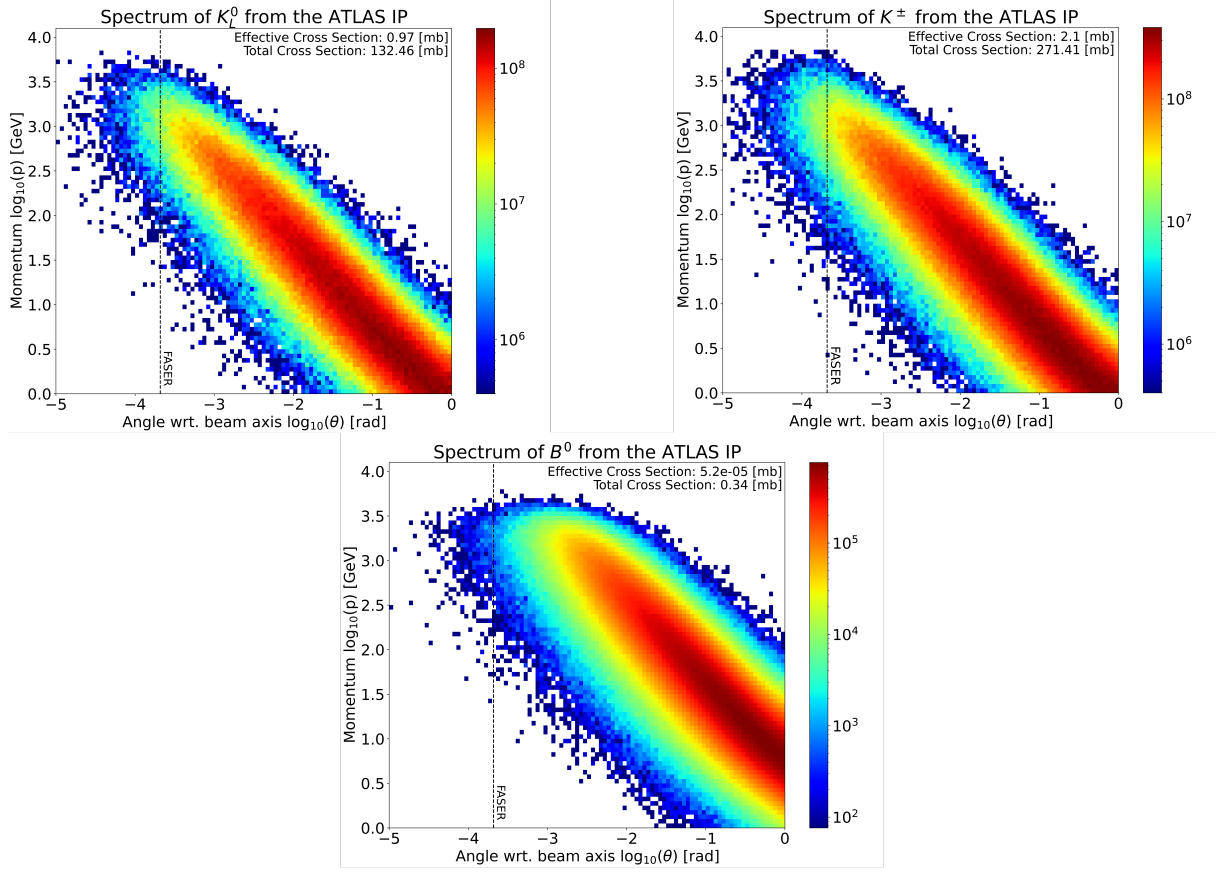
The description of the phenomenology of the ALPs production and decay being completed, the discussion will now move towards the MC simulations with the final aim of having, like for the other production processes of the ALPs like through Primakoff process discussed by [17], the reach of the FASER detector. We will in the following section more precisely focus on the production rates and number of events for specific periods of data taking during the Run 3 of the LHC since the reach plot cannot be given without specifying the FASER upgrade required to enhance sensitivity to di-photon signals.

4.1 Meson spectrums from ATLAS IP

The very first and essential step one has to make is the study of the meson spectrums from the ATLAS IP, emitted in the very forward direction towards the FASER detector. In the MC simulations we will produce, the interest is not modeling the proton-proton interactions at the IP and hence the spectrum are used as an input of our simulations. For the mesons in which we are interested, the spectra will be given by some MC generators like EPOS LHC [24] for the light mesons as K^\pm , K_L and for the heavier B^\pm mesons the MC generator which will be used is Pythia [25].

The spectrums are stored as a two-dimensional histogram in a text file, with 3 columns namely the momentum of the meson, the angle with respect to the line of sight at which this meson is emitted and the associated cross section for this particular category of meson (having this momentum and this angle).

On the three figure in 4.1 we present the spectrum for each of the mesons involved in the MC simulation, we can see as a dashed black line the acceptance of FASER which represents the limit of the spectrum accessible for the detector (not yet accounting for the angle at which the ALP will be emitted after the decay). We can see on the top right corner of each plot, the total cross section for the LHC at 14 TeV but also what we have called the effective cross section which corresponds to the cross section only for the mesons in FASER's acceptance. The histograms is scaled in unit of cross section (pb) per bin giving the colormap on the right side of each spectrum.


 Figure 4.1: The K^\pm , K_L and B^\pm spectra

4.2 Mesons decays into ALPs

Now that we know the cross section for each meson type and that we have the mesons spectrums, the next logical step is to study the decay of each of these mesons into ALPs. As we have seen previously, what will determine the rate of the ALPs signals is the branching fractions we have previously developed for each of the mesons of interest. Regarding the parameter in these branching fractions, two of them are free parameters, the ALP mass m_a and its coupling to the $SU(2)_W$ gauge bosons g_{aWW} .

A key aspect of the following MC simulations which will be performed is the fact that none of these parameters are known and except having lower and upper bounds from other experiments, the values of the mass and the coupling could take any value in the not yet excluded ranges. In order to study ALP signals in FASER, one then has to simulate many slightly different ALP models each time with different couplings and masses in order to have access to the reach of the detector in question. The final aim is as we said before to obtain the reach of the FASER detector for such ALP model as a function of the mass m_a and the coupling g_{aWW} of the ALPs.

The first part of the MC simulation then takes as an input, the mass of the ALP m_a , the coupling g_{aWW} and the mesons spectrums and return the ALP spectrum in the momentum-angle with respect to beam axis plane as for the mesons. Let's describe in more details the procedure:

- i) The very first step is to understand, with respect to the mass of the ALP, from what mesons this previous can originate. In fact during the decay, if the sum of the masses of

the decay products is greater than the mass of the incoming meson, then the ALP can't be coming from the decay of that specific meson since it would violate the energy-momentum conservation.

- ii) If the decay is allowed, the meson spectrums needed are loaded from the text files, with the angles, momentum and weight associated to each bin in the spectra presented above. Instead of using the term cross section for each bin, we will here use weight since it is more suited for a discussion on MC simulations. The variables are then transformed from the files to obtain the energy of the meson, its transverse momentum and momentum along the \hat{z} direction using the following equations:

$$E = \sqrt{|\vec{p}|^2 + m^2} \quad ; \quad p_z = |\vec{p}|^2 \cos(\theta) \quad ; \quad p_t = |\vec{p}|^2 \sin(\theta) \quad (4.1)$$

Since the angle φ giving the components along the \hat{x} and \hat{y} axis are not known, a MC sampling is performed for enhanced statistics, using a random uniform function in the range $[-\pi, +\pi]$ such that the missing components can be written as:

$$p_x = p_t \cos(\varphi) \quad ; \quad p_y = p_t \sin(\varphi) \quad (4.2)$$

If the φ angle is sampled a total number of n times for a meson with specific weight w , after the MC sampling, this will create a number of n mesons with different φ angles and with a weight $w' = \frac{w}{n}$ such that summing the weights for each of the MC sampled mesons will give the initial weight of the specific meson.

The information relative to the mesons kinematics (i.e. its energy and momentum) are stored in a Lorentz vector object. The meson spectrum is then reshaped into two lists: one with the Lorentz four-vector of the particles and one with the associated weight.

- iii) One can now apply the decays of these mesons in its rest frame and using the relativistic kinematics, it will give the Lorentz vector of the decay product among which there is the ALP. Once again, the angles for the decay in the rest frame are given by a MC sampling, since they can be completely random with no preferred direction. To determine the values we used two random uniform distributions, one in the range $[-1, 1]$ for the value of the cosine of the angle θ and one in the range $[-\pi, +\pi]$ for the angle φ . The aim here is to again enhance the statistics on the decay. The weight associated to each of the mesons will be determined the same way as previously for a number of m samples this time.

According to the mesons and from which the ALP is originated, the mass m_a , the coupling g_{aWW} and the weight associated to the specific mesons in the meson spectrum, the weight associated to ALP generated is the the product of the probability that the mesons decays times the probability that it decays into a final state with an ALP times the original weight of the meson:

$$w_{ALP} \rightarrow w_{\text{meson}} \cdot w_{\text{meson decay}} \cdot \mathcal{B}(\text{meson} \rightarrow Xa) \quad (4.3)$$

This formula gives the weight associated to the ALP or abolishing the MC simulations nomenclature, the cross section of the ALP originating from a specific meson. In order to also have the kinematics of the ALP, not in the rest frame of the decayed meson but in the lab frame, one has to apply the Lorentz boost associated to the kinematics of the meson.

- iv) The final step is to reshape the simulated data into three lists: one for the momentum of the ALP, one for the angle with respect to the beam axis and one for the weight associated to each pair of (momentum-angle). The motivation here is to have the same file structure as the one for the mesons spectrums. The way this reshaping is performed is by using

an histogram to represent the spectra of the ALP in the (momentum-angle) plane and to associate to each bin a certain weight. The histogram is then transformed into the three lists above but this induces, due to the binning chosen for the histogram, a diminution of the precision as well as the statistics.

For the simplicity of the simulations, the coupling of the ALP g_{aWW} is taken to be $g_{aWW} = 1$ in this part which allows for creating only ALPs with a certain mass. In fact this is not an issue at all since the coupling appears as a weighting factor in the cross section for each ALP meaning that it can be taken into account later. A contrario the mass is crucial in the generation of the ALP spectra since it plays an important role in the kinematics of the decay. For this reason, the contribution of the coupling in the branching fraction for the mesons decays through FCNC, will be taken into account in the second part of the MC simulations.

Another point which was not taken into account here for the rest of the MC simulations is the distance traveled by the mesons before decaying since due to their small lifetimes, these previous will not travel a significant distance before decaying with respect to the distance which separates the ATLAS IP from the entrance of the FASER detector.

4.3 ALPs decays within FASER

The spectra of the ALP model with different masses have now been obtained and the logical steps which follows is the decay of the ALP into two photons. This part here is by far the most complicated of the MC simulations, one has to take into account the geometry of the FASER detector, making a selection on the spectra of the ALP due to its acceptance, but also the decay length of the ALP, its branching fraction and the kinematics of the decay in order to finally obtain the kinematics and rates of the SM final states.

The second part of the MC simulations takes as an input the ALP spectra computed in the first part of the MC simulations, the coupling g_{aWW} of the ALP, the length of the decay volume for ALP in the FASER detector, its distance from the ATLAS IP, its radius and finally the integrated luminosity at which one aims for the data taking. The output of the simulations can have different shapes according to the final aim of the MC simulation but we will discuss this later. We will now describe into details the procedure:

- i) The initial step is to specify the geometry of the detector which includes its radius and length as it can be simply represented, for the purpose of this study, as a cylinder. The mass of the ALP studied is then specified as well as the coupling associated to it and the integrated luminosity for the expected data taking. Another parameter here is introduced which we will call the *smearing* parameter.

We recall from the first part of the MC simulations that when the data for the ALP spectra was put into an histogram and then exported as three lists, one for the momentum, one for the angle with respect to the beam axis and one for the weight associated to each bin, it generated some degradation on the precision as well as the statistics.

While loading the the ALP spectra, i.e. the three lists we mentioned above, the aim is to transform back this information into two list, one with the Lorentz vector for each of the specific ALP with certain momentum emitted at a certain angle and a second one with the weight associated to it. Although, instead of simply extracting the spectrum and transforming it, each time a couple (momentum-angle) is read from the file, the value for the angle as well as the momentum is smeared according to the *smearing* parameter.

What the smearing concretely does is instead of having only one ALP with certain momentum and angle, it generates many ALP with slightly different angles and momenta, the number of times this smearing is performed is given by the *smearing* parameter. The way this smearing is done is through the multiplication of the momentum and angle of the ALP by a smearing factor given by a random uniform distribution, centered around 1 with a standard deviation of $\sigma = 0.05$. This allows for compensating the discretization which happened in the first part of the MC simulations and renders the ALP energy spectrum as well as its spatial distribution, smoother.

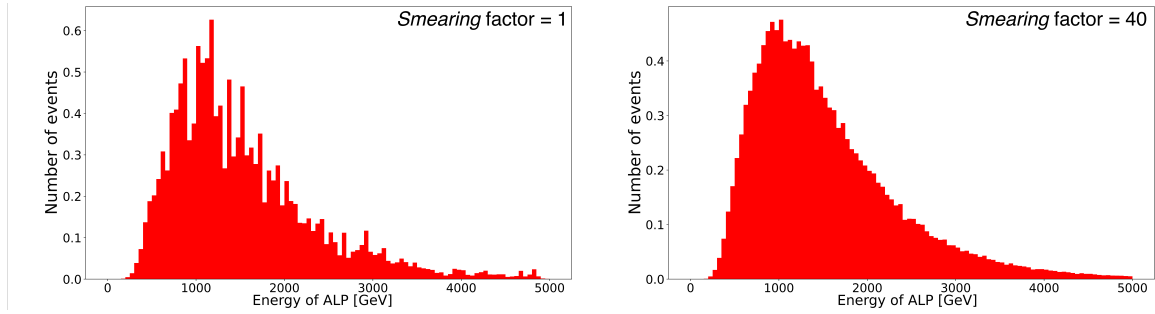


Figure 4.2: Effect of the smearing on the ALP energy distribution

We present in the figure 4.2 the effect of the smearing of the momentum of the ALP by showing how the energy distribution of the ALP changes with different values of the *smearing* parameter. The result is as expected and shows a smoother distribution for larger values of the *smearing* parameter.

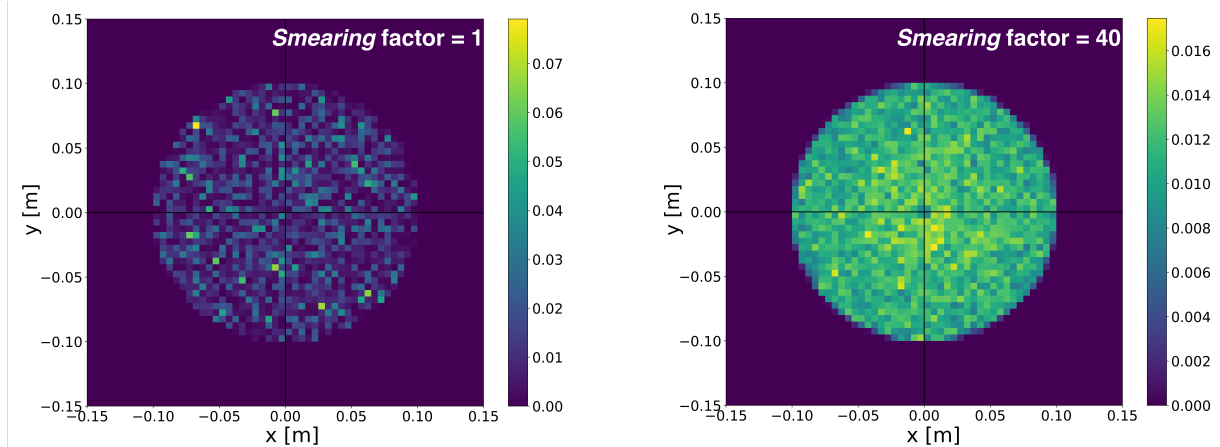


Figure 4.3: Effect of the smearing on the ALP spatial distribution

Another way to observe the effect of the smearing is through the spatial distribution of the ALP at the end of the decay volume of the FASER detector. Once again the observed effect is shown in 4.3 is a smoother distribution for higher values of the *smearing* parameter.

One has to be really attentive when doing this kind of procedures because a counter part of it can be to completely change the initial data set. In fact the tricky part is that when putting the ALP spectrum into an histogram, the bins were equally spaced in logarithmic scale and so the sizes of the bins in linear scale are much smaller for low values of momentum and angles than for larger values. In order to account for this, the values of the momentum and the angle themselves are smeared by a factor and not by adding or subtracting a

constant to it, whatever the initial value was. Also, since the data is stored in logarithmic scale the smearing has to be performed on the values in logarithmic scale and not on the values in linear scale.

After the smearing, the only variables provided by the ALP spectra is the energy of the ALP, its transverse momentum and momentum along the \hat{z} axis but not the components along the two others directions. In fact, the problem is here the same as the one we encountered while loading the files in which the mesons spectra were stored. As before, a MC sampling of the angle φ is performed since once again this angle can take any value in the range $[-\pi, +\pi]$. For simplicity this MC sampling is done at the same time at which the smearing is so that the sampling is performed as many times as the smearing is performed.

- ii) Before even decaying the ALP into two photons, one can already compute the weight associated to each of the ALP decay from the list of Lorentz four-vectors. The first factor taken into account is the previously ignored coupling g_{aWW} which was set equal to one in the first part of the MC simulations. The second factor that has to be taken into account is the probability that the ALP decays inside FASER's decay volume. This probability depends on the decay length of the ALP we have defined above, which depends itself on the coupling of the ALP to photons, the mass of the ALP and its momentum. The decay probability can then be written as:

$$\mathcal{P}_{decay} = \exp\left[-\frac{L}{\bar{d}_a}\right] - \exp\left[-\frac{(L+l)}{\bar{d}_a}\right] \quad (4.4)$$

We have labeled in the equation 4.4 the decay length of the ALP \bar{d}_a , the distance between the ATLAS IP and the entrance of the FASER detector $L = 480\text{m}$ and the length of the decay volume $l = 3.5\text{m}$.

After this factor, comes into account the branching fraction for the ALP decay into di-photon which we previously discussed to be one. Finally comes the integrated luminosity for which one aims for the data taking. This changes the weights associated to each ALP (which was also the cross section associated) into the number of events for this specific ALP. We can then write the number of events N as:

$$N = g_{aWW}^2 \cdot w_{ALP} \cdot \mathcal{B}(a \rightarrow \gamma\gamma) \cdot \mathcal{P}_{decay} \cdot \mathcal{L}_{int} \quad (4.5)$$

On top of this, a discrete selection is performed on the initial spectrum itself. In fact if the angle at which the ALP is emitted from the ATLAS IP is greater than the angle corresponding to the acceptance of the FASER detector then it is not taken into account in this part of the simulation.

Another discrete selection is performed on the momentum of the incoming ALP requiring it to be above 100 GeV. This value seems to be completely arbitrary but it in fact makes sense knowing that there is a lot of material separating the ATLAS IP and FASER's location [21]. For the ALP to survive when going through this material it has been found that its momentum should be above a certain threshold which corresponds to this 100 GeV threshold [21].

In order to understand what is the impact of the momentum of the ALP on its decay position inside the decay volume of FASER, one can study the distribution of energy of the ALP as a function of the decay position given by 4.4:

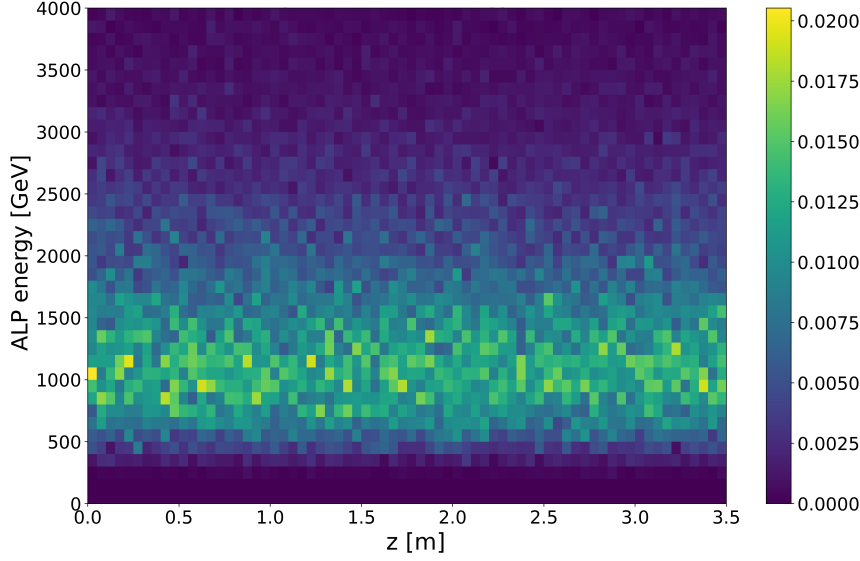


Figure 4.4: Decay distance of the ALP and energy distribution

The result is here quite obvious, the decay distance doesn't have a significant impact on the energy spectrum of the ALP and vice-versa. This means that more energetic or less energetic ALP will not decay much further or much closer. This is explained by the fact that when taking the probability of the decay as a function of the distance, FASER's location is in the regime of the tail of the distribution which means minimal change in the probability with respect to changes of distance. We will also show later that the mass of the ALP and its coupling does not have any impact on this distribution too.

The information about the number of events for each ALP is stored in a list as well as the information about distance traveled before decay of the ALP, its energy and the angle at which it is emitted.

- iii) The upcoming step is the one in which the ALPs decay into two photons. The kinematics of the decay in the rest frame of the ALP have already been discussed before. As previously said the two angles θ and φ involved in the kinematics of the decay are completely random and so the cosine of the angle θ is given by a random normal distribution in the range $[-1, +1]$ and the angle φ is given by a random normal distribution in the range $[-\pi, +\pi]$. Since the number of ALPs for which the simulation is performed has already been enhanced by the smearing of the distribution, a MC sampling of the angles for the ALP decay is not strictly needed but could have in fact been performed to increase even more the quality of the simulation.

Once the Lorentz four-vectors for the 2 photons are known in the rest-frame of the ALP, the components can then be boosted back into the lab reference frame according to the boost of the ALP. The angles at which the two photons are now propagating are really important, as well as the momentum in the three spatial direction as well since this information will help us determine the separation in distance between the two photons.

- iv) The final step of this second part of the MC simulations is to compute the relevant quantities which will be needed later on when doing the analysis of the di-photon signals. The first and most important quantity we'll discuss now is the spatial separation between the two photons when reaching the end of the decay volume.

The easiest way to compute the separation of the two photons is to compute for each of the two photons, the separation with respect to the \hat{z} axis in the transverse plane. Due to momentum conservation, there will always exist a plane in which the two photons's trajectories are contained which allows us to compute the separations of the two photons as explained on the figure 4.5. This computation relies on the fact that the boost of the ALP is almost entirely in the \hat{z} direction since the angles at which the ALPs are emitted are considerably small.

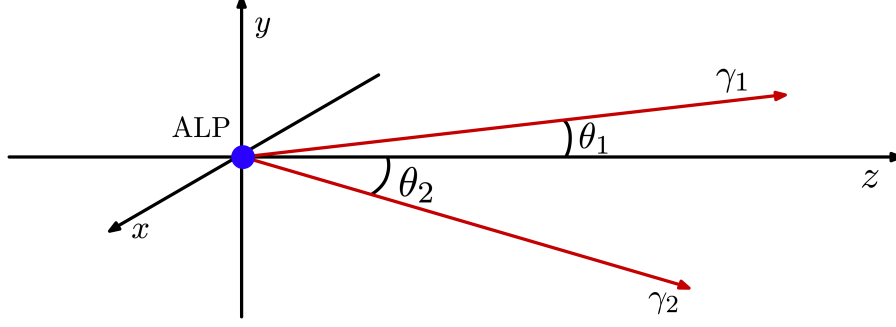


Figure 4.5: Di-photon separation from ALP decay

The angles in the plane in which the photons trajectories are contained can be obtained using the following equations:

$$\theta_i = \arccos\left(\frac{p_{z,i}}{|\vec{p}_i|}\right) \quad ; \quad |\vec{p}_i| = \sqrt{p_{x,i}^2 + p_{y,i}^2 + p_{z,i}^2} \quad \text{with: } i = 1, 2 \quad (4.6)$$

The total separation of the two photons at the end of the decay volume is then given by the following equation:

$$\delta_{\gamma\gamma} = [\tan(\theta_1) + \tan(\theta_2)] \cdot [l - z_{decay}] \quad (4.7)$$

We have here labeled as previously l as the length of the decay volume of FASER and what we have labelled as z_{decay} is the distance at which the ALP decays with respect to the entrance of the decay volume. The difference between these two distances then gives the distance between the point at which the ALP decays and the end of the decay volume.

Another important variable which gives a really interesting insight into the topology of the di-photon signals is the asymmetry between the energy of one of the photons and the energy of the other. We can then define the energy asymmetry as:

$$A_{\gamma\gamma} = \frac{|E_{\gamma,1} - E_{\gamma,2}|}{E_{\gamma,1} + E_{\gamma,2}} \quad (4.8)$$

In the case in which the energy of the two photons is the same the asymmetry will obviously be zero and it will be maximal when one of the photons carries all of the energy. This quantity is directly linked to the separation of the photons since what determines the energy of each photon are the angles of the decay in the rest frame of the ALP.

After computing the two above quantities for each of the Lorentz four-vectors for ALPs, all of the information about the ALP decays are known and ready to be stored into lists for further analysis. The saving scheme here is pretty simple and all of the following informations are stored in one list and grouped into 3 different lists:

- List n°1: Position along \hat{x} , Position along \hat{y} , Position along \hat{z} , Energy of the ALP and number of events associated.
- List n°2: Momentum along \hat{x} , Momentum along \hat{y} , Momentum along \hat{z} , Energy of first photon and Energy of second photon.
- List n°3: Energy asymmetry, Energy of less energetic photon and Separation between the two photons

An important aspect regarding this second part of the MC simulations is that it takes only an ALP spectra as an input which means the procedure is performed for one specific mass for the ALP. Nonetheless, it associates to that specific mass a wide range of couplings at the same time and so this part of the MC simulations returns for each combination of the mass of the ALP with all the couplings, all of the informations listed above.

This ends the discussion of the MC simulations for the rates and kinematics of the SM decays of the ALP within the FASER detector. Some intermediate results for a particular ALP with certain mass and coupling were shown above in order to better illustrate the procedure. The focus will now move towards the analysis of the output of the simulations to better understand the topology of the events but also to have a first insight into the type of upgrade the current FASER detector design would need to enhance the di-photon signal sensitivity.

4.4 Topology of di-photon signals

We remind that the aim of the performed simulations is to obtain in the mass and coupling parameter space for the ALP, the reach for the FASER detector. In order to understand for what range the values of the masses and the coupling have to be taken, an interesting step is to consider the already excluded regions by other experiments. This gives us the figure 4.6:

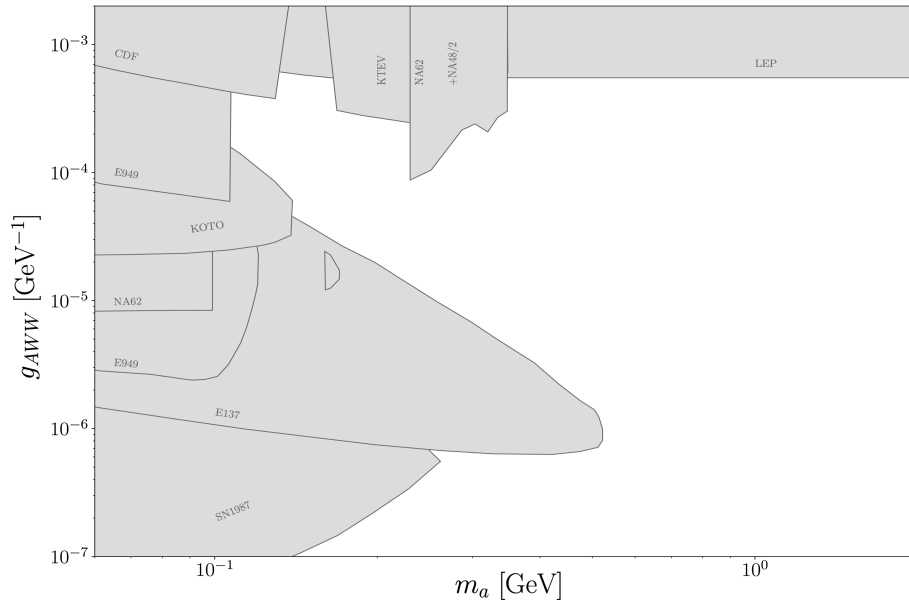


Figure 4.6: Portion of $(m_a - g_{aWW})$ parameter space already excluded

The aim will then be to probe as much of the non already covered area in the reach plot 4.6 and this allows us to define the following ranges for the mass of the ALP and couplings to $SU(2)_W$ gauge bosons as follows:

$$m_a \in [0.1 - 2] \text{ GeV} \quad \text{and} \quad g_{aWW} \in [5 \cdot 10^{-7} - 8 \cdot 10^{-4}] \text{ GeV}^{-1} \quad (4.9)$$

The values of the masses and the couplings for which the simulations have been performed were equally spaced in logarithmic scale and a total 44 values for the masses and 33 values for the couplings resulting in a total of 1452 ALP models probed.

The different points in the parameter do not have the same kinematics neither the same rates for the di-photons signals, we now want to orientate the discussion towards a qualitative analysis on the topology of the events. Since it would be a complete loss of time to present this analysis for all the (mass-coupling) points we will here choose three of them in order to understand the general trend without going to much into details. The chosen benchmarks points in the (mass-coupling) parameter space are then the following:

Id	m_a [GeV]	g_{aWW} [GeV $^{-1}$]
1	$1.65 \cdot 10^{-1}$	$1.8 \cdot 10^{-4}$
2	$2.08 \cdot 10^{-1}$	$1.0 \cdot 10^{-4}$
3	$3.20 \cdot 10^{-1}$	$3.2 \cdot 10^{-5}$

The first distribution one can study is the distribution of the energy of the ALP when it decays as a function of the position of the decay inside the decay volume of the FASER detector. We have shown previously that the energy of the ALP didn't have any significant impact on the decay position and we are now interested to know if the mass or the coupling has a significant impact on the decay position. The effect on the energy distribution will of course be important but the question is to understand wether the regime is still in the tail of the distribution for the decay probability or if it changed.

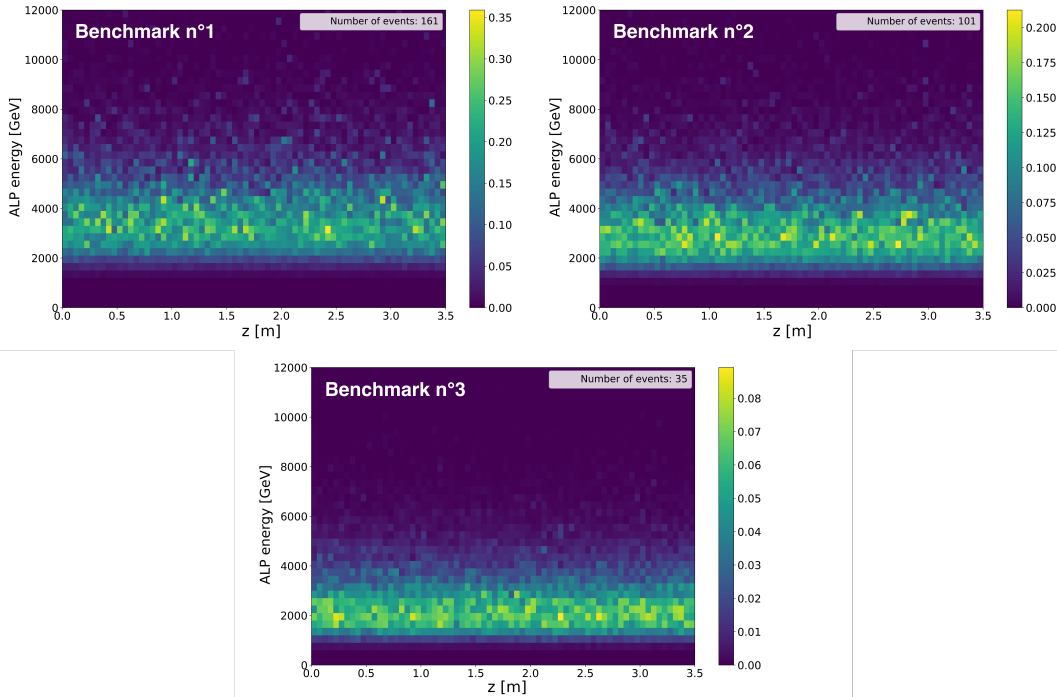


Figure 4.7: Distribution of decay position and energy of the ALP for the 3 benchmarks

We can see that the effect of the mass or the coupling does not have a significant impact of the decay distance distribution since it does not change over the full length of the decay volume. Of course as expected the distribution for the energy has changed for the three different benchmarks.

The second interesting distribution one can study is the spatial distribution of the ALP and the end of the decay volume. It is in fact important to know if the distribution is completely uniform or condensed at the center of the decay volume or more on the edges, in the transverse plane.

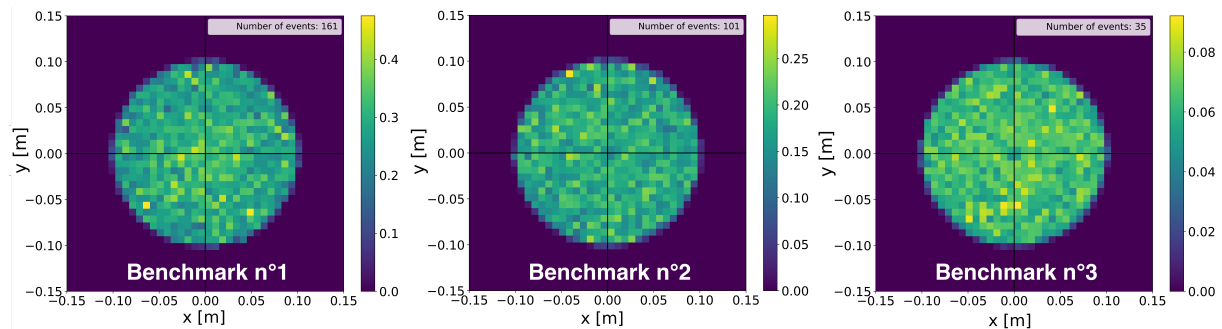


Figure 4.8: Spatial distribution in the transverse plane of ALP for the 3 benchmarks

The spatial distribution presented in 4.8 have the same profile for the three benchmark presented and it is uniform. There is not much to say about the consequences of the result here but we will further understand it when discussing the potential upgrade of the FASER detector design.

Let's now move towards the analysis of the characteristics of the ALP decay into two photons. As we have explained before, many different parameters have been computed in the second part of the MC simulations in order to better understand the topology of the signals. The first and most intuitive distribution one can study is the distribution of the energy of one of the photons with respect to the energy of the other photon as presented here:

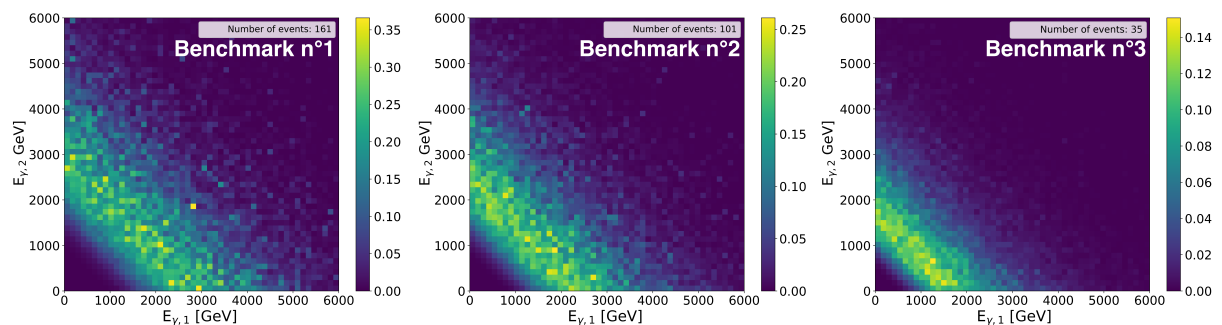


Figure 4.9: Distribution of the energy of the photons for the 3 benchmark

There are two interesting things one can notice in the three distributions presented in 4.9:

- There is a striking similarity which is, no matter the value of the coupling and the mass, which is that the shape of the distribution always looks the same. In fact the distribution of the signals is mostly present in what is called the asymmetric region and not in the symmetric region in which the energy of the photons would always be close to one another.

- Another striking difference is the spread of the energy of the photons, in fact for ALPs with smaller masses and higher couplings, the photons are much more energetic than for higher masses and smaller couplings.

To investigate further the asymmetric distributions in 4.9 an interesting procedure one can do is to apply a cut on the separation of the two photons when reaching the end of the decay volume. The aim here is to understand whether the asymmetric events are coming from close by photons or if it comes from much more separated photons. The best way to observe this is through a distribution in which the asymmetry of the energy of the photons, as defined previously, is compared to the separation between the photons.

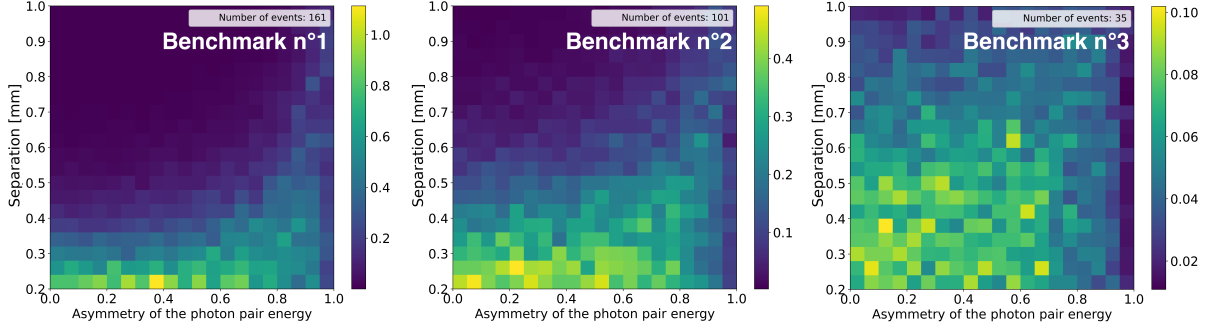


Figure 4.10: Distribution of the asymmetry compared to separation of photons for the 3 benchmark

There are again here two very interesting things one can notice while looking at the distributions in 4.10:

- The behaviour of the three benchmark presented above is similar from one to another in the sense that the more the energy of the photons is asymmetric and the more they are separated. This particularity can be understood by coming back for a moment to the ALP decay in its rest frame. When boosting back the Lorentz four-vectors for the photons in the lab reference frame, according to the angles associated to the decay, the situation can be that one of the photons is emitted almost in the direction of the boost resulting in the other photon being emitted in the almost opposite direction of the boost. This will result in having one of the photons carrying most of the energy and the other one being much less energetic. Due to energy and momentum conservation, it is easy to prove that the angle at which the less energetic photons is emitted has to be much bigger than the one for the most energetic photon which will provide a greater separation between the two photons.
- The second interesting fact is that for larger values of mass and smaller values of coupling, the dependence of the separation to the asymmetry tends to disappear and the distribution becomes more uniform. This tells us that for these specific models of large mass and low coupling, the asymmetry of the energy of the two photons is less important and the distribution of the energy of the photons is then condensed in the symmetric region.

In order to confirm what we have observed with the distributions in 4.9, one can come back to the distributions with the energy of the two photons, apply an arbitrary cut on the separation of the two photons and see how the distribution changes.

We can once again observe that for a fixed separation cut of the order of $200\mu\text{m}$ the distributions change much more for the low mass and large coupling benchmark than for the large mass and low coupling benchmark.

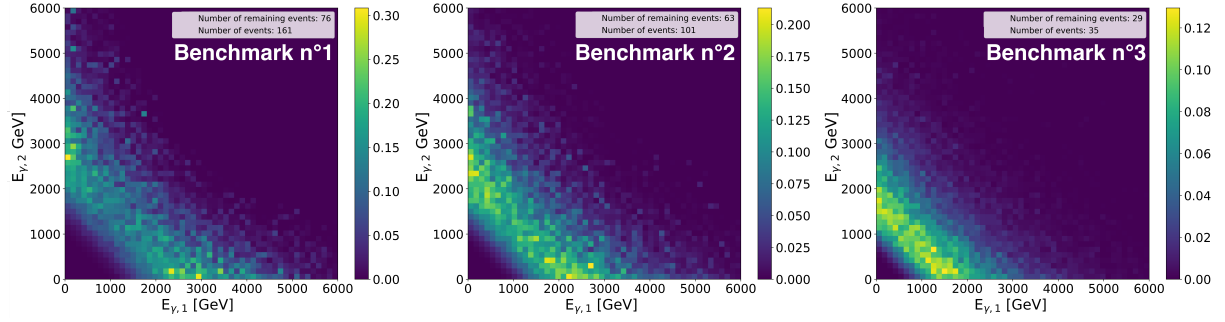


Figure 4.11: Energy distribution of the two photons with separation selection for the 3 benchmark

Another important aspect here is the diminution of the number of events when applying a certain cut on the separation. This is a critical point here since it shows that having a rather large spatial resolution for an hypothetically added module in the current FASER detector to detect di-photon signals will result in much lower number of events.

The final analysis one can do is to determine the sensitivity reach in the mass and coupling plane for the ALP for the FASER detector requesting for a minimum of 3 events with no background (which is here assumed to be zero since the MC simulations do not include any background studies) and assuming a perfect spatial resolution for the detector.

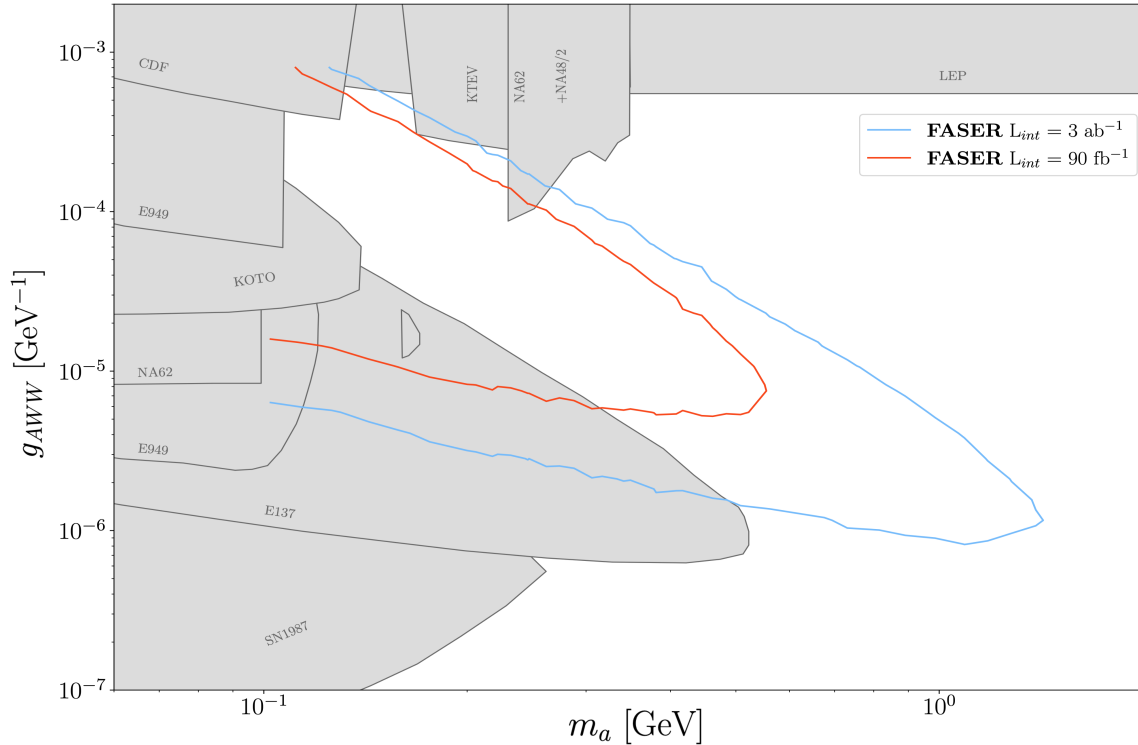


Figure 4.12: Sensitivity reach plot for FASER assuming ideal detector

The figure 4.12 presents the sensitivity reach plot for the FASER detector with an ideal detector for measuring the spatial separation between the two photons. Two different sensitivity reach are here presented, one for the LHC with data taking during a part of the Run 3 accounting

for an integrated luminosity of $\mathcal{L} = 90 \text{ fb}^{-1}$ but also for the High-Luminosity LHC (HL-LHC) which should provide a total integrated luminosity of $\mathcal{L} = 3 \text{ ab}^{-1} = 3000 \text{ fb}^{-1}$.

This final plot ends the discussion on the analysis of the MC simulations for ALP decaying inside FASER. We understood the topology of the di-photon events through the analysis of the asymmetry of their energy, the energy range in which the photons were but also through the study of the spatial distribution of decay position of the ALP in the transverse plane. We also computed the number of events expected for all of the 1452 ALP benchmark and have produced, assuming an ideal detector with perfect spatial resolution, the reach of the FASER detector for different integrated luminosities. It is now time for us to move towards the proposed upgrade of the FASER detector introducing a Pre-Shower module in order to resolve the two photons from ALP decays.

4.4.1 Sensitivity reach of FASER's PS detector

As we mentioned above, one of the aim of the simulations was to determine the performance i.e. the efficiency of the detector for resolving photon pairs with different energies and different separations out of the two list presented. An efficiency table was then produced with all of the possible combinations above so a total of 320 different configurations and the efficiencies were associated to them.

We also have previously presented the sensitivity reach plot for FASER for different integrated luminosity and assuming an ideal detector having a 100% efficiency at resolving photons whatever their energy or separation. Although, in reality this is not the case and this can affect the sensitivity reach.

The aim will then be to understand by how much the contour lines will change and to achieve this, now that the efficiencies have been computed for specific values of energies and separation for the pair of photons, we need to format the data produced in the second part of the MC simulations in order to match the above described format.

For better visualization of the procedure, we show in the figure 4.13 for one arbitrary benchmark, how the energy distributions for the two photons changes when only using the energy ranges and separations ranges also used in the GEANT4 simulations.

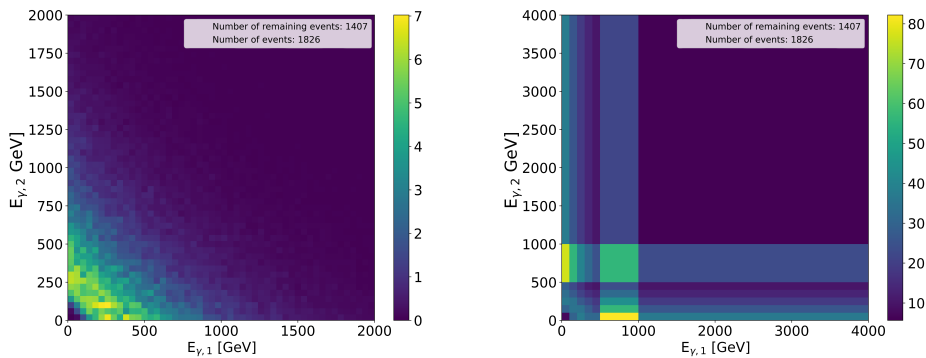


Figure 4.13: Reshaping of the photon's energy distributions

The results shown in is for a specific separation between the two photons, in order to visualize how the data would be fully represented for one benchmark for the ALP model, it would be the equivalent of having such distributions for different separations between the photons hence giving for a pair of photons of specific energies and separations, a number of events.

Now that the efficiencies of the simulated PS and the number of events simulated of the ALP decay into two photons have exactly the same shape, one can simply take the convolution between the two datasets in order to have for an ALP with mass m_a and coupling g_{aWW} what is the number of events one can expect.

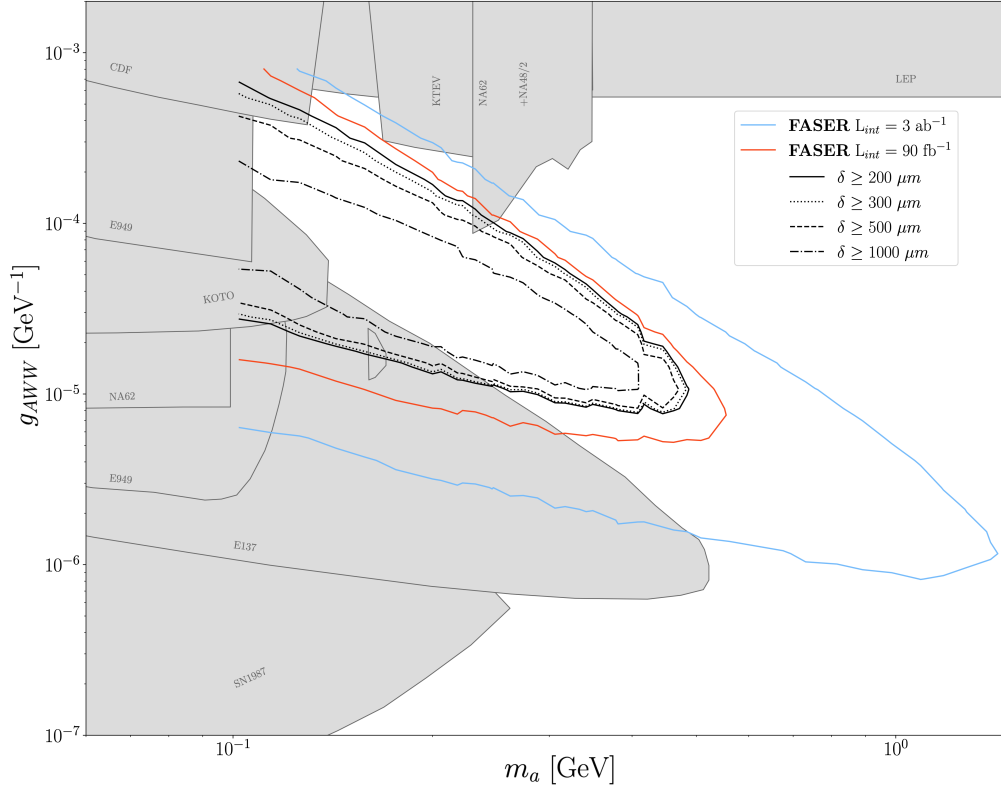


Figure 4.14: Sensitivity reach plot for different photon separation

We have presented in 4.14 the final version of the sensitivity reach plot, in which we kept the contour lines for ideal detector but also shown for an integrated luminosity of $\mathcal{L} = 90\text{fb}^{-1}$ how these contour lines would change according to the separation between the two photons. The effect of the condition on the separation obviously leads to fewer number of events detected and hence less covered area in the parameter space for the mass and the coupling of the ALP.

These results once again motivate the design of the PS detector and also shows how good the performances are without having a really sophisticated reconstruction algorithm which can certainly be improved in the future.

One could notice that when we discussed the PS design, we mentioned a really specific technology for the measurement of the charge: SiGe BiCMOS monolithic pixel detectors. The lack of explanations and details were intentional since this topic will be discussed in the next chapter.

Chapter 5

Time resolution of SiGe BiCMOS pixel detectors

The need of having particle detectors exhibiting a good spatial resolution was one of the main requirement in the past year especially in High Energy Physics (HEP) experiments. The better the spatial resolution would be and the more precise the measurement one could perform would be. Although, this was without taking into account the increasing number of collisions due to increasing luminosity in colliders like the LHC which resulted in having what is called pile-up. This phenomenon occurs when many particle tracks overlay one with another and makes the identification of each particle track almost impossible. One of the solutions to this problem is to have a better time resolution for the detectors used which would allow for distinguishing the different particle tracks.

A good timing performance is not only useful in HEP but can also find its applications in the everyday life by allowing for better precision for Positron Emission Tomography (PET) scans which would allow for better identification of cancerous cells for example.

In the following discussion, we will go through the measurement of the time resolution of a prototype designed for the ATTRACT project which is based on the same technology as the ones used for the prototype for the FASER experiment, a SiGe BiCMOS pixel detector used for timing at very low power consumption.

5.1 Fundamentals of silicon pixel detectors

5.1.1 Doped semiconductors and junctions

The Silicon being a semi-conductor, it is possible to dope it either positively (p-doped) or negatively (n-doped) in order to change its band structure and make it exhibit interesting properties. If one was to bring a p-doped and n-doped semiconductors in contact making what is called a p-n junction, the energy band structure of such an object would be illustrated in a simplified way by the figure 5.1. On the p-doped side, holes are the main charge carriers and the Fermi level is near the valence band edge, vice-versa for the n-doped side.

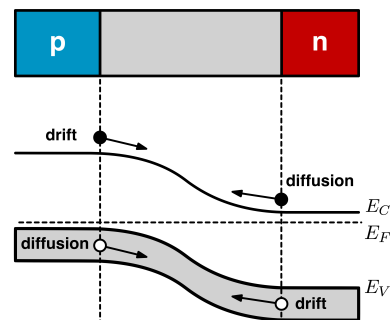


Figure 5.1: Band structure of doped silicon junction

At the boundary of the two differently doped materials a diffusion current is created due to the concentration gradient of the charge carriers, making the electrons of the n-doped region move towards the p-doped side and holes of the p-doped region moving towards the n-doped side [26]. The region in which the charge carriers can recombine is called the depletion region, it has no free charges but the atomic cores remain ionised after the recombination was done, it exhibits what is called a space-charge.

The p-doped region has a negative space-charge density while the n-doped region has a positive space-charge density. This asymmetry will generate an intrinsic electric field causing a drift current going in the opposite direction with respect to the diffusion current. The drift current continuously increases after the contact between the two regions until reaching what is called the thermal equilibrium meaning that the intensity of the two currents are the same and no more charge is moving.

One can also apply a bias voltage to the two sides of the p-n junction. If one applies a forward bias voltage ($V_{bias} > 0$) then the electrostatic potential in the depletion region reduces and the drift current reduces with respect to the diffusion current resulting in a smaller depletion region. On the other hand if one applies a reverse bias voltage ($V < 0$), the electrostatic potential in the depletion region increases relatively to its value in the thermal equilibrium and therefore the depletion region size increases to reach the thermal equilibrium.

The p-n junction with reverse bias can be seen as a particle detector. Indeed this makes the depletion region as large as possible, depending on the voltage applied of course, and when a charged particle crosses this region, it will ionize the medium, generating free charge carriers (an electron-hole pair) in the depletion region which will then be drifted towards their respective electrodes.

5.1.2 Silicium pixel detectors

The easiest way to visualize a silicium pixel detector using the depletion region of a reverse biased p-n junction is given by the following figure:

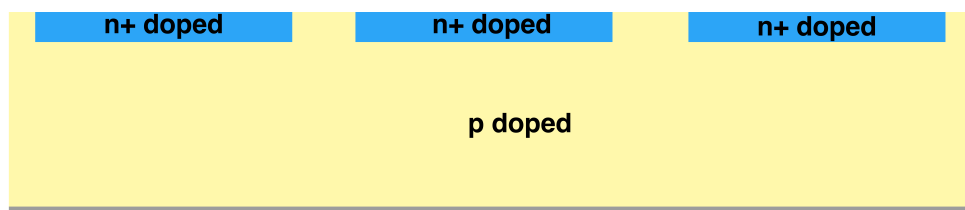


Figure 5.2: Typical schema of a pixel detector

The area of the pixel is defined by the size of the n-doped region on top of the schema and the substrate is p-doped, a reverse bias voltage is then applied between the two sides of the pixels and a depletion regions appears between the two regions. When a particle crosses the depletion region, charge carriers pairs will be created as a result of the energy loss of the particle and the energy cost to create a pair is typically in silicium of $E = 3.6eV$. The charge carriers will then be collected on each side of the pixel and the generated current is given by the Shockley-Ramo theorem such that:

$$I_{ind} = \sum_i q_i \cdot \vec{v}_{d,i} \cdot \vec{E}_{w,i} \quad (5.1)$$

We labeled in the equation 5.1 as q_i the charge of each carrier, $\vec{v}_{d,i}$ the drift velocity of each carrier and $\vec{E}_{w,i}(t)$ the so-called weighting field, used to describe how the charge carriers will move with respect to their charge and velocity in the medium. The weighting field also depends on the shape of the pixels, in fact if the pixels have a large size with respect to the inter-pixel region size, the weighting field lines will be more vertical and hence the charge collection on the electrodes will be more homogeneous and faster.

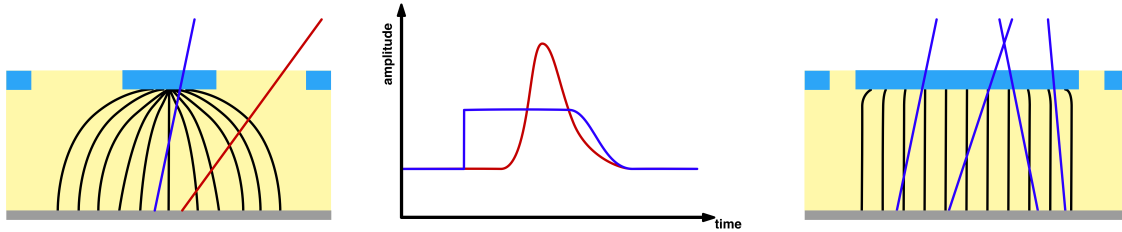


Figure 5.3: Pixel size comparison for weighting field and signal output

The figure 5.3 shows the difference in terms of the weighting field lines which are more bent in the case of a small pixel size with respect to inter-pixel region size but also shows the effect, of having a small pixel size, in the signal generated .

An interesting aspect from the charge collection is what is called the charge collection noise which is related to the non uniformity of the charge deposition in the sensor while a particle crosses the depletion region. In fact when large clusters are absorbed at the electrodes, their contribution is removed from the induced current which will then create fluctuations in the rise or fall of the signal. Since this noise is coming from statistical origin due to the process of charge deposition, the variability of the induced current is irreducible for the p-n junction based sensors [27].

5.1.3 Electronic noise

The discussion was more oriented towards the geometry of the pixels and the technology behind the working principle of them. We will now discuss the electronics and more precisely the noise coming from it.

Amplitude noise

The first category of noise we will discuss here is the noise on the amplitude of the signal which can be itself separated into two separate types of noise, the white noise and the Flicker noise. The white noise can come from thermal fluctuation, since these can alter the energy band structure of silicon, some charge carriers could suddenly have enough energy to go from one side of the depletion region to the other side generating a fluctuation in the induced current. Another source of white noise is called the Shot noise which is the noise associated to the unavoidable fluctuations in the induced current of the charges passing through a potential gap like the one generated by the depletion region. More precisely, the times needed for the charge carriers to pass through the potential gap is discrete and the fluctuation in this time generates the fluctuation in the current [26].

For what concerns the Flicker noise, the source of it is still not well explained but an interesting characteristic of it is its dependence on the frequency which also motivates its other name, the $1/f$ noise. This frequency dependence is in contrast with the white noise which does not exhibit a frequency dependence. The consequence of these two behaviors is that for the lower

frequencies, the noise will be dominated by the Flicker noise and for the highest frequencies, dominated by the white noise.

The last concept we will introduce here is what is called the Equivalent Noise Charge (ENC), which represents the charge to which the noise, after amplification, corresponds to. The expression for the ENC is then given by:

$$ENC = \frac{\sigma_V}{\text{Gain}} \quad (5.2)$$

One has to pay attention to the fact that the ENC is associated to the electronics and when measuring, for example with an oscilloscope the noise, one has to take into account that the noise of the electronics themselves and the noise of the oscilloscope, quadratically combines. The ENC can then be rewritten as:

$$ENC = \frac{\sqrt{\sigma_{measured}^2 - \sigma_{Scope}^2}}{\text{Gain}} \quad (5.3)$$

Timing noise

The second category of noise we will discuss now is the timing noise which can be separated into the time jitter noise and the time walk noise.

The time jitter is directly linked to the amplitude noise, since if one fixes the threshold on an oscilloscope to a constant value, due to the amplitude fluctuation, the signal might pass above the threshold, then go under it again and finally pass above it a second time, resulting in an anticipation in the time at which the threshold level should have been crossed. The expression for the time jitter is given by the following expression:

$$\sigma_{t,jitter} = \frac{\text{Rise Time}}{\text{Signal to Noise ratio}} = \frac{\text{Rise Time} \cdot ENC}{Amp} \quad (5.4)$$

Since this noise is directly linked to the random noise coming from the amplitude it is not possible to correct for it except by either having a better rise time (which means a smaller values for it), or by having a better amplification and so a better gain to have a greater amplitude.

On the other hand, if one takes two signals with different amplitude but same rise time, the time at which the signal will cross the threshold is different since the slope of the signal, i.e. how fast it rises, will be different. In contrast with the time jitter noise, this one can be corrected and this will be the focus of the following discussion. The aim will be to reduce as much as possible the value for the time resolution making its dominant contribution coming from the time jitter. The final aim of the correction will be to find an easy but effective correction method that could further be implemented in the electronics themselves in order to have the best possible time resolution without having to perform additional corrections after data taking.

5.2 Measuring the time resolution

After motivating how important timing is in HEP experiments, it is interesting to understand how one can actually measure the time resolution of a specific sensor. In the following part we will present the procedure used to measure the time resolution of our object of interest by measuring the Time Of Flight (TOF) between our object and a reference sensor. We will first go through a quick presentation of the ATTRACT sensor, then move towards another quick presentation of the object of reference, a Low Gain Avalanche Diode (LGAD) and we'll describe the set-up used. We will also briefly explain how data was taken and reshaped in order to pursue with analysis.

5.2.1 The ATTRACT prototype

The object we want to test here is not the prototype which was designed for FASER but is another SiGe BiCMOS pixel detector developed for the ATTRACT project and we will refer to it in what follows as the ATTRACT prototype or the ATTRACT sensor. The technology on which the design relies is although the same for the two prototypes.

The ATTRACT prototype has been realized in the SG13G2 130 nm BiCMOS technology of IHP for which the electronics are placed in triple wells inside the guard rings. The pixel are hexagonally shaped in order to increase the angles at the corner of the pixels to reduce the electric field at the nearby surface and limit the risk of early breakdown in these regions due to the P-stop layer in the low-resistivity substrate [28] .

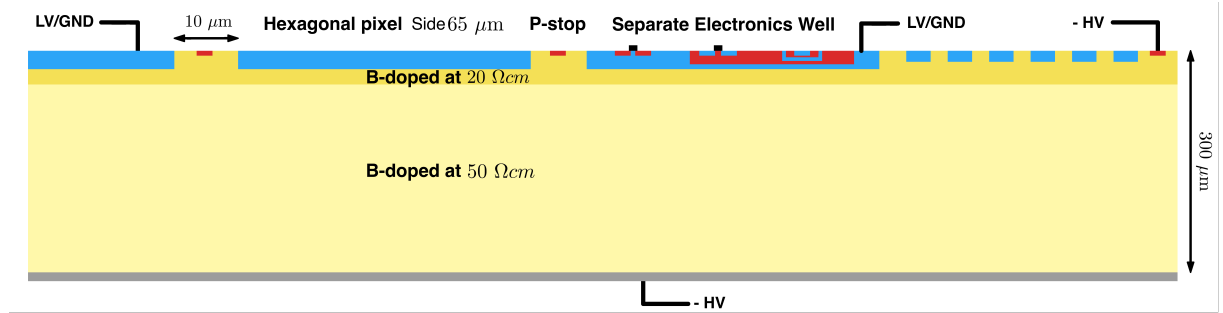


Figure 5.4: Cross section of the detector

On the figure 5.4, one can see the p-doped regions illustrated in red for the p-stop and in yellow for the p-doped substrate, while the n-doped regions are in blue. The p-doped substrate, in the technology of standard resistivity 50 Ω-cm, is connected from the top surface outside the guard rings but also from the backside, to the negative High Voltage (HV). On the other hand, the pixels themselves and the triple wells containing the electronics are connected to the positive Low Voltage (LV). The values for the HV were ranging from 80V up to 160V and even 180V for some of the the prototypes but a drift in current was observed and this working condition was no longer used to prevent damages. For a typical HV of 140V corresponds a depletion region of 26 μm depth which implies for the typical signal of a Minimum Ionizing Particle (MIP) a charge deposited of approximately 1600 electrons (accounting for 3,6 eV for energy loss per electron-hole pair resulting in approximately 60 pairs created per micron). For what concerns the low voltage is was operated between 1.8V and 2.0V.

In order to control the different element of the front-end electronics integrated in the chip to vary the power consumption of it but also its performances and stability, a Digital to Analog Converter (DAC) is used. More precisely, a Pad current I_{Pad} is sent to the chip, further divided by 50 in order to obtain what is the main bias current $I_{bias} = I_{Pad}/50 = 1\mu A$. This later will be used to set the bias current of many elements but the ones of interest here are the pre-amplifier (pre-amp), feedback and driver bias currents. All of these three bias current will be expressed as the main bias currents times one of the DAC values ranging from 0 to 255 such that we can write each of them as:

$$I_{pre-amp} = I_{bias} \cdot DAC \quad ; \quad I_{feedback} = \frac{I_{bias} \cdot DAC}{16} \quad ; \quad I_{driver} = \frac{I_{bias} \cdot DAC}{2} \quad (5.5)$$

The DAC values are set using a configuration software specifically developed for the UniGe GPIO (General Purpose Input Output) board, connected to the board on which the ATTRACT prototype is glued. The figure 5.5 shows a picture of the ATTRACT prototype mounted onboard.

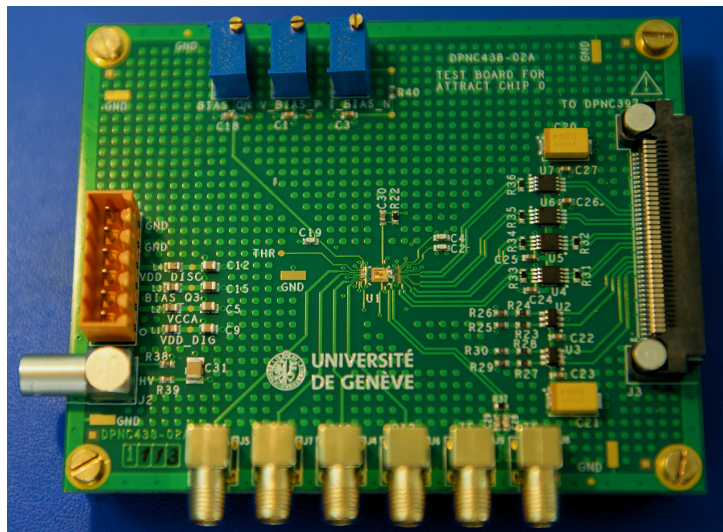


Figure 5.5: ATTRACT prototype mounted on board

The chip itself can be separated into 4 different parts corresponding to 4 different types of pixel architecture and version of the electronics. For our purpose, since we want to have access to the waveforms themselves and read them with an oscilloscope directly, we will only use three of the four pixels with the analog outputs (also because on this chip the Time to Digital Converter (TDC) didn't work so there is no other option than using these outputs). A closer picture of the chip is given in the figure 5.6 with each of the groups of pixels identified and the four pixels of interest for us highlighted as well.

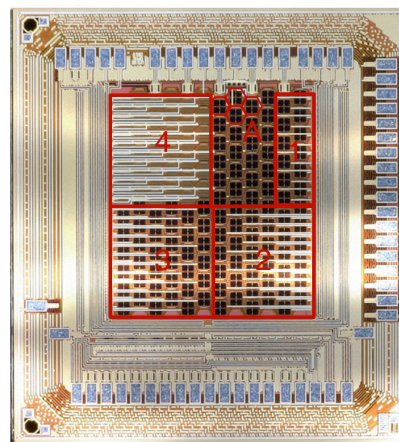


Figure 5.6: A closer look to the ATTRACT prototype chip

5.2.2 Reference sensor: LGAD

The Avalanche PhotoDiodes (APDs) developed for detecting low energy particles and x-rays exhibit an internal signal gain, proportional to the bias voltage applied and with good uniformity across large detection areas. If operated in the linear region, the output signal is proportional to the energy deposited with a gain which can range between 10 to 100, allowing for detection of only few photons and very low energy particles [29]. A counter part of this gain performance is that the noise associated to the multiplication process can affect the signal-to-noise ratio.

Considering an APD with modified doping levels creates devices with lower gain in the range of 5 to 10, operated in the linear region for proportional response with a low voltage applied requiring a high resistivity silicon substrate in order to achieve full depletion, such a sensor is called an LGAD. The lower gain induces less noise and the gain dependence on temperature and applied bias voltage is comparable with the one of standard APDs.

This design enables for the detection of sub-ns signals produced by MIPs for which the ionisation is uniformly produced as a function of depth of the detector. For an LGAD with supposed

gain of 10, if the substrate depth is thinner than regular PIN silicon detectors, by an order of magnitude, the same signal will be produced from a MIP for the 2 devices [29]. The LGAD structure enables for fast rise time and hence fast silicon timing detectors.

The concept of the LGAD is based on a standard PIN detector with a basic doping structure of $n^+ / p / p^- / p^+$ structure. An interesting way to better understand this structure is through a cross section of the pad as follows:

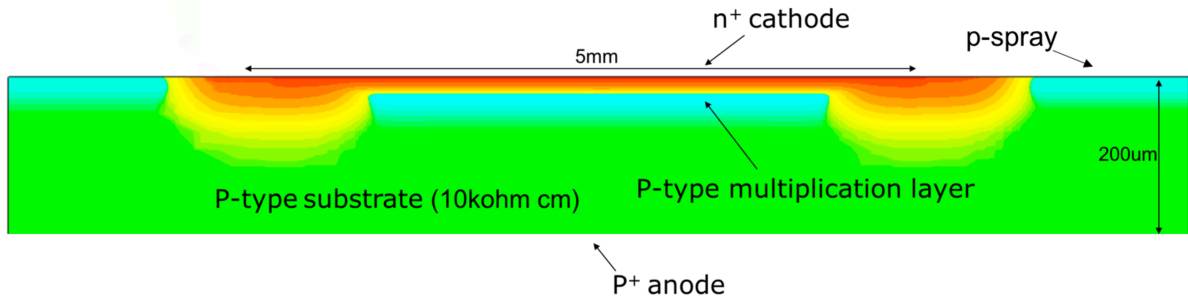


Figure 5.7: Cross section of an LGADs pad exhibiting its doping structure

We can observe for the figure 5.7 a highly n^+ doped cathode electrode with a moderately doped p-type region known as the multiplication implant. The n-type electrode has a peak doping concentration of about $1 \cdot 10^{19} \text{ cm}^{-3}$ and a thin profile into the silicon bulk of the order of $1 \mu\text{m}$. On the other hand, the p-type multiplication implant has a lower peak doping concentration of the order of $1 \cdot 10^{19} \text{ cm}^{-3}$ but has a much deeper profile into the silicon bulk of the order of $4 \mu\text{m}$. For what regards the silicon bulk itself it has a high resistivity of the order of $10\text{k}\Omega - \text{cm}$ with a p^+ anode electrode on the backside.

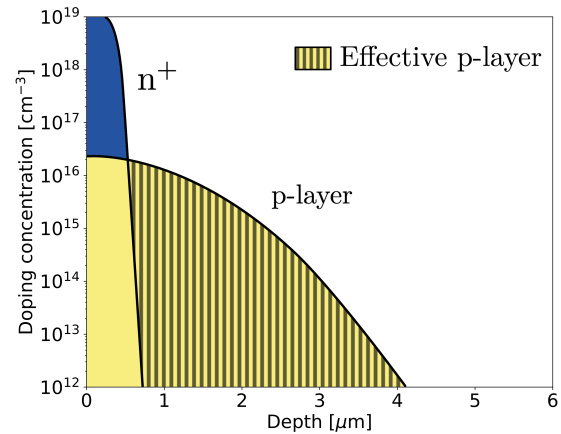


Figure 5.8: Doping concentration profile

An example of the doping concentration through the n-type cathode and the p-type multiplication implant is shown in the figure 5.8 .

Since the bulk is a p-type high resistivity, a $4 \mu\text{m}$ and uniform p-spray doping with peak concentration of the order of $1 \cdot 10^{15} \text{ cm}^{-3}$ is added in order to isolate the cathodes. An additional deep n^+ doping region is added at the sides of each cathode to reduce the magnitude of the electric field. If not added, the electric field at the edge of the n^+ cathode will be larger than the one in the multiplication region resulting in breakdown taking place at this location [29].

The sensor is operated with the silicon bulk being over depleted such that when incident radiation produces electron-hole pairs in the detector, they drift towards their respective electrodes. The electric field gets its maximal magnitude between the n^+ cathode and the p-type multiplication electrode.

The sensor used for the timing measurement is an improved version of the model described above, it has a total thickness of approximately $50 \mu\text{m}$ to reduce the charge collection noise and

was first produced at Fondazione Bruno Kessler (FBK) in 2017 [30]. The main idea was also to improve the radiation tolerance with respect to the radiation tolerance of the 300 μm substrate production at FBK in 2016. Different design were produced depending on the gain layer configuration and the LGAD we used for the measurement was the one having an approximate 45 ps time resolution for the conditions in which it was operated.

A dedicated board was designed here at the University of Geneva in order to operate the LGADs and to recover the analog waveforms for analysis. A picture of one of the LGADs glued to the board is shown in the figure 5.9:

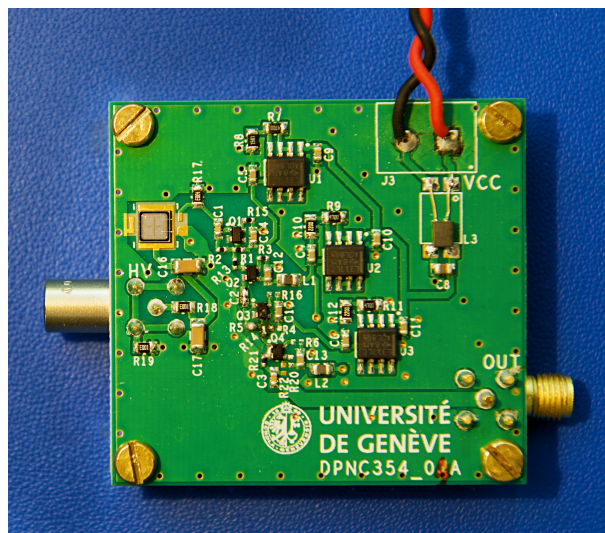


Figure 5.9: Picture of the LGAD mounted onboard

One could note the hole drilled at the back of the board, this is to avoid further losses of events unfortunately not surviving through the material of the board, It can seem to be marginal gain but for low energy particles it matters.

5.2.3 Layout of experiment

As we said before, the aim of the measurement which will be performed is to measure the time resolution of the ATTRACT prototype using as a reference a 45 ps LGAD through a TOF measurement between the two sensors. We here anticipate a bit the next section in which we will present the analysis performed to correct for the time walk of the ATTRACT prototype but in order to obtain a set of variables such as amplitude of the signal, Time Of Arrival (TOA), Time Over Threshold (TOT) and many others, since the TDC of the ATTRACT prototype was not working, we will use the analog channels. It is in fact even better to use these channels since they provide as an output the full analog waveform which allows for better understanding of the sensor's behavior. For what concerns the LGAD, the analog output will also be used in order to obtain the same variables described above and to have a look at the waveforms too.

Board assembly

The very first task one has to accomplish in order to start setting up the experiment for the data taking is to prepare the two boards with the two sensors, for the TOF measurement. An important aspect to understand is that the closer the two sensors will be to each other, the higher the rates of the events one will have access to. This is due to the fact that the source used (^{90}Sr) emits electrons in one direction but as soon as these exits the container of the source, they are emitted in all directions. We can characterize the spread by the solid angle containing all of the

electrons and so the further the sensors from the source, but also the further the sensors are from one to another and the smaller the portion of solid angle covered.

Another aspect one has to take into account is the thickness of the boards on which the two pixel detectors are glued, in fact due to the spectrum in energy of the source used, the electrons with the lowest energy might not survive through the ~ 1.5 mm and hence having a drilled hole just behind the sensor on the board is necessary.

In the set-up we used, we only had the LGAD board with a hole and so it was placed on top of the ATTRACT board (on which the ATTRACT sensor is glued) as close as possible. A support was 3D-printed in order to be placed on top of the ATTRACT board (being the largest of the two) and also acting as support for the LGAD. It allowed for good alignment between the two sensors but also as a support for the source container to align it with the two sensors and place it as close as possible.

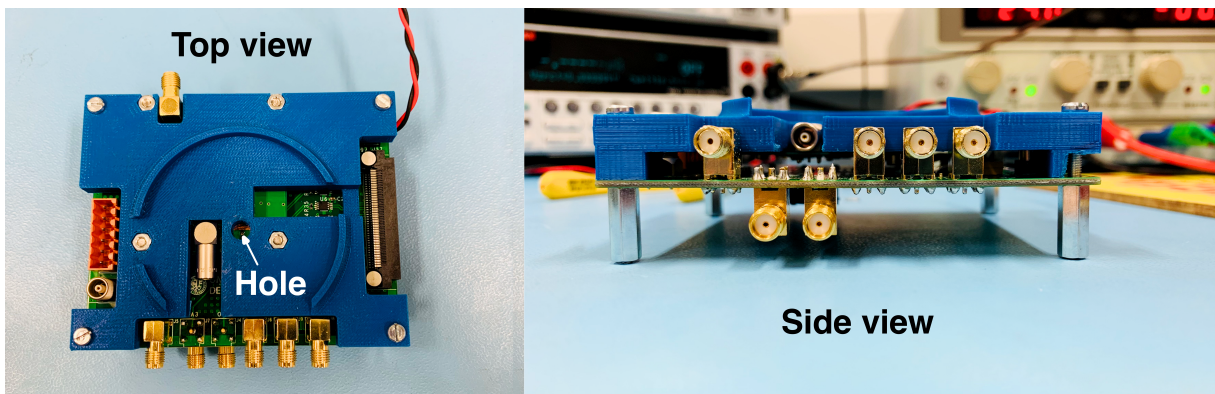


Figure 5.10: LGAD mounted on top of the ATTRACT board with the 3D-printed support

The figure 5.10 presents the separation between the two board obtained using the 3D-printer support, it also shows a top view exhibiting the place on which the source is positioned and held by the same support.

Power routing and outputs

The next step in the preparation of the set-up is to provide the two boards and sensors with power. The ATTRACT board has two input, one for the HV using a LEMO connector and a 6 pin terminal block connector for the LV. It also has a digital input for the connection with the UniGe GPIO. For what concerns the LGAD board it has one input for the HV using again a LEMO connector and simply two cables connected to the side of the board for the LV.

Regarding the outputs for each of the boards, the ATTRACT one has four analog output for the four pixels mentioned above and the LGAD board only has one.

The Power Supplies (PSU) used for the HV of both the boards are Keithley 2400 SourceMeter. A converter to LEMO input will be used on the two positive and negative outputs of the PSUs in order to directly connect the boards using two LEMO cables. For the LV, a single Aim-TTi PSU with double output channels was used to power the two boards, for the ATTRACT one using the 6 pin terminal block connector on one side and six banana pins, for the LGAD using simply 2 banana pins, the cables were directly welded on the board itself.

Now concerning the analog output of both boards to recover the waveforms, we used a Lecroy Teledyne oscilloscope with bandwidth ranging from 3GHz up to 40 GHz and a sampling rate of

80 Giga Samples (GS) per seconds. The cables used to connect the analog output directly to the oscilloscope were SMA cables and DMC to SMA adapters were plugged on the oscilloscope side for the connection. When using these SMA cables for this purpose, one has to pay attention to the length of them since it can induce a time delay on the signals.

The oscilloscope used only has four analog inputs channels and having four analog channels on the ATTRACT board and one on the LGAD board, it was not possible to connect all of them. This is not an issue since what we want to study is the coincidence between two of the pixels. We could hence only connect one of the pixels from the ATTRACT sensor and the routed pixel of the LGAD. Although, since we still have two unused channels, we can connect two others pixels from the four on the ATTRACT sensor in order to have a study of cross-talks, which can happen when an induced signal in one of the pixels give rise to a parasitic signal in the neighbouring pixels, having a non desired effect on the time resolution.

Hence we used three cables of identical length for three of the four outputs of the ATTRACT Board and a longer cable for the LGAD board analog output in order to have a significant TOF between the two sensors.

Finally, the two boards were placed inside an insulating box for radiations made of a thick layer of plexiglas surrounded by a layer of lead. The box can be opened from the top allowing for access and a gap is left on the side in order to let the cables in and out of the box. A PC was also used for controlling the UniGe GPIO and program the chip i.e. set the different DAC values for the different bias currents.

The experimental set-up is now complete and we can now focus and how the data was taken with the the oscilloscope but also how it was transformed in order to be suitable for corrections, selection and further analysis.

5.2.4 Data taking scheme

Setting up the data taking

The measurement we want to perform here is a time resolution measurement through a TOF measurement between our object and a reference sensor. Concretely, we are looking for coincidences in a short window of time (mainly set by the difference in SMA cable length) or the order of 15 ns here. Additionally, we want to be outside of the noisy region around the baseline of the signal to not trigger on what we call fake coincidence events which will for sure worsen the time resolution.

The oscilloscope was connected to four different channels we will order as follows: **Channel 1**: the pixel used for coincidences from the ATTRACT sensor, **Channel 2 & 3**: neighbouring pixels of the studied one as well on the ATTRACT sensor, **Channel 4**: the pixel used for coincidences from the LGAD sensor.

To set the trigger for coincidences on the oscilloscope, we need to choose a qualified multistage-type trigger which allows for trigger only when two of the channels passed the chosen triggers. We also need to add for both channel that they are DC coupled and that for both channels the trigger region is set for positive slopes of the signals meaning the rising edge of the signal.

For what concerns the trigger levels, this is where one has to pay attention to the noise around the baseline of the signal. In order to guess the trigger level, there are two options, the first one consists in slowly increasing the threshold without any radioactive source generating coincidences and find for what value of threshold, after waiting a certain time, there are no more triggers. The second and more accurate option is to perform a quick and simple noise analysis by computing the mean but also the standard deviation of the noise. This is completely suited since in fact

the noise is randomly generated at any time and so describes perfectly a Gaussian distribution. Once the values for average and standard deviation have converged to (almost) fixed values, one can set the threshold at the following level:

$$Thr = \mu_{noise} + 5 \cdot \sigma_{noise} \quad (5.6)$$

This allows for having a probability of $2.86 \cdot 10^{-7}$ % of triggering on the noisy part of the signal. One could then ask why we don't event put the threshold to higher values but this as a significant impact on the performance of the sensor. Indeed if selecting only the events for which the amplitude is the highest will give a better performance for the sensor but will not be representative of the "true" performance of the sensor. Also, the efficiency in terms of amplitude of the signals for which the pixel is sensitive will highly decrease. The criteria given above is then the best compromise between maintaining a good efficiency, and having truthful measurement of the performances in terms of time resolution.

An important note for what was said above is that even if five times the standard deviation gives an high confidence level, noise is not something constant over time and can be affected by many sources through time. The five standard deviation gives a good estimation of the level but one should always double check that the noisy event rate is still low enough. For some of the measurement performed we even had to go up to six or seven standard deviations as a matter of fact.

We have now set up all of what regards the event selection with the multistage trigger and we will now quickly also discuss how the data was saved from the oscilloscope to optimize the time of data taking. Instead of saving each and every single waveform as soon as the trigger fired, we used what are called sequences. A sequence is made of a set of segments and each of the segments represents one of the waveforms saved. This way we can acquire for example 200 segments in a sequence and then only save the sequence which allows for not always reading the full memory of the oscilloscope while almost empty but reading it when almost full which saves some time.

Data conversion

After the data has been saved for a full measurement on the oscilloscope, it is downloaded and then converted into what we will here call a root file, referring to the ROOT programming software developed at CERN [31].

The conversion software concretely does a waveform analysis by defining a set of standard variables like rise-time, TOA, TOT, amplitude, time for a certain percentage of the amplitude, noise level and standard deviation, and many others (not relevant for us in what follows). The analysis is performed on every waveform and the results are then stored and a ROOT tree which helps visualizing in a simple way the data set. It also allows for quickly and easily building distributions for whatever variables which gives a very instructive insight into the data set.

When converting the waveform into these variables, one can also choose to save all of the waveforms. It can be useful for example if a category of events have a different behavior than the rest of the set, then it may be possible to find similarities between the waveforms and further understand the sensor and electronics behavior.

In order to perform the analysis, the code also requires the user to put information with respect to the region in which the signal is located (for defining the variables linked to the signal itself) and a noisy region (used for defining the variables linked to the noise). The user will also be asked to give the value of the threshold used and generally has to take a slightly bigger value than the one set on the scope since this previous is not really accurate.

Measurement parameters

The performances of the sensor are different with respect to many parameters but the one we will here test are the performances with respect to the power consumption of the front end electronics, mainly determined by the current provided to the pre-amp, but also with respect to the HV provided for the depletion of the sensor. The different measurement were then organized by first defining what we will call Working Points (WP) which corresponds to the different DAC values given for the driver, feedback and pre-amp currents. For all of the WP, the measurement will be taken for different HVs ranging from the minimum required to start depleting, up to the maximum depletion the sensor can withstand. We present in the following table, all of the measurements performed:

WP	LV [V]	$I_{Pre-amp}$ [DAC]	$I_{Feedback}$ [DAC]	I_{Driver} [DAC]	HVs [V]
2	1.8	150	100	50	80, 100, 120, 140, 160
4	2.0	7	10	200	100, 120, 140, 160
5	2.0	20	100	200	80, 100, 120, 140, 160
6	2.0	50	75	175	80, 100, 120, 140, 160

Once all of these measurement are performed, one can proceed to the analysis of the results in order to understand how time walk can be corrected to get the time resolution performance for the ATTRACT prototype depending on the depletion and the power consumption.

Chapter 6

Results for time resolution of the ATTRACT sensor and Time walk correction

6.1 Calibration

An important step to make before starting with the actual analysis is the energy calibration of our sensor. In fact this will help use calculate the correspondance in the number of electrons for the threshold but it will also help us compute the ENC.

In other to do this calibration, we will use a simplified set-up than the one described above since we only need to have the ATTRACT board powered and only one of the analog outputs connected. The source we will use is also different (^{109}Cd) since the calibration will be performed with photons and not electrons, giving peaks in the energy distribution and not a Landau distribution like the ^{90}Sr source used for the TOF measurements. The physical process involved here is photoelectric effect meaning the photons will release all of their energy in a single point. This energy deposition is also not dependent on the depth of the depletion region unlike for the ^{90}Sr which ensures that the position of the peaks measured is accurate.

The calibration will be performed for the same HV applied to the pixel with a value of HV = 140V and it will be performed for all of the four WPs described in the table 5.2.4. We will only present the procedure and intermediate results for WP2 since it is exactly the same for the others three.

We know from the literature that the two principal energy peaks of the ^{109}Cd corresponds to the following values of energy:

$$E_{\gamma,1} = 22.16317 \text{ keV} \quad , \quad E_{\gamma,2} = 24.9427 \text{ keV} \quad (6.1)$$

The aim of the calibration will then to make a correspondance between the amplitude of the signal measured and the energy deposited in the sensor. One can also use that the energy cost to produce an electron-hole pair in silicium to also know the correspondance between amplitude and number of electrons such that:

$$Amp \text{ [V]} = \alpha E \text{ [keV]} \quad \text{and} \quad Amp \text{ [V]} = 3.6 \cdot \alpha E = \beta E \text{ [number of electrons]} \quad (6.2)$$

We have labelled in the equations 6.2 as E the energy. One could see that what we called β is nothing more than the gain of the front-end electronics in units of mV/e^- .

We present in the following figure the spectrum of amplitudes for the source of ^{109}Cd :

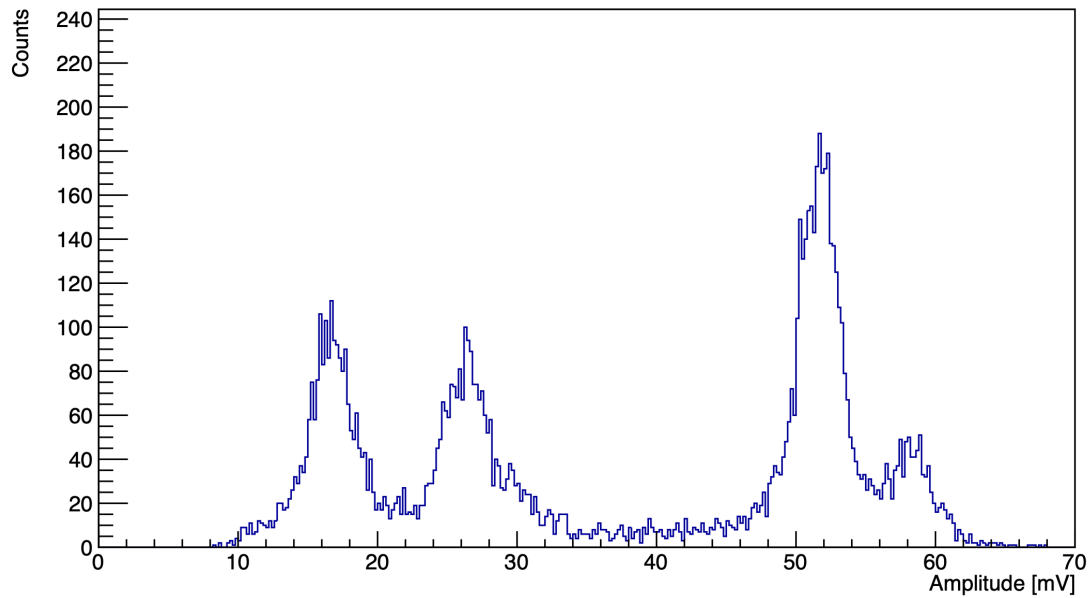


Figure 6.1: Spectrum in amplitude of the ^{109}Cd photon source

The spectrum obtained shows four distinct peaks but we will only focus on the second and third ones since we only know the energy for these ones. The way the exact amplitude for the two peaks was obtained was by simply fitting using a Gaussian distribution the peaks and the value of the peak in amplitude was then simply the value of the mean of the Gaussian distribution. The results of the fit are given by the following figure:

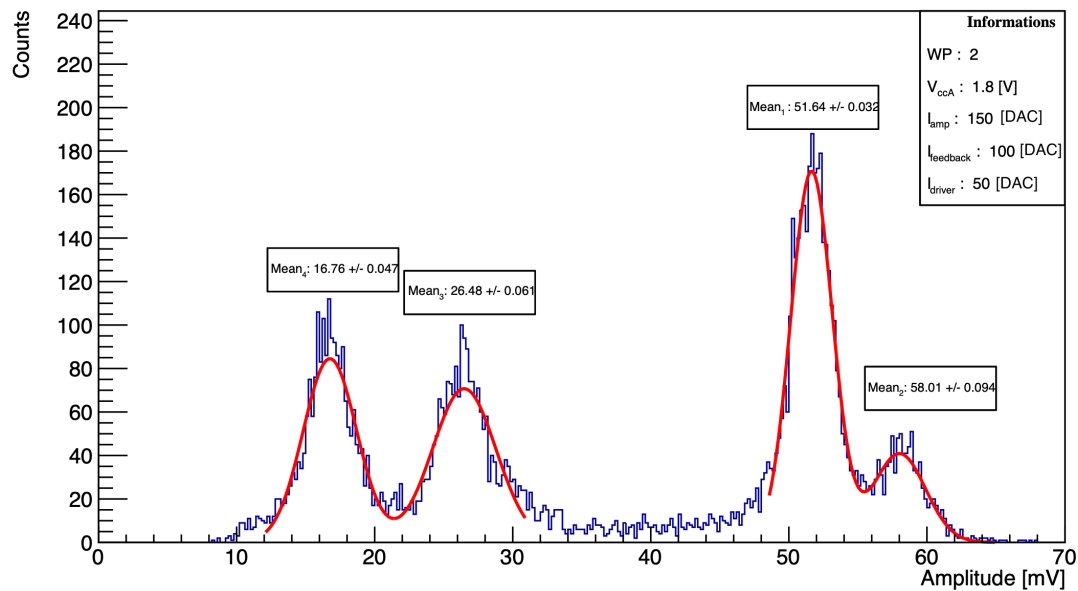


Figure 6.2: Fitted spectrum in amplitude for ^{109}Cd photon source

The next step is to plot the amplitude as a function of the energy and to fit the three points obtained (requesting that for zero amplitude the energy deposited is zero). The value of the constant α will then simply be given by the slope of the linear fit. In order to also obtain the value of the β constant, one can do the same but this time fitting with respect to the number of electrons instead of the energy. We show the results, still for WP2 in the below figure:

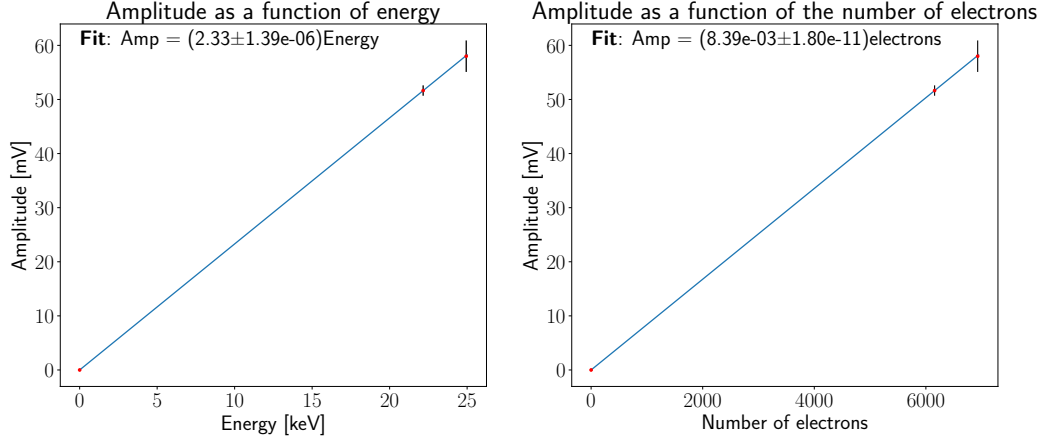


Figure 6.3: Amplitude as a function of the energy

The exact same analysis was hence performed for all of the four WPs and the results for the values of α , the gain and the ENC are presented in the following table:

WP	α [mV/keV]	Gain [mV/ e^-]	ENC [e^-]
2	2.33	$8.39 \cdot 10^{-3}$	86.88
4	1.46	$5.24 \cdot 10^{-3}$	136.73
5	1.81	$6.50 \cdot 10^{-3}$	108.36
6	2.29	$8.25 \cdot 10^{-3}$	51.50

A better way to represent these results is to plot the ENC as a function of the pre-amp current since it largely determines the power consumption of the front-end electronics:

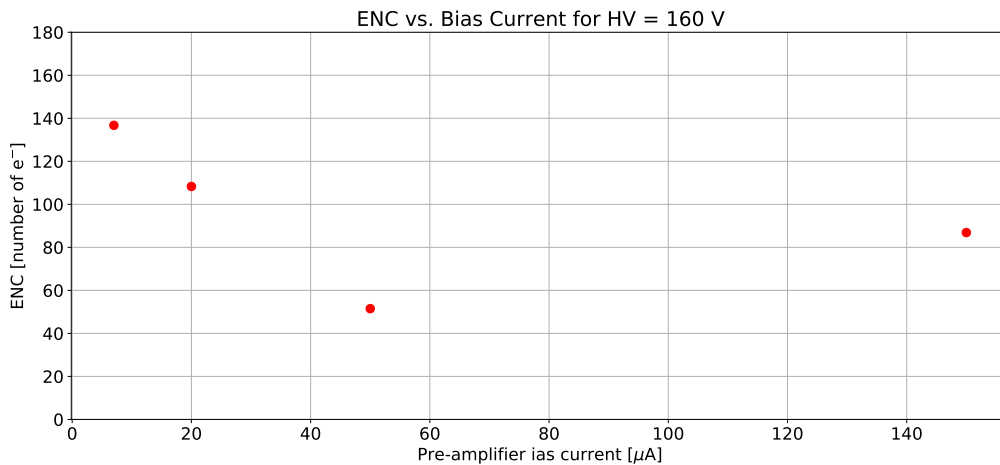


Figure 6.4: ENC as a function of the power consumption of the front end electronics

We can see on this figure that the ENC tends to decrease as the power consumption increases but for the WP6 having a pre-amp current of $50\ \mu\text{A}$, the ENC is smaller with respect to the ENC for the WP2 with pre-amp current of $150\ \mu\text{A}$. This can be explained by understanding that the product between the bandwidth of the amplifier and the gain is constant. If one has a smaller bandwidth, the effect produced is an average on the higher frequency components of the signal. This causes the noise to become lower but also the amplitude while the rise time increases. By increasing or decreasing the feedback bias current, one respectively decreases or increases the gain and so playing with this parameter can help trade bandwidth for gain. This depends whether one wants to have a less noisy and hence less amplified and fast signal or wants a more noisy but more amplified and faster signal. One has to pay attention to the fact there does not seem to be any error on the values given but these are too small to even appear on the figure.

The explanation for the point above is that one went for a less noisy signal but then had a less fast and less amplified signal by in fact trading bandwidth for gain. The important is that the timing performance still gets better with increasing power consumption.

6.2 Time walk correction

The discussion will now, as we finished describing the data taking procedure and the calibration, move towards the analysis in order to perform time walk correction on the TOF measurements to determine the time resolution of our object. Before going deep into the methods used for the correction itself, we will discuss the selection made on the events.

In what follows, there will be many references to the TOT, TOA, amplitude etc... for each of the different acquired channels. We will then, for the ease of reading, refer for example to the TOT for the pixel of the ATTRACT sensor used for timing as TOT1 and so on for the other two pixels from this sensor and for the LGAD pixel (the number are associated to the channel number we associated to each pixel earlier).

6.2.1 Event selection

There are mainly three event selections one has to perform before going on with the time walk correction, namely the correction for cross talks from the neighbouring pixels on the Attract sensor, the "stability" region for the LGAD performances and the threshold condition on the tested pixel.

Cross-talks selection

We call a cross talk between pixels when a signal in one pixel has an influence on one or more pixels. In the design of the ATTRACT sensor, this is mainly due to the fact that the output lines for the four analog pixels are really thin and close to each other. This means that when a significant signal is transported through these lines it can parasitically generate a signal in the neighbouring output lines for which the signal will have the shape of the derivative of the signal. This is due to the fact that the "bridge" between the two lines will act like a capacitor and this justifies the shape of the signal. The "fake" signal coming from cross-talks will then be delayed and will worsen the time resolution of the sensor.

From the event selection point of view, this means that any event recorded for which the amplitude (amp) of pixel n° 1 (Amp1) is smaller than amplitude of pixel n° 2 (Amp2) or pixel n° 3 (Amp3), then the event will not be selected for the further analysis.

Stability of the LGAD

The LGAD has its front-end electronics on the board and not integrated inside the pixels as for the ATTRACT sensor. The part for which we are concerned here is the double stage amplifier since one of the two saturated for values of amplitude (Amp4) of the signal of the order of Amp4 = 110 mV, above this values, the linearity in performances was lost and so we have to restrict to this upper value.

There is also a lower bound for the values of the amplitude for which the performances also worsen since this corresponds to a category of events for which the particles hit is either in the inter-pixel region or in the periphery of the sensor itself. The lower bound which was then set to Amp4= 70 mV resulted from the event selection point of view of not selecting events for which the amplitude is either smaller than 70 mV or bigger than 110 mV.

Threshold selection

The last selection criteria seems to be obvious but makes a significant difference. When discussing the conversion of the data from the oscilloscope to make it suitable for analysis, we had to provide the code with a threshold for each channel of the oscilloscope. This value for the threshold is used to find the values of the other variables like TOA or TOT. We also discussed the fact that it is always better to have a slightly higher threshold than the one used on the oscilloscope in order to be sure not to probe the noisy region as well.

From the event selection point of view this means that any event for which the value of the amplitude (Amp1) will be smaller than the threshold set on this channel, will not be taken into account for the rest of the analysis.

6.2.2 Time walk correction procedure

As we explained in the first section of this chapter, the time walk is one of the contributions to the time resolution of our sensor. The aim will there be to find what is the best method out of the three different corrections we investigated, to correct for the time walk and enhance the time resolution.

The three variables for which the time walk correction was investigated were the inverse of the amplitude of the signal ($1/\text{Amp1}$), the TOT of the signal (TOT1) and the inverse of the slope of the signal ($1/\text{Slope1}$). More precisely the slope corresponds to the difference between the amplitude of the signal at 80% and at 20% divided by the difference of the time at which the signal reaches 80% of its amplitude and when it reaches 20%.

The time walk correction we investigate here is for the ATTRACT sensor but the LGAD also needs a time walk correction which will only be performed with respect to the amplitude of the signal (Amp4).

In order to make the discussion easier to follow and more concise in what follows, we will present in the first place the procedure for the time walk correction taking as an example the correction with respect to the inverse of the amplitude. The procedure is almost the same no matter what is the sensor or the the variable with respect to which the correction is performed. Only a few parameters have to be tuned with respect to the exact correction performed. All of the configurations of the HV and the bias current will also not be presented since it would be completely irrelevant. Instead we will present in the step-by-step description only the results for one of the WP for a certain HV. The full results will be presented at the very end for the time resolution of all configurations and for all three corrections methods.

The general method

The correction for the time walk is performed on the two-dimensional distribution of the TOF, defined as the difference of the TOA the ATTRACT pixel (TOA1) and the TOA of the LGAD pixel (TOA4), as a function of one of the three listed variables. One could have noticed that for the first and third correction method, it is performed with respect to the inverse of the a standard variable. This is simply due to the fact that the distribution is easier to fit this way and hence the code performance to correct increases.

The first step of the correction is to loop over all of the recorded events and to apply the selection criteria we discussed above, if and only all of the three conditions are satisfied, the variables relatives to the events are stored in a two-dimensional histogram with the TOF on the y-axis and the inverse of the amplitude of the ATTRACT pixel on the x-axis. A typical distribution obtained after looping over all of the events is given by the following figure:

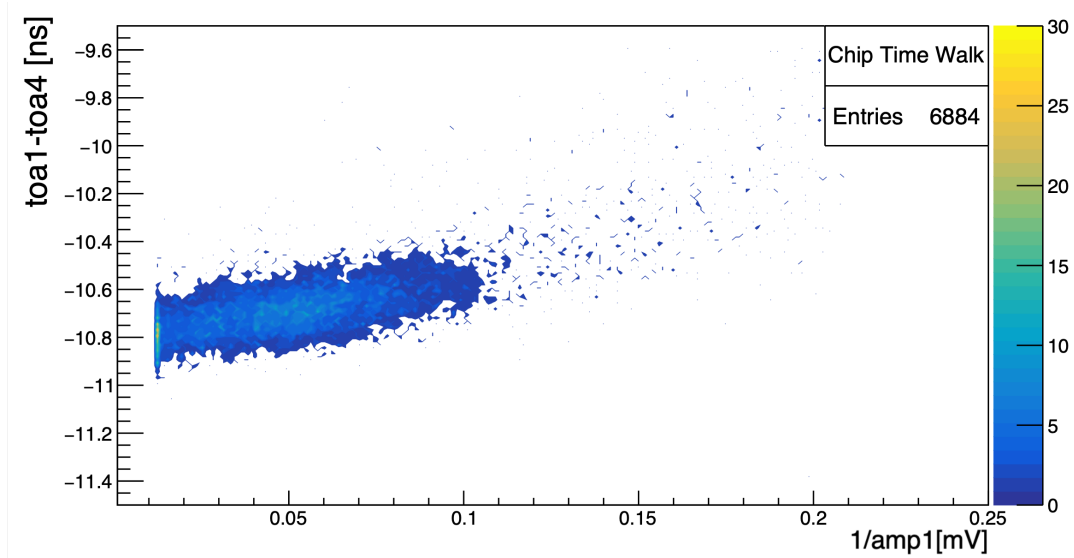


Figure 6.5: Shape of distribution without correction

As one can see, the TOF is not constant with respect to the inverse of the amplitude and tends to increase as the values of the amplitude decreases. An important point to understand is that if one was to directly put into an histogram the values of the TOF, it would be the equivalent of projecting this two-dimensional histogram along the y-axis. The distribution is then going to have a larger spread due to the amplitude dependance with respect to a distribution for which there is no dependance.

The idea of the time walk correction is to make this distribution as flat as possible in order to reduce the spread of the one-dimensional TOF distribution. To do so, the easiest way we will present here is to obtain the behavior of the TOF as a function of the inverse of the amplitude from the two-dimensional distribution. Once this dependance is known, one can simply fill a new two-dimensional histogram with the difference between all of the events in the initial two-dimensional histogram and the value of the function describing the dependance at this precise point. This will flatten the distribution meaning that after projecting on the y-axis to obtain the one dimensional TOF distribution, one should get rid of the larger spread. One could wonder how to determine the dependence on the two-dimensional distribution and this is what we will discuss now.

The first method which was investigated was by using the `TProfile` object from ROOT. What this object concretely does is turning a two dimensional histogram into a `TGraph` object which is simply a set of points in the (x-y) plane (for us (1/Amp1-TOF) plane) depending on an input value accounting for binning. More precisely, the `TProfile` defines its points by slicing the histogram along the x-axis into the number of bins specified, then taking the average of the position of all the points in the bin along the y-axis. The value for the point along the x-axis is defined as the middle of the bin and the y-value is defined as the average computed.

Unfortunately, it has been observed that this method was not optimal since it was visible by eye that the points defined using the `TProfile` were not a good representation of the distribution and were often giving points not centered at the middle of the distribution as it is expected from its shape. We then had to find a different method for the correction.

The second method which was investigated was more complex and needs a more detailed description. The main idea is that, if one takes a slice of the two-dimensional distribution corresponding to a certain range on the x-axis, the shape of the projected one-dimensional histogram for the TOF should be Gaussian since the full TOF distribution is in principle Gaussian. This means that in order to find the center of the distribution, one can simply perform a Gaussian fit on the projected TOF distribution. The value along the x-axis will then be the center of the slice and the value along the y-axis will be the position of the peak of the Gaussian fit performed i.e. the mean of the Gaussian function. This explains how this method works on the paper but it is interesting to understand how its performed from a code point of view.

A dedicated function was created, taking as an input the two-dimensional distribution, a rebinning coefficient along the x-axis (`rebin`), the minimum number of events in each slice (`stat`) and the range for the gaussian fits on the projected TOF one-dimensional distribution (`ylo` and `yhigh`). The output given is a set of four vectors containing respectively the values along the x-axis, the values along the y-axis, and the errors on each of them. We will now see the step by step description of what this function does:

- i) The function starts by creating a clone of the two-dimensional distribution and rebins it along x-axis according to the value of the `rebin` parameter. The initial two-dimensional distributions has a high number of bins in order to be able to further adjust depending on the shape of the distribution through that parameter.

- ii) A loop over all the bins along the x-axis for which the number of entries is greater or equal to one is performed. Another loop is performed in order to know the bounds in terms of bins numbers along the x-axis such that when the projection to obtain the TOF one-dimensional distribution is performed, the number of events will be greater than the value of the parameter `stat`.

A break condition was also added in order for the procedure to stop if the number of bins needed to obtain the required number of events is too large, this is to avoid continuously adding events in the tails of the distributions.

- iii) Still inside the second loop, for each iteration, the one-dimensional histogram for the projection is reseted (since it is used each time a projection is made). It is then filled with the projection on the y-axis of the values for the TOF of the events present in the bounds in terms on bins for this iteration in the loop. A check is performed with respect to the number of events contained, if the number of entries for the histogram is zero, the value of a counting parameter is raised by one and the iteration in the loop ends.

- iv) If the second loop manages to fill a one-dimensional histogram without reaching the threshold set on the number of maximum iterations, an additional check is performed. If the iteration in the first loop concerns the tail of the distribution for the highest values of the inverse of the amplitude then if the value of the counting parameter is greater than a certain value, it breaks the first loop.
- v) Once a viable one-dimensional TOF distribution is created, the binning is again changed according to a constant factor for the same reasons as the one for which the rebin was performed along the x-axis. Another projection is performed, on the same range along the x-axis but this time in a reduced range along the y-axis such that the distribution ranges from the difference of the mean of the first projection and four times its RMS (Root Mean Square) and the sum of the mean of the first projection and four times its RMS. This technique is used to not take into account the elements in the tail of the one-dimensional distributions for the TOF. When approaching the tails along the x-axis in the two-dimensional distribution the density of events decreases and so the points being very off in terms of TOF can affect much more the core of the distributions, this is not wanted. This way we probably miscorrect for a few points instead of miscorrecting many points in the core.
- vi) After performing the Gaussian fit on the TOF one-dimensional distribution, the last step is another rebinning according to the size of the slice. In fact it has been observed that the bigger the slice and the more spread the distributions was, it is then less easier to properly obtain a gaussian-shaped distribution suited to fit.
- vii) The final step is to perform the Gaussian fit on the obtained distribution, setting the input parameter for the mean of the Gaussian distribution as the value of the center of the bin having the most entries in the one-dimensional TOF distribution. The values saved are the center of the bin for the value along the x-axis, the value of the mean of the Gaussian distribution for the value along the y-axis. For the errors, the one on the value along the x-axis is the size of the range along which the projection is made, divided by the square root of twelve and the error on the value along the y-axis is the error from the Gaussian fit on the mean.

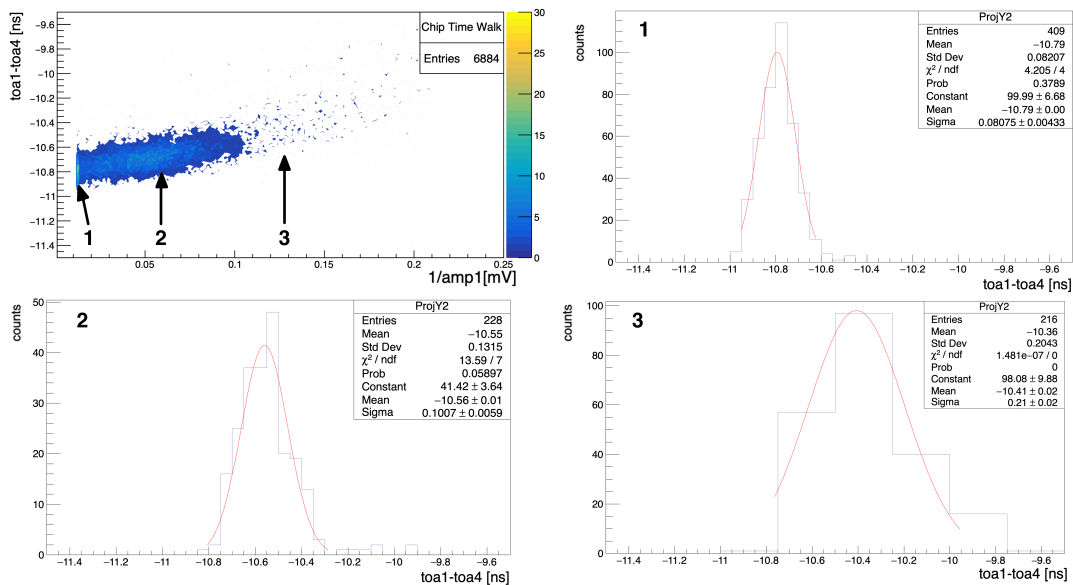


Figure 6.6: Different projections and their Gaussian fit

We can illustrate the above procedure by showing for three different points inside the distributions, what is the shape of the projected distribution but also the Gaussian fit performed. The main difference here with the TProfile method is that it is more sensible to the density of events in the distribution and can perform a more accurate correction. If we look at the two-dimensional distribution, we see that in the region for the highest amplitudes, the density of points is much greater than anywhere else. The TProfile method would have had points equally separated along the x-axis where the slicing method can define a point each time the slices contain at least a number of events equal to the value of the stat parameter. This means that for the densest regions of the distribution, there will be more points defined for the correction than with the TProfile method, giving a better representation of the dataset for further correction.

Now having the points on which the correction can be performed, one has to decide how he wants to extrapolates the dependance of the TOF as a function of the inverse of the amplitude. Two different methods were also investigated here and we will present them in what follows:

- i) The first method which is the one that comes to mind at first is to simply perform a fit on the points defined by the previously described method. In order to do that, a "progressive" polynomial function was implemented. What this function was doing is to fit the set of points with polynomial functions ranging from the zeroth degree to the ninth degree, one after the other, using as input parameter for the fit of degree n the values found for the degree $n - 1$. The fit having the best value for the ratio of the Chi squared over the number of degrees of freedom is then saved and used for the correction.

The counter part of this method is that it has been observed that due to the varying density of points, the fit can be more influenced by the densest region than the least dense ones resulting in an incorrect correction for these regions.

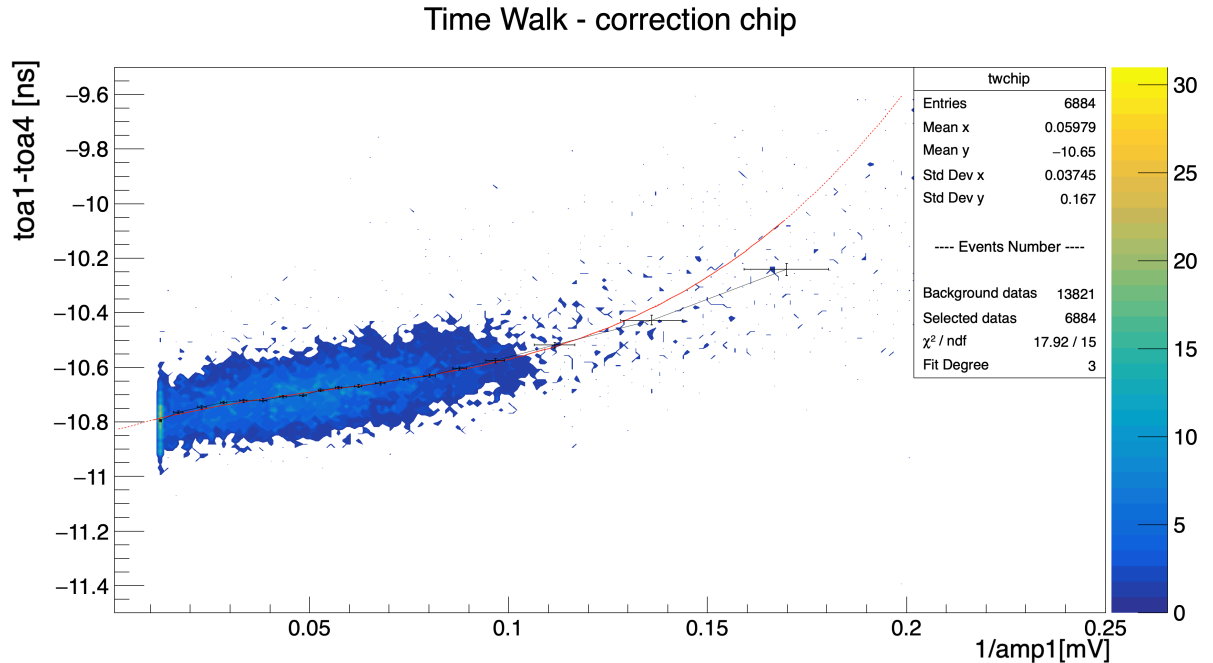


Figure 6.7: Correction using the fitting method

- ii) The second method investigated was to preform a linear interpolation between all of the points defined in the previous procedure. This way the correction is more correct no matter the density of points and it was observed that it produced better results with more accuracy.

The only counter part of this method is that if at some point the points are too separated, the correction will no longer be sensible to the small fluctuations. The performed correction will then be less accurate for these regions.

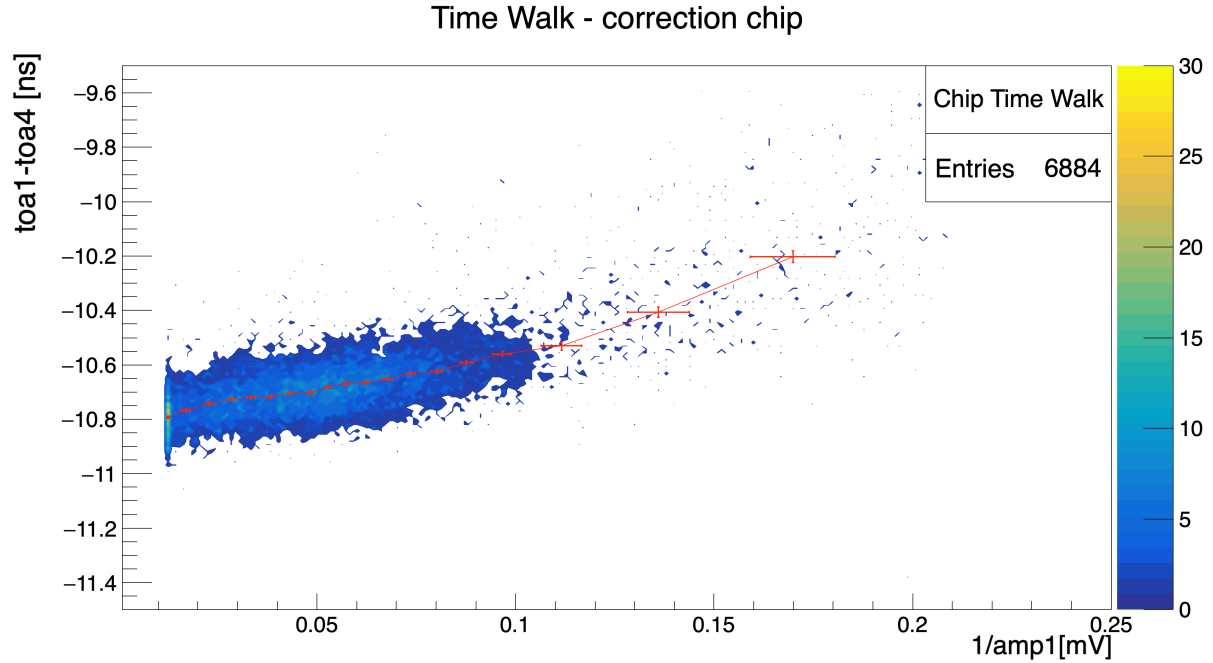


Figure 6.8: Correction using the interpolation method

The description of the method to obtain the correction to apply for time walk for all of the two-dimensional distributions is now finished. To perform the full correction for time walk, for all of the three methods of correction for the time walk for the ATTRACT pixel, there is also the need to perform the correction for the LGAD pixel.

6.2.3 TOF fitting method

The final step before getting the value of the time resolution is to perform the Gaussian fit of the one-dimensional TOF distribution after the two corrections are performed. The only difficult part with this final fit is that one has to take into account the fact that the distributions of the TOF is not perfectly symmetric and has a tail on one side. The TOF distributions should although have a gaussian shape which means one still needs to perform a Gaussian fit. The only risk with the tail is that it will influence the fit and produce a larger spread of the gaussian distributions than what it actually is.

To solve this issue, a fit was performed at many different percentages of the maximum of the distribution with the aim of finding for what percentage, the fit gives the best results in terms of how Gaussian the distribution is but also how good the Chi squared over the number of degrees of freedom ratio is. The percentage for which the results were the best was for 25 % of the maximum of the distributions. Hence when performing the fit with the Gaussian distribution, the range on the x-axis on which the fit was performed was on the left, the bin after which the number of entries was more than 25% the maximum number of entries in a bin and on the right the last bin for which the number of entries was more than 25% the maximum number of entries in a bin.

We present in the following picture an example of one of the Gaussian fit performed on one

of the TOF distributions obtained. One can see it exhibits on the right side the tail we were discussing above. The information on how much the distributions is Gaussian is simply given by the difference between the integral of the TOF distributions and the histogram generated from the Gaussian fit (with the same number of bins). It is represented as the percentage of the distributions which is "Gaussian" and the percentage which is not. Another interesting parameter computed here is the Full Width at Half Maximum (FWHM) of the TOF distribution divided by 2.355 which gives is supposed to be equal to the standard deviation of the Gaussian distributions obtained after fitting. The two variables are equal if and only if the TOF distribution is Gaussian. This parameter tells us also how good the fit performed is.

In the end, the parameter which interest us here is the standard deviation of the Gaussian distribution obtained after fitting. This value will help us determine the time resolution of the ATTRACT pixel itself as we will see in the next subsection.

6.2.4 Time resolution results

One has to pay attention to the fact that the result we obtained for the standard deviation of the TOF distribution is the quadratic composition of the time resolution for the ATTRACT pixel and the time resolution for the LGAD pixel such that we can write:

$$\sigma_{TOF}^2 = \sigma_{t,ATTRACT}^2 + \sigma_{t,LGAD}^2 \quad \Rightarrow \quad \sigma_{t,ATTRACT} = \sqrt{\sigma_{TOF}^2 - \sigma_{t,LGAD}^2} \quad (6.3)$$

The equation 6.3 then gives the time resolution of the ATTRACT pixel as a function of the time resolution associated to the measure we performed and the time resolution of the LGAD pixel. The error on the time resolution is then given by:

$$\Delta\sigma_{t,ATTRACT} = \sqrt{\left(\frac{\sigma_{TOF}}{\sqrt{\sigma_{TOF}^2 - \sigma_{t,LGAD}^2}}\right)^2 \cdot \Delta\sigma_{TOF}^2 + \left(\frac{\sigma_{t,LGAD}}{\sqrt{\sigma_{TOF}^2 - \sigma_{t,LGAD}^2}}\right)^2 \cdot \Delta\sigma_{t,LGAD}^2} \quad (6.4)$$

The only remaining unknown in the two equations 6.4 are the time resolution for the LGAD pixel as well as the error on the time resolution. According to the people who provided us with the LGAD sensor used for the measurement, the time resolution was:

$$\sigma_{t,LGAD} = (45 \pm 5) \text{ ps} \quad (6.5)$$

It is now possible to determine what is the value of the time resolution obtained for each of the different WP, for the different HVs as well as for the three different correction methods investigated.

We can see in the 6.9 figure the time resolution obtained for our sensor, for each of the WP and as a function of the HV applied. The very first thing one can notice is the decreasing value for the time resolution as the HV increase, and this for all of the four WPs. This behavior due to the fact that the higher the HV and the thicker the depletion region is. The main contribution to this behavior comes from signal to noise ratio becoming smaller as the depletion region becomes thicker and so the amount of released charges will increase. Another contribution is from the drift velocity of the charges increasing with increasing depth of the depletion region hence giving a smaller rise time. It can easily be seen by recalling that the time resolution can be written as:

$$\sigma_t = \frac{\text{Rise Time}}{\text{Signal to Noise ratio}} \quad (6.6)$$

This highlights the fact that the parameters of the pixels itself in contrast with the parameters of the electronics, can have an impact on the time resolution.

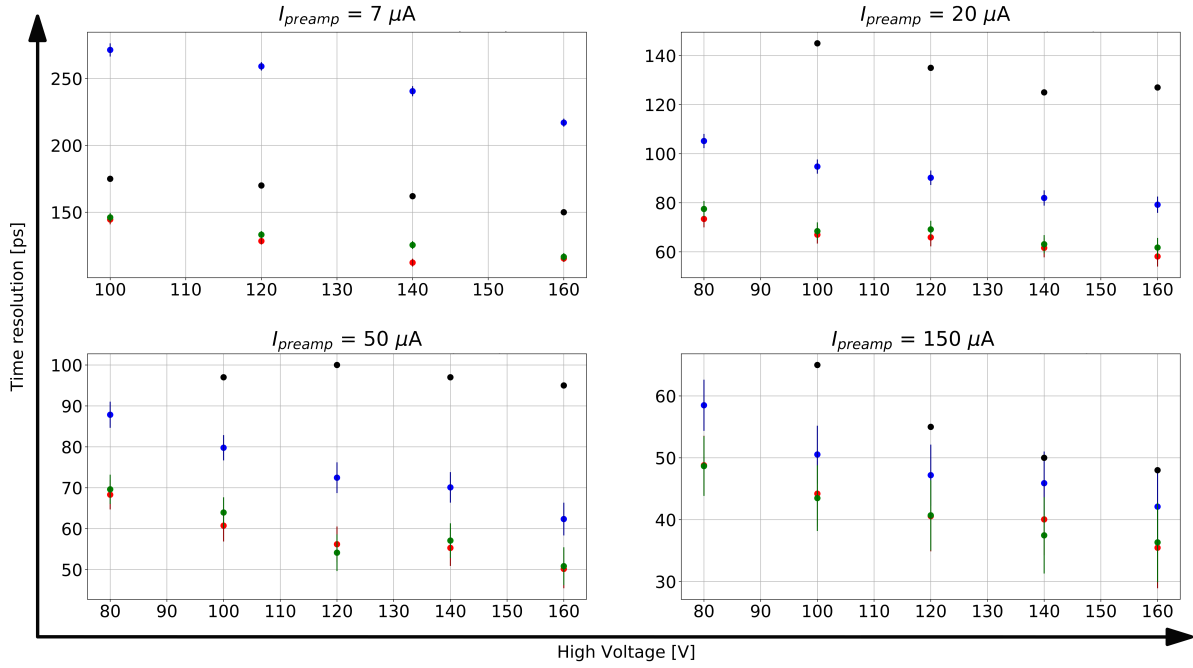


Figure 6.9: Comparaision of different correction methods for all WP and HVs

A second interesting observation one can perform is the difference between the results obtained for the three different corrections methods. For all of the WPs, the correction for time walk with respect to the TOT always gives the worst results. On the other hand, the results obtained for the correction with respect to the inverse of the amplitude or the inverse of the slope give more ore less similar results for all the WPs. These two previous methods are in fact similar to each other since the value of the inverse of the slope depends on the value of the amplitude.

Another interesting way to represent the results obtained is to look for a fixes HV and a fixed correction method, for example HV = 160 V and the inverse of the amplitude correction method, how the time resolutions changes with the bias current provided to the pre-amp. The results are presented in the following figure:

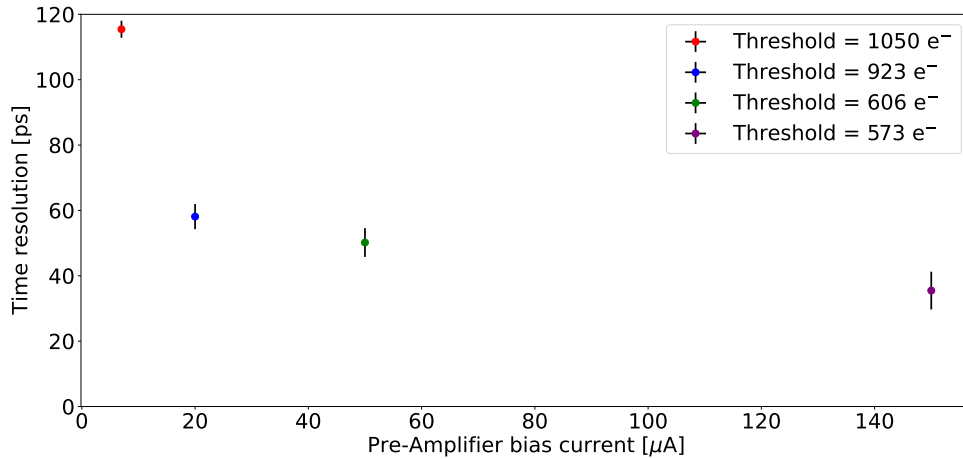


Figure 6.10: Time resolution as a function of the pre-amplifier current

One can here see that as the current for the pre-amp increases, the time resolution decreases which means better performances of the electronics as the current increases. This can be simply explained by recalling the fact that the pre-amp is a simple transistor and changing the current provided to it changes the frequency at which this previous is working. The result is then faster electronics and hence better performances.

The presentation of the results settles the end of the characterisation of the ATTRACT sensor in terms of time resolutions and shows the effect of the time walk correction on the time resolution which is set, up to the best performances to a value slightly above the 35 ps. One could still argue here that the time resolution of the reference object is bigger than the one of the object we put to the test. It was then considered to also perform this measure with an LGAD having a much lower time resolution, of the order of 30 ps, or even to measure the time resolution between two Attract sensors which would give the most accurate measurement of the time resolution at the cost of a much lower rate of events and hence much longer data takings.

Chapter 7

Outlook and conclusion

All along the discussion about the work performed during this thesis, we went through the motivation of the QCD Axion solution to the strong CP problem, going through inductions on the classical level but also on the quantum level and showed why it is the most promising solution. We also have seen that the mathematical material behind this solution can also be generalized to a more wide category of model predicting particles Beyond the SM of particle physics and the model of interest here was the ALP. We studied a particular model of ALP in which it can couple to the electroweak and we investigated the possible generation of ALP benefiting from this coupling through FCNC, further decaying into the main decay channel in the 100 MeV to a few GeV mass range for the ALP, the di-photon channel.

We then presented the FASER detector located at CERN, described its design and showed that it could not, in its current status, detect the di-photon decay from the ALPs. For this reason, we described the Pre-Shower module suggested by the University of Geneva as an upgrade of the current FASER detector design and quickly presented how it would be structured.

The suspended question was the number of ALPs decay FASER could probe with the suggested Pre-Shower detector proposed. For this purpose, we went through Monte Carlo simulations of the ALPs generated from the ATLAS IP through the FCNC decays of heavy mesons like Kaons and B-mesons in particular. We then proceeded towards the decay of the ALPs into two photons and have selected only the ones decaying inside FASER's decay volume and reaching the Pre-Shower module. Throughout the simulations, the information relative to the kinematics of the photons coming from the ALPs decays as well as the ALP itself we saved and the number of events for a specific ALP model with certain mass and coupling, was computed. The results showed that due to the highly energetic mesons from which the ALPs originate, the two photons can be highly collimated and hence requiring a small separation between the two to be able to identify them. We also observed that if the energy of the two photons is asymmetric, this produces a greater separation between the two photons which makes them more easily observable. We also realized that the asymmetry in the energy and the separation between the two photons was dependent of the mass and the coupling. To end the discussion on the Monte Carlo simulations and the Pre-Shower module, we produced thanks to the GEANT4 simulations performed for the Pre-Shower to obtain its efficiency as a function of the energy of the photons and their spatial separation, the reach plot of the FASER detector with the Pre-Shower, for detecting ALP decays. We showed the results for different integrated luminosities for the data taking and also showed how the covered area in the (mass-coupling) parameter space, changes depending of the integrated luminosity as well as the required separation between the photons.

The discussion moved towards the description of the SiGe BiCMOS technology in order to

produce silicon pixel detectors for timing purposes. The fundamentals of the theory of silicon sensors were presented as well as the noise sources these sensors are suffering from. We then detailed the procedure used to characterize the time resolution of one of the prototypes designed for the ATTRACT project, by performing a Time Of Flight measurement between the tested sensor and a reference sensor. We explained how both sensors worked and explained the data taking scheme used.

The final discussion was oriented towards the correction for one of the noise contributions to the time resolution for silicon pixel detectors, the time walk. We showed in detail how to perform a time walk correction for the ATTRACT sensor and compared three different methods of correction to find out which one was the most suited. The result proved that the best method to correct for time walk was to perform a correction with respect to the amplitude of the signal or with respect to the slope of the signal, i.e. how fast it would rise. The results for different working conditions of the electronics as well as the sensor itself were given, exhibiting an improvement of the time resolution with higher High Voltage for the sensor, as well as better time resolution for higher bias current provided to the pre amplifier. The optimal performance in terms of timing was obtained using the amplitude correction method and showed a time resolution of the order of 35 ps for the highest bias current for the pre-amplifier.

The Monte Carlo simulations performed are here giving the results in terms of reach for the FASER detector only for one specific models but in fact one could also add the other productions mechanisms as well as other decay of the ALPs into SM particles resulting in a more accurate reach. The result also only showed the results for the current design of the FASER detector and it could also have been great to perform the same analysis for future improvement of FASER.

Regarding the time resolution obtained for the ATTRACT sensor, the time walk correction method developed good results but the possible improvements relies on the data taking procedure used. It turned out the measurement of the time resolution gave a result which was above the time resolution of the reference object. Some further measurement are ongoing with a faster reference object with a time resolution of the order of 30 ps but some issues have been encountered with respect to the board on which these previous were glued. The optimal solution would be to use two Attract sensors and to perform the time measurements between themselves but it requires an improved design of the board to bring the sensors as close as possible to enhance the event rate.

Bibliography

- [1] T. D. Lee and C. N. Yang. “Question of Parity Conservation in Weak Interactions”. In: *Physical Review* 104.1 (Oct. 1, 1956), pp. 254–258. ISSN: 0031-899X. DOI: 10.1103/PhysRev.104.254. URL: <https://link.aps.org/doi/10.1103/PhysRev.104.254> (visited on 06/20/2021).
- [2] Bogdan Povh et al. *Particles and Nuclei: An Introduction to the Physical Concepts*. 7th ed. 2015. Graduate Texts in Physics. Berlin, Heidelberg: Springer Berlin Heidelberg : Imprint: Springer, 2015. 1 p. ISBN: 978-3-662-46321-5. DOI: 10.1007/978-3-662-46321-5.
- [3] Anson Hook. “TASI Lectures on the Strong CP Problem and Axions”. In: *arXiv:1812.02669 [hep-ph]* (Dec. 6, 2018). arXiv: 1812.02669. URL: <http://arxiv.org/abs/1812.02669> (visited on 05/23/2021).
- [4] J. H. Smith, E. M. Purcell, and N. F. Ramsey. “Experimental Limit to the Electric Dipole Moment of the Neutron”. In: *Physical Review* 108.1 (Oct. 1, 1957), pp. 120–122. ISSN: 0031-899X. DOI: 10.1103/PhysRev.108.120. URL: <https://link.aps.org/doi/10.1103/PhysRev.108.120> (visited on 05/23/2021).
- [5] C. Abel et al. “Measurement of the Permanent Electric Dipole Moment of the Neutron”. In: *Physical Review Letters* 124.8 (Feb. 28, 2020), p. 081803. ISSN: 0031-9007, 1079-7114. DOI: 10.1103/PhysRevLett.124.081803. URL: <https://link.aps.org/doi/10.1103/PhysRevLett.124.081803> (visited on 05/23/2021).
- [6] M. Tanabashi et al. “Review of Particle Physics”. In: *Physical Review D* 98.3 (Aug. 17, 2018), p. 030001. ISSN: 2470-0010, 2470-0029. DOI: 10.1103/PhysRevD.98.030001. URL: <https://link.aps.org/doi/10.1103/PhysRevD.98.030001> (visited on 06/19/2021).
- [7] E. Wigner. “On the Consequences of the Symmetry of the Nuclear Hamiltonian on the Spectroscopy of Nuclei”. In: *Physical Review* 51.2 (Jan. 15, 1937), pp. 106–119. ISSN: 0031-899X. DOI: 10.1103/PhysRev.51.106. URL: <https://link.aps.org/doi/10.1103/PhysRev.51.106> (visited on 05/23/2021).
- [8] Kazuhiko Nishijima. “Charge Independence Theory of V Particles”. In: *Progress of Theoretical Physics* 13.3 (Mar. 1955), pp. 285–304. ISSN: 0033-068X. DOI: 10.1143/PTP.13.285. URL: <https://academic.oup.com/ptp/article-lookup/doi/10.1143/PTP.13.285> (visited on 06/20/2021).
- [9] Michael Edward Peskin and Daniel V. Schroeder. *An introduction to quantum field theory*. Reading, Mass: Addison-Wesley Pub. Co, 1995. 842 pp. ISBN: 978-0-201-50397-5.
- [10] Jeffrey D. Kost. *Phase Transitions in the Early Universe: The Cosmology of Non-minimal Scalar Sectors*.
- [11] Matthew Dean Schwartz. *Quantum field theory and the standard model*. New York: Cambridge University Press, 2014. 850 pp. ISBN: 978-1-107-03473-0.

-
- [12] R. D. Peccei. “QCD, Strong CP and Axions”. In: *arXiv:hep-ph/9606475* (June 28, 1996). arXiv: hep-ph/9606475. URL: <http://arxiv.org/abs/hep-ph/9606475> (visited on 05/23/2021).
- [13] C. Aubin et al. “Light pseudoscalar decay constants, quark masses, and low energy constants from three-flavor lattice QCD”. In: *Physical Review D* 70.11 (Dec. 8, 2004), p. 114501. ISSN: 1550-7998, 1550-2368. DOI: 10.1103/PhysRevD.70.114501. URL: <https://link.aps.org/doi/10.1103/PhysRevD.70.114501> (visited on 06/20/2021).
- [14] Ann Nelson. “Calculation of $\bar{b} \rightarrow s$ ”. In: *Physics Letters B* 143.1 (Aug. 1984), pp. 165–170. ISSN: 03702693. DOI: 10.1016/0370-2693(84)90827-X. URL: <https://linkinghub.elsevier.com/retrieve/pii/037026938490827X> (visited on 06/20/2021).
- [15] R. D. Peccei and Helen R. Quinn. “CP Conservation in the Presence of Pseudoparticles”. In: *Physical Review Letters* 38.25 (June 20, 1977), pp. 1440–1443. ISSN: 0031-9007. DOI: 10.1103/PhysRevLett.38.1440. URL: <https://link.aps.org/doi/10.1103/PhysRevLett.38.1440> (visited on 06/20/2021).
- [16] Eder Izaguirre, Tongyan Lin, and Brian Shuve. “Searching for Axionlike Particles in Flavor-Changing Neutral Current Processes”. In: *Physical Review Letters* 118.11 (Mar. 15, 2017), p. 111802. ISSN: 0031-9007, 1079-7114. DOI: 10.1103/PhysRevLett.118.111802. URL: <https://link.aps.org/doi/10.1103/PhysRevLett.118.111802> (visited on 05/23/2021).
- [17] Jonathan L. Feng et al. “ALPs at FASER: The LHC as a Photon Beam Dump”. In: *Physical Review D* 98.5 (Sept. 18, 2018), p. 055021. ISSN: 2470-0010, 2470-0029. DOI: 10.1103/PhysRevD.98.055021. arXiv: 1806.02348. URL: <http://arxiv.org/abs/1806.02348> (visited on 05/23/2021).
- [18] Akitaka Ariga et al. “FASERs physics reach for long-lived particles”. In: *Physical Review D* 99.9 (May 15, 2019), p. 095011. ISSN: 2470-0010, 2470-0029. DOI: 10.1103/PhysRevD.99.095011. URL: <https://link.aps.org/doi/10.1103/PhysRevD.99.095011> (visited on 05/23/2021).
- [19] M. Aaboud et al. “Measurement of the Inelastic Proton-Proton Cross Section at $s = 13$ TeV with the ATLAS Detector at the LHC”. In: *Physical Review Letters* 117.18 (Oct. 26, 2016), p. 182002. ISSN: 0031-9007, 1079-7114. DOI: 10.1103/PhysRevLett.117.182002. URL: <https://link.aps.org/doi/10.1103/PhysRevLett.117.182002> (visited on 06/20/2021).
- [20] FASER Collaboration et al. “Technical Proposal for FASER: ForWArD Search Experiment at the LHC”. In: *arXiv:1812.09139 [hep-ex, physics:hep-ph, physics:physics]* (Dec. 21, 2018). arXiv: 1812.09139. URL: <http://arxiv.org/abs/1812.09139> (visited on 05/23/2021).
- [21] Babette Döbrich et al. “ALPtraum: ALP production in proton beam dump experiments”. In: *Journal of High Energy Physics* 2016.2 (Feb. 2016), p. 18. ISSN: 1029-8479. DOI: 10.1007/JHEP02(2016)018. URL: [http://link.springer.com/10.1007/JHEP02\(2016\)018](http://link.springer.com/10.1007/JHEP02(2016)018) (visited on 05/23/2021).
- [22] S. L. Glashow, J. Iliopoulos, and L. Maiani. “Weak Interactions with Lepton-Hadron Symmetry”. In: *Physical Review D* 2.7 (Oct. 1, 1970), pp. 1285–1292. ISSN: 0556-2821. DOI: 10.1103/PhysRevD.2.1285. URL: <https://link.aps.org/doi/10.1103/PhysRevD.2.1285> (visited on 06/20/2021).
- [23] Stefania Gori, Gilad Perez, and Kohsaku Tobioka. “KOTO vs. NA62 Dark Scalar Searches”. In: *arXiv:2005.05170 [hep-ex, physics:hep-ph]* (May 11, 2020). arXiv: 2005.05170. URL: <http://arxiv.org/abs/2005.05170> (visited on 05/23/2021).
-

- [24] T. Pierog et al. “EPOS LHC: Test of collective hadronization with data measured at the CERN Large Hadron Collider”. In: *Physical Review C* 92.3 (Sept. 14, 2015), p. 034906. ISSN: 0556-2813, 1089-490X. DOI: 10.1103/PhysRevC.92.034906. URL: <https://link.aps.org/doi/10.1103/PhysRevC.92.034906> (visited on 06/20/2021).
- [25] Torbjörn Sjöstrand, Stephen Mrenna, and Peter Skands. “PYTHIA 6.4 physics and manual”. In: *Journal of High Energy Physics* 2006.5 (May 9, 2006), pp. 026–026. ISSN: 1029-8479. DOI: 10.1088/1126-6708/2006/05/026. URL: <http://stacks.iop.org/1126-6708/2006/i=05/a=026?key=crossref.7fbc8fa1a47a48f7565bead655446685> (visited on 06/20/2021).
- [26] Leonardo Rossi et al. *Pixel Detectors: From Fundamentals to Applications*. Red. by Alexander Chao et al. Particle Acceleration and Detection. Berlin, Heidelberg: Springer Berlin Heidelberg, 2006. ISBN: 978-3-540-28332-4 978-3-540-28333-1. DOI: 10.1007/3-540-28333-1. URL: <http://link.springer.com/10.1007/3-540-28333-1> (visited on 06/20/2021).
- [27] L. Paolozzi et al. “Test beam measurement of the first prototype of the fast silicon pixel monolithic detector for the TT-PET project”. In: *Journal of Instrumentation* 13.4 (Apr. 12, 2018), P04015–P04015. ISSN: 1748-0221. DOI: 10.1088/1748-0221/13/04/P04015. URL: <https://iopscience.iop.org/article/10.1088/1748-0221/13/04/P04015> (visited on 06/20/2021).
- [28] G. Iacobucci et al. “A 50 ps resolution monolithic active pixel sensor without internal gain in SiGe BiCMOS technology”. In: *Journal of Instrumentation* 14.11 (Nov. 6, 2019), P11008–P11008. ISSN: 1748-0221. DOI: 10.1088/1748-0221/14/11/P11008. URL: <https://iopscience.iop.org/article/10.1088/1748-0221/14/11/P11008> (visited on 06/20/2021).
- [29] N. Moffat et al. “Low Gain Avalanche Detectors (LGAD) for particle physics and synchrotron applications”. In: *Journal of Instrumentation* 13.3 (Mar. 9, 2018), pp. C03014–C03014. ISSN: 1748-0221. DOI: 10.1088/1748-0221/13/03/C03014. URL: <https://iopscience.iop.org/article/10.1088/1748-0221/13/03/C03014> (visited on 06/20/2021).
- [30] V. Sola et al. “First FBK Production of 50\$\\mu\$m Ultra-Fast Silicon Detectors”. In: *Nuclear Instruments and Methods in Physics Research Section A: Accelerators, Spectrometers, Detectors and Associated Equipment* 924 (Apr. 2019), pp. 360–368. ISSN: 01689002. DOI: 10.1016/j.nima.2018.07.060. arXiv: 1802.03988. URL: <http://arxiv.org/abs/1802.03988> (visited on 06/20/2021).
- [31] Rene Brun and Fons Rademakers. “ROOT An object oriented data analysis framework”. In: *Nuclear Instruments and Methods in Physics Research Section A: Accelerators, Spectrometers, Detectors and Associated Equipment* 389.1 (Apr. 1997), pp. 81–86. ISSN: 01689002. DOI: 10.1016/S0168-9002(97)00048-X. URL: <https://linkinghub.elsevier.com/retrieve/pii/S016890029700048X> (visited on 06/20/2021).